High Surface Area Cu/γ-Al₂O₃ Catalyst Synthesized by Reverse Microemulsion Method for CO₂ Conversion via Reverse Water Gas Shift

by

Zakharova Anastasiia

A thesis

presented to the University of Waterloo

in fulfillment of the

thesis requirement for the degree of

Master of Applied Science

in

Chemical Engineering

Waterloo, Ontario, Canada, 2021

Author's declaration

I hereby declare that I am the sole author of this thesis. This is a true copy of the thesis, including any required final revisions, as accepted by my examiners.

I understand that my thesis may be made electronically available to the public.

Abstract

Nowadays, catalytic conversion of CO_2 has gained a great attention due to environmental issues caused by CO_2 emission around the world. CO_2 can be considered as a source of carbon with hydrogenation (using renewable hydrogen) as a possible approach for transforming CO_2 into value-added chemicals and fuels creating an artificial carbon cycle. This study investigated the catalytic performance of γ-alumina-supported copper oxide for the reverse water gas shift reaction. The catalytic nanoparticles were characterized by various analytical techniques such as XRD, SEM, TPR etc. Reverse microemulsion (RME) technique was deployed for the synthesis of highly porous CuO supported on $γ-Al_2O_3$ with a specific surface area of 369.69 m^2/g.

The catalytic performance of the synthesized catalyst was evaluated under various operating conditions (300-500 °C and 10,000 to 200,000 mL $g_{cat}^{-1} h^{-1}$). Results showed 100% CO selectivity with excellent CO_2 conversion (near to equilibrium, 53%) at 500 °C. Catalyst stability test was conducted for 95 h at 1 atm and 600 °C with varying space velocities. RME-prepared $Cu/γ-Al_2O_3$ catalyst showed excellent catalytic stability and CO_2 conversion of 61% at GHSV of 60,000 and 41% at GHSV of 200,000 mL $g_{cat}^{-1} h^{-1}$. This study showed that reverse microemulsion is a promising method for developing catalysts and enhancing their functionality in thermo-catalytic reactions.

CO_2 adsorption mechanism was studied via in-situ FTIR. At 300 °C and low gas concentration, CO_2 was physically adsorbed on the surface as carbonates and the persistent formation of CO was observed. A rate equation was suggested along and kinetic parameters were estimated in order to extrapolate the experimentally measured data. The resulting reaction rate expression with the estimated parameters was successfully implemented under various operating conditions to evaluate the catalytic performance.

Keywords: CO_2 conversion, reverse water gas shift, copper catalyst, reverse microemulsion

Acknowledgment

I would like to thank my supervisor Professor David Simakov for the continuous support, patience and guidance throughout my master's program.

I would also like to thank my committee members: Aiping Yu and Hector Budman for their valuable comments and suggestions on my research project.

This work would not have been possible without the help and advice from my group members: Yichen Zhuang, Guanjie Sun, Yue Yu and Muhammad Waqas.

Finally, I would like to thank my family who encourage and support me during this program.

Table of contents

List of figures

viii

List of tables

Nomenclature

λ	wavelength of the X-ray
d	plane spacing
θ	the grazing angle
p	the pressure at equilibrium
p_2	the saturated vapor pressure of the adsorbed gas
Vm	the volume of gas required to form a monolayer on the surface
V	the amount of adsorption
N_A	Avogadro constant
s	adsorption cross-sectional area of the adsorbed species
V	molar volume of the adsorbed species
a	quality of the adsorbent material
di	diameter
D	dispersion
f_1	CO_2 conversion to CO
f_2	CO_2 conversion to CH_4
$F_{C,out}$	total outlet molar flow rate of carbon-containing species
$F_{H_2,f}$	feed molar flow rate of H_2
$F_{CO_2,f}$	feed molar flow rate of CO_2
$F_{CO,out}$	outlet molar flow rate of CO
$F_{CH_4,out}$	outlet molar flow rate of CH_4
$F_{t,out}$	total outlet molar flow rate
Q_f	volumetric feed flow rate
L_{Cu}	copper loading
M_{Cu}	copper molar weight
r_{CO}	CO generation rate per catalytic weight
R_{CO}	CO generation rate per active phase weight
S_{CH_4}	selectivity to CH_4
U	uptake
W_c	catalyst weight
X_{CO_2}	CO_2 conversion
y_i	mole fraction (i stands for either CO_2, CO, or CH_4)
ΔH°_{298}	reaction enthalpy
α	H_2:CO_2 ratio in the feed
ρ_{site}	Cu site density
ρ_{Cu}	copper density

Abbreviations

ADC	Analog-to-digital converter
BET	Brunauer–Emmett–Teller
BPR	Back pressure regulator
CB	Carbon balance
CCS	Carbon capture and storage
CCU	Carbon capture and utilization
CLC	Chemical looping combustion
FTIR	Fourier transform infrared spectroscopy
GHG	Greenhouse gas
GHSV	Gas hourly space velocity
ICP–OES	Inductively coupled plasma–optical emission spectrometry
IR	Infrared
MFC	Mass flow controller
PC	Personal computer
PI	Pressure indicator
RH	Relative humidity
RME	Reverse microemulsion
RWGS	Reverse water gas shift
S	Selectivity
SSA	Specific surface area
SEM–EDS	Scanning electron microscopy–energy dispersive spectroscopy
TC	Thermocouple
TCD	Thermal conductivity detector
TOF	Turnover frequency
TGA	Thermogravimetric analysis
TI	Temperature indicator
TPD	Temperature-programmed desorption
TPR	Temperature-programmed reduction
X	Conversion
XRD	X-ray diffraction

Chapter 1: Introduction

1.1 Problem statement

Over the last century, the concentration of greenhouses gases increased drastically due to human activities [1]. Many environmental problems are linked to the negative climate change impact such as ice retreat, heavy rainfall and flooding, ocean acidification, permafrost melt, loss of glaciers, increased intensity of hurricanes, etc. Reducing the atmospheric levels of CO_2 is among the most significant challenges. Emission-reducing strategies have become a worldwide consensus in mitigating the climate change [2]. For the CO_2 mitigation purposes carbon capture, storage, sequestration and utilization technologies must play an important role in the upcoming future [3]. The direct reduction of CO_2 is achieved by the contact with chemical media such as solvents or sorbents. Carbon capture and storage (CCS) is a process of capturing CO_2, usually produced from the large manufacturing industries such as fossil fuels plans then transporting it to the site where is it injected and stored in the underground geological formations. Carbon capture and utilization (CCU) is the other known process of capturing CO_2 and recycling it to various valuable products such as plastics, biofuels, etc. An alternative method for CO_2 capture is chemical looping combustion (CLC) that mainly consists of pre-, post- and oxy-combustion which are very energy intensive techniques, therefore expensive. At the same time, new emerging CLC approaches may reduce the energy consumption.

There are various problems with the abovementioned strategies. The direct capture is lacking the technological advancement in utilization of energy sources such as natural gas and renewable electricity. The CCS and CLC approaches require high capital and operational cost due

to high-energy demand. As for CCU, the long-term consequences of CO_2 storage are unknown and require the special attention.

CCU has several ways such as photo- and electro-chemical reduction, as well as biological and thermocatalytic reduction. Photo- and electro-chemical reduction along with biological one pose some limitation towards implementation such as low CO_2 solubility and high cost of biological cultivation systems [4, 5]. The thermocatalytic CO_2 conversion to synthetic fuels using renewable sources of energy is an alternative solution. Design and development of high-performance and cost-effective hydrogenation catalysts is among the most important challenges to be addressed in developing processes for the utilization of CO_2 via thermocatalytic conversion.

Reduction of CO_2 using renewable energy sources can produce syngas ($CO+H_2$) by using the reverse water-gas shift (RWGS) reaction. The syngas is considered as an important feedstock for the production of chemicals and fuels via Fischer-Tropsch synthesis [6, 7]. The endothermic RWGS reaction, Eq. 1, requires a catalyst that has to be operated at a relatively high temperature (600-750 °C) [8] to achieve significant conversion. The other thermocatalytic reactions, along with the RWGS reaction, can occur in the same temperature range, such as Sabatier reaction, Eq. 2, and CO methanation, Eq. 3 [9].

$$CO_2 + H_2 \rightleftarrows CO + H_2O \qquad \Delta H^{\circ}_{298} = +41.2 \text{ kJ/mol} \qquad (1)$$

$$CO_2 + 4H_2 \rightleftarrows CH_4 + 2H_2O \qquad \Delta H^{\circ}_{298} = -164.9 \text{ kJ/mol} \qquad (2)$$

$$CO + 3H_2 \rightleftarrows CH_4 + H_2O \qquad \Delta H^{\circ}_{298} = -206.5 \text{ kJ/mol} \qquad (3)$$
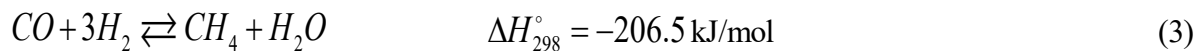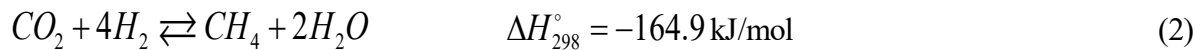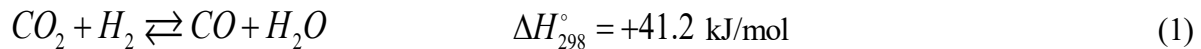
As a result, the thermocatalytic conversion was chosen for the reduction of CO_2 to CO using the synthesized catalyst. The goal of this study is to develop a highly active and resistant to

deactivation heterogeneous catalyst for the CO_2 to CO via RWGS at a temperature up to 600 ˚C. The present work is directed to the investigation of the properties and potential of RME synthesized copper-based catalysts for the RWGS reaction.

1.2 Project objectives

The project objective was to develop a highly active, selective and resistant heterogeneous copper-based catalysts for CO production via the reverse water gas shift (RWGS) reaction at the temperature up to 600 ˚C. To fulfill this goal, not only characterization of the catalyst is important, but also understanding the reaction mechanism and evaluating the catalytic performance. The following specific objectives are listed below:

1.   Synthesis of the high surface area copper-based catalyst by reverse-microemulsion (RME) method;

2.   Catalyst performance evaluation of the prepared catalyst based on CO_2 conversion and selectivity to CO in the range of temperatures and space velocities;

3.   Catalyst characterization using various analytical techniques (XRD, SEM-EDS, BET, TPR, TPD, ICP-OES) to examine the reaction mechanism;

4.   Study of the CO_2 adsorption mechanism on molecular level using in-situ FTIR;

5.   Conducting the kinetic parameter estimation based on obtained experimental data to gain the insights on the performance of the catalyst;

6.   Evaluation of the catalytic stability under various space velocities and the catalytic thermal deactivation study to evaluate the catalytic performance and resistance towards sintering, coking and deactivation.

1.3 Thesis outline

This thesis introduces the study on Cu-catalyst synthesised by reverse microemulsion methods for the reverse water gas shift reaction. Thesis chapters are outlined below:

Chapter 2 introduces background on CO_2 emission and global climate change. The thermocatalytic pathway is proposed as a way to solve the CO_2 emission problem. It summarizes the literature review of reverse water gas shift catalysts and reverse microemulsion method.

Chapter 3 and Chapter 4 describe the newly developed methodology for the catalyst synthesis and catalyst characterization methods. The experimental setup for catalytic performance evaluation and mechanistic studies is described as well.

Results and discussion are provided in Chapters 5 and 6, which are divided into the following parts: catalyst characterization, catalytic performance evaluation and catalyst stability evaluation. Briefly, catalyst properties such as surface area, morphology, chemical composition and reducibility were obtained from the characterization studies. The catalytic performance and catalyst stability results were conducted at various reaction condition. CO_2 conversion and selectivity to CO were obtained from the reaction tests performed in a lab-scale reactor. In-situ FTIR studies were conducted on the CO_2 adsorption on fresh and spent catalysts. Validation of the experimental data by the kinetic parameter estimation model was performed in MATLAB. Chapter 7 concludes the results obtained in Chapters 5 and 6 and discusses possible research directions in the future.

Chapter 2: Background and literature review

2.1 CO_2 emission and global climate change

Carbon dioxide emissions are the most harmful to the environment and consequently the major cause of global warming. The CO_2 emissions are mostly created by people during the process of agriculture and burning fossil fuels like, for example, oil, natural gas, petrol, and diesel. The level of CO_2 constantly increases around the world by almost 3% each year, this leads to inevitable consequences to the environment as the temperature is going to rise around 2 °C. These changes slowly alter the Earth resulting in ice sheets melting, sea level increasing, and extreme weather such as heavy rainfalls, storms and longer drought periods. Therefore, the goal of the world is to lower the emission using alternative sources of energy and the reduction of fossil fuel consumption. The greenhouse gas emissions profiles are quite similar in all industrialized countries. As for Canada, the main GHG contributor is CO_2. The total amount of emissions in 2018 was 728 Megatonnes of carbon dioxide equivalent (Mt CO_2 eq) in Fig. 1. During this period 1990 and 2019, emissions raised by about 21% mainly due to mining, upstream oil and gas, and transport [10].
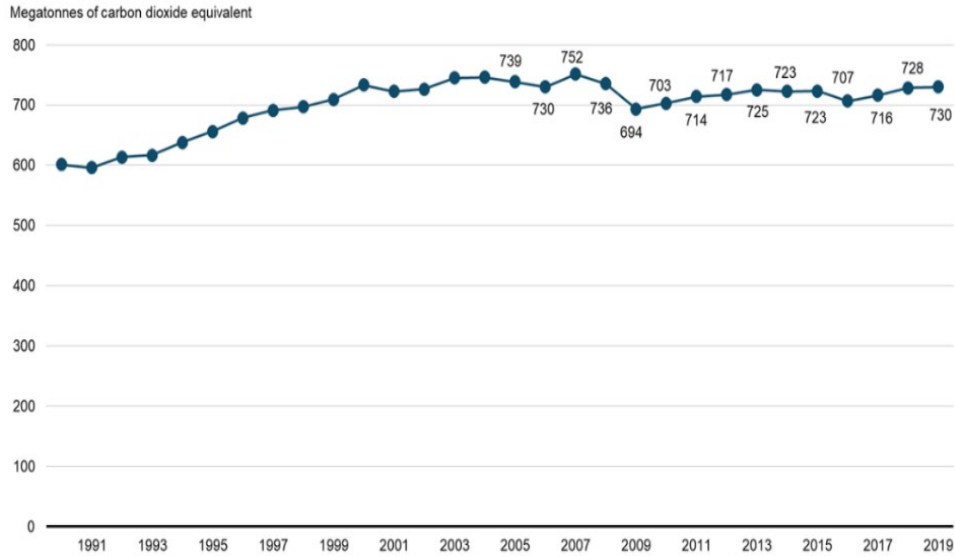
Fig. 1 Carbon dioxide emissions (Mt CO_2 eq), Canada, 1990 to 2019 [10].

In 2018, the main GHG emissions sectors were transportation, oil, and gas in Canada in Fig. 2. In total both sectors, account for 51% of total emissions [10]. As for the rest of sectors they take only 6-12% of total emissions.
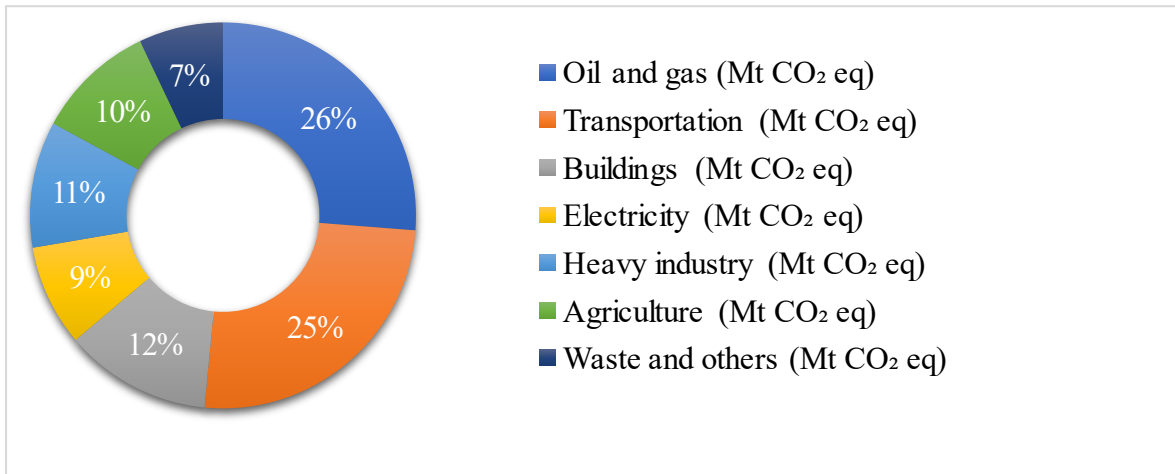
Fig. 2 Canada's Greenhouse gas emissions by economic sector in 2018 [10].

The Canadian energy industry generated 641 terawatt-hours (TWh) of electricity in 2018 in Fig. 3 [11]. The main energy source is hydro as it makes up 60% of total electricity production.

Then the nuclear energy sector is about 15%, while renewables produce only 7%. The rest is gas/oil around 11% and coal about 7% [11].
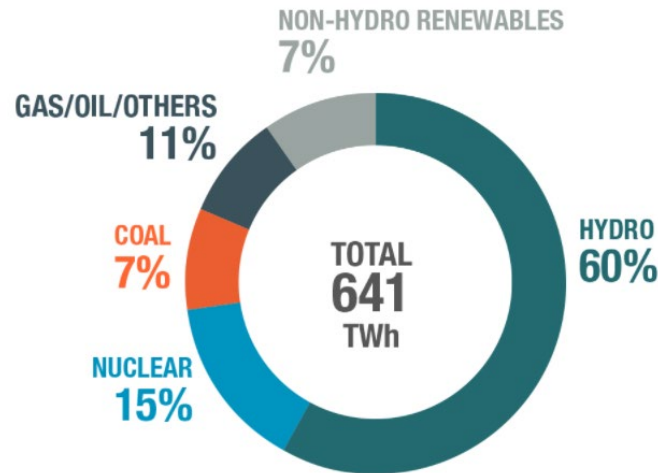
Fig. 3 Electricity generation by source in Canada, 2018 [11].

There is a need to deal with constantly growing CO_2 emissions and the best way to start is to lower fossil fuels such as oil, natural gas because the CO_2 concentration continues to agglomerate in the atmosphere. Some promising approaches to tackle CO_2 emissions will be presented in the next chapter.

2.2 Background on thermocatalytic CO_2 conversion

2.2.1 Reaction pathways

There are various approaches to deal with emissions in the atmosphere such as direct CO_2 emission reduction, CO_2 capture and storage (CCS), and CO_2 capture and utilization (CCU) into renewable synthetic chemicals and fuels [5]. An attractive and potentially profitable way is to convert CO_2 into useful chemicals and fuels, because these products can be sold to end consumers.

Also, the usage of fossil fuels will be significantly lowered as synthetic fuels can be used for various purposes such as heat and power generation and transportation.

Various thermocatalytic routes for the conversion of CO_2 into synthetic fuels and chemicals are shown in Fig. 4; red and blue arrows represent exothermic and endothermic reactions, respectively [5]. To conduct the thermocatalytic reaction it is necessary to obtain H_2 as a reactant. Water electrolysis, which can be powered by using renewable sources of energy (such as solar, wind, hydro), can be a solution for H_2 production.
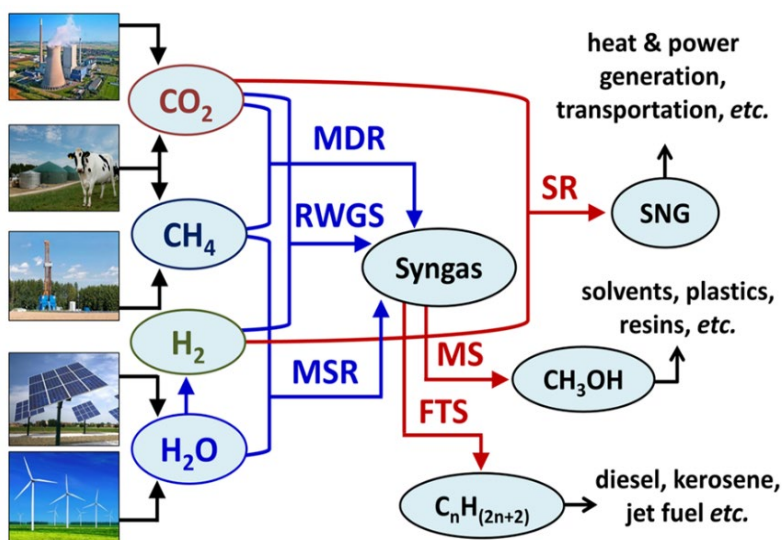
Fig. 4 CO_2 reaction pathways, syngas production and its derivatives [5].

A process of methane steam reforming (MSR), the reaction of methane and water, produces syngas ($CO+H_2$) as well as methane dry reforming (MDR), the reaction of methane and carbon dioxide. The other possible way to produce syngas is reverse water gas shift reaction (RWGS), the reaction of carbon dioxide and hydrogen. Syngas can be upgraded further to valuable chemicals and fuels through methanol synthesis (MS) and Fischer-Tropsch synthesis (FTS). By the reaction of carbon dioxide and hydrogen, Sabatier reaction (SR) and direct methanol synthesis (DMS) are

possible to generate renewable natural gas (RNG) or synthetic natural gas (SNG) and methanol, respectively. The conversion of CO_2 which is in an abundant quantity in the atmosphere to valuable products that can be furthermore sold to consumers is the main advantage of the above mention reactions.

The major challenge is to design a reactor that can efficiently supply or remove heat depending on the reaction. Moreover, the catalyst takes an important place in thermocatalytic reactions and the catalyst's deactivation can occur during the reaction. Therefore, it is essential to find a stable, low-cost catalyst to make an industrial implementation possible. Commercially available catalysts are commonly based on transition metals (e.g., Ni, Cu, Cr, Fe) [3]. But there are not suitable for CO_2 conversion because the superior catalytic activity is needed to activate the CO_2 molecule which transition metals are lacking. Secondly, the catalyst deactivation occurs due to coking. Therefore, certain types of reactors are commonly used such as fixed bed and fluidized bed reactors. However, these reactors have their drawbacks due to thermal management that requires an innovative reactor design. For example, a reactor that can combine endothermic and exothermic reactions and separates steps into one highly efficient catalytic unit. The design of the reactor requires modeling and optimization as well as the commercialization can take some time, but the potential is huge to provide an optimal solution for CO_2 conversion into synthetic fuels [3].

2.2.2 Reverse water gas shift

The reaction is a mildly endothermic reaction (Eq.4):

$$CO_2 + H_2 \rightleftharpoons CO + H_2O \qquad\qquad \Delta H^{\circ}_{298} = +41.2 \text{ kJ/mol} \qquad\qquad (4)$$

During the reaction, some competitive pathways are possible such as Sabatier reaction and CO methanation (Eq.5-6):

$$CO_2 + 4H_2 \rightleftharpoons CH_4 + 2H_2O \qquad\qquad \Delta H^{\circ}_{298} = -164.9 \text{ kJ/mol} \qquad\qquad (5)$$

$$CO + 3H_2 \rightleftharpoons CH_4 + H_2O \qquad\qquad \Delta H^{\circ}_{298} = -206.1 \text{ kJ/mol} \qquad\qquad (6)$$

As for the reaction, the high CO_2 conversion can be reached at high temperatures (600–750 °C) [8] due to the endothermic nature. However, there are some limitations for the elevated temperatures as it can lead to catalyst deactivation and loss of selectivity to CO leading to CH_4 formation [5]. Therefore, it is very important to add heat efficiently in order to keep the reaction going. As well as for the catalyst to remain active during the reaction to avoid deactivation and selective to CO to avoid the formation of undesirable products. There is a challenge to make an inexpensive and stable catalyst because the selectivity depends on the support and catalytic materials.

The RWGS is a reversible reaction and the water gas shift (WGS), Eq.7, is also active during the RWGS:

$$CO + H_2O \rightleftharpoons CO_2 + H_2 \qquad\qquad \Delta H^{\circ}_{298} = -41.2 \text{ kJ/mol} \qquad\qquad (7)$$
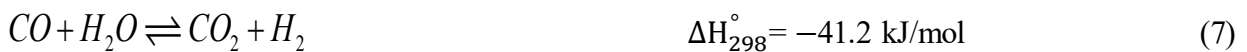
Therefore, catalysts that can be used for WGS can be implemented for RWGS. For example, Cu-based catalysts that are successfully implemented and commercially available for the WGS are being investigated for the RWGS reaction [5]. Cu-based catalysts are selective to the CO formation, but the pathway strongly depends on the active phase and support. These catalysts are normally operated at low temperatures, however, the temperatures above 900 K are required to achieve high CO_2 conversion. As for temperature above 900 K, the deactivation of Cu-based catalysts occurs rapidly by sintering. Various approaches have been made to improve the catalytic

activity such as modification of support with promoters, the addition of noble metals, and new active phase formations.

2.3 Catalysts for reverse water gas shift reaction

2.3.1 Noble metal catalysts

Some of the noble metals such as Pt, Pd, and Rh are active during reverse water gas shift reaction. In the study of Liang et al. the 2 wt% Pt catalyst supported on mullite $(Al(NO_3)_3 \cdot 9H_2O)$ in a feed gas $(CO_2/H_2/N_2 = 45/45/10)$ at a flow rate of 50 ml min^{-1} (STP) was investigated. The initial conversion of CO_2 at 550 °C was around 22.9%, while the selectivity to CO went down to 85% at higher temperatures [12]. Under the same conditions but with potassium promotion, the conversion of CO_2 reached 30% with the selectivity to CO at 100% in the range of temperature from 300-550 °C [12]. The addition of the promoter weakened the strength of CO adsorption and improved the generation of formate species from CO_2 hydrogenation. These formate species were decomposed to CO, therefore, it led to a new pathway for CO generation [12].

Choi et al. investigated 5 wt% Pd catalyst supported on Al_2O_3 [13]. The RWGS was conducted at the temperature range of 600-900 °C with H_2/CO_2 ratio from 1 to 3 as shown in Fig. 5 [13]. The following results showed the conversion of CO_2 and selectivity to CO on the Pd based catalyst. The obtained experimental conversion was close to the equilibrium conversion where the highest conversion was obtained at 900 °C and with the ratio H_2:CO_2 (1:3), equals 78% [13]. While the selectivity to CO of Pd decreased with the increase of the feeding ratio due to the formation of CH_4 at 600-700 °C [13]. It can be explained by the ability of H_2 dissociation, noble metals have high activity towards H_2 dissociation compare to the other metals, and provide the formation of CH_4 that can be obtained at T ⩽ 700 °C.
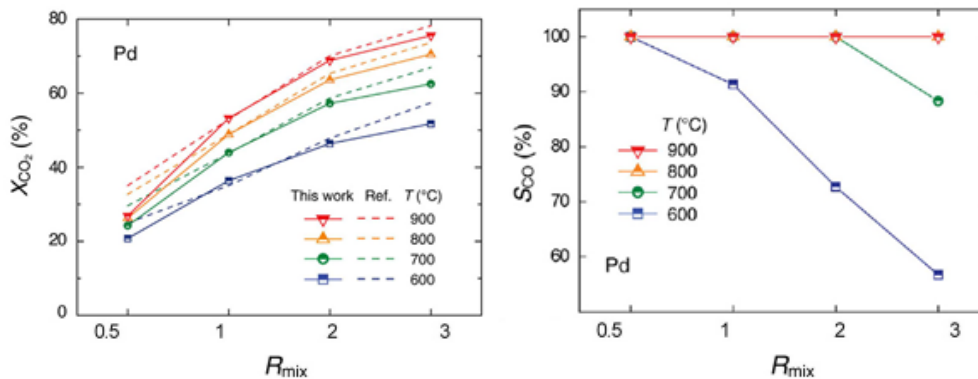
Fig. 5 CO_2 conversion and selectivity to CO of Pd/Al_2O_3 at different temperatures and H_2/CO_2 ratios [13].

Bando et al. studied Rh-based catalysts on SiO_2 for CO_2 hydrogenation [14]. The hydroxyl groups increased the surface surrounding Rh particles on the catalyst surface leading to an increase in CO_2 conversion and selectivity to CO [14]. The study shows that the formation of carbonyl clusters on Rh increased the production of CO [14].

2.3.2 Transition and metallic catalysts

Transition metals such as Fe, Ni are widely used in commercial WGS reaction and these metals also can be applied for the RWGS reaction [15-17]. Metal layered oxide catalysts are investigated for RWGS and these catalysts are highly stable and active [16, 17]. Wang et al. looked at the layered K-Fe-Ti oxide catalyst [17]. The 0.8K–2.4Fe–1.3Ti catalyst showed high stability. This is related to the reduction of Fe_3O_4, which is the active phase for RWGS, and promotion by potassium [17]. The catalyst was stable for 202 h on stream during the reaction with relatively high CO_2 conversion around 40% and good selectivity to olefins. The selectivity to CO decreased after some time due to the pretreatment step by acid [17]. The interaction between Fe and Ti was reduced which led to the formation of iron carbides and the shift to the RWGS reaction, which resulted in the high CO_2 conversion [17].

One of the biggest limitations of the RWGS is the low space velocity needed to achieve high performance [16]. In the paper of Pastor-Pérez et al. this dependency can be clearly seen when the temperature is around 600-700 °C as the conversion is close to the equilibrium [16]. In Fig. 6, various alumina-based catalysts were evaluated in terms of CO_2 conversion. The catalyst performances are ranked as following: Fe-Cu-Cs/Al_2O_3 > Fe-Cu/Al_2O_3 > Fe-Cs/Al_2O_3 > Fe/Al_2O_3. Fe-Cu-Cs/Al_2O_3. Fe-Cu-Cs/Al_2O_3 is the most active and selective material which led to a constant 100% selectivity to CO in the given temperature range [16]. This trend can be observed for copper-containing catalysts which have been reported to be activated by high hydrogen partial pressures [16]. Overall, it seems that Cs promotion along with the addition of Cu resulted in a very positive effect for the CO_2 conversion [16].
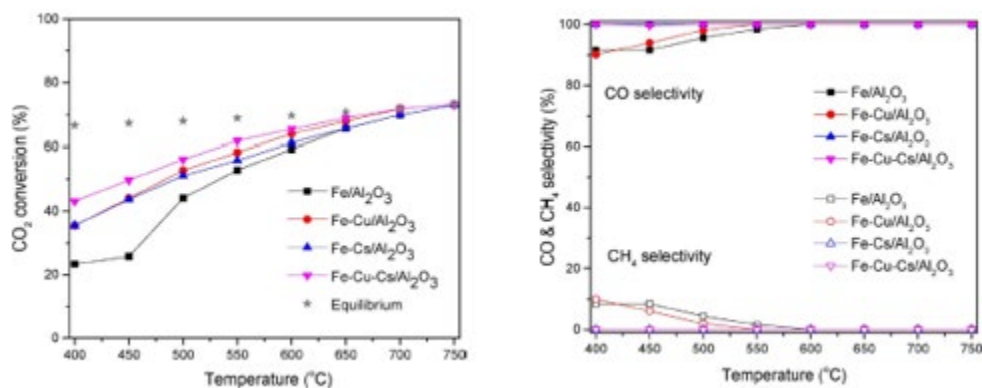
Fig. 6 CO_2 conversion and selectivity to CO and CH_4 at different temperatures. Reaction conditions: weight hourly space velocity (WHSV) of 12,500 mL/g^{-1} h^{-1} with a H_2/CO_2 ratio of 4:1, 400-750 °C [16].

The study of Sun et al. investigated 3 wt% Ni/Ce-Zr-O catalyst that showed stability over 80 h and high selectivity to CO at 750 °C [18]. The conversion of CO_2 was the highest around 50 % at 750 °C due to endothermic nature of RWGS reaction. As reported the activity of the catalyst

depends on the crystallite size, however, highly-dispersed 1 wt% Ni did not perform well due to the low content of Ni [18]. Therefore, the enhanced conversion and high selectivity can be explained by the high interference between Ni and support [18].

Fe/Al_2O_3 catalyst in the paper of Sengupta et al. was doped by Co and Ni separately, the synergism of Co^{2+} or Ni^{2+} with Fe^{2+} and Fe^{3+} in Fe_3O_4 species helped to improve RWGS activity [15]. However, this increase can be seen only at low temperatures, while with the rise of the temperature there are no noticeable changes in CO yields. Among the doped catalysts, Co-Fe/Al_2O_3 showed a high CO yield (48%) at 650 °C [15]. This is explained by the formation of the mixed oxide phase, which increased the reducibility of the iron-oxide catalyst [15]. At the same time, the alumina support is considered as a key element to sustain catalyst performance in the high-temperature region [15].

In the study of Yang et al. the Fe based catalysts were doped by Mo, Ni, Cu and evaluated on CeAl support [8]. As a result, the addition of Ni and Cu had a great overall effect on conversion [8]. However, Ni showed a decrease in the selectivity towards CO, while Cu boosted the activity and selectivity towards CO more than 95% [8]. High-performance of Fe-Cu/CeO_2-Al_2O_3 catalyst relied on its high-efficiency at medium to low temperatures. Therefore, the authors concluded that the Cu based catalysts are an excellent choice for RWGS.

Table 1 Catalytic performance of metallic and transition catalysts synthesized by different methods in terms of CO_2 conversion (X_{CO2}) and selectivity to CO generation (S_{CO}). L_{Me} is metal loading. Synthesis methods included are insipient wetness impregnation (IWI), co-precipitation (CP), high-temperature calcination (HTC).

catalyst	synthesis	reaction conditions				X_{CO_2}, %	S_{CO}, %	ref.
		T, °C	P, MPa	H_2/CO_2	GHSV, mL/(g h)			
$K_{0.8}Fe_{0.8}Ti_{1.3}O_{16}$	HTC	400	2	3:1	100,000	12	80	[17]
15 wt. Fe-Cu-Cs/Al_2O_3	IWI	400	0.1	4:1	25,000	40	99	[16]
15 wt. Fe-Cu/Al_2O_3	IWI	400	0.1	4:1	12,500	37	90	[16]
1 wt. Ni/Ce-ZrO	CP	600	0.1	1:1	28,000	37	75	[18]
3 wt. Ni/Ce-ZrO	CP	600	0.1	1:1	28,000	40	85	[18]
1.5 wt. Co-Fe/Al_2O_3	IWI	600	0.1	1:1	60,000	50	48	[15]
1.5 wt. Ni-Fe/Al_2O_3	IWI	600	0.1	1:1	60,000	NA	30	[15]
25 wt. Fe-Cu/CeO_2-Al_2O_3	IWI	500	0.1	4:1	30,000	45	95	[8]

2.3.3 Cu-based catalysts

Copper-based catalysts are commercial for the WGS reaction, which is also widely investigated for RWGS due to excellent activity and selectivity [5]. In Zhang et al. study the high catalytic activity was reached due to the high dispersion of Cu species on the β-Mo_2C [19].In Fig 7, the selectivity to CO and conversion of CO_2 were investigated for different loadings of Cu/β-Mo_2C and Cu/ZnO/Al_2O_3. 1 wt% Cu/β-Mo_2C. The resulting catalysts showed great stability (with the following conditions 600 °C, weighted hourly space velocity (WHSV) of 300 000 mL/g/h in 40 hours, maintaining 85% of activity over 40 hours [19]. Compare to the Cu/ZnO/Al_2O_3 catalyst that lost more than 60% of its original activity (from 42.5% to 15%) within 15 h reaction under the same reaction conditions [19]. Interestingly, all the copper-based catalysts maintained high selectivity to CO [19].

15
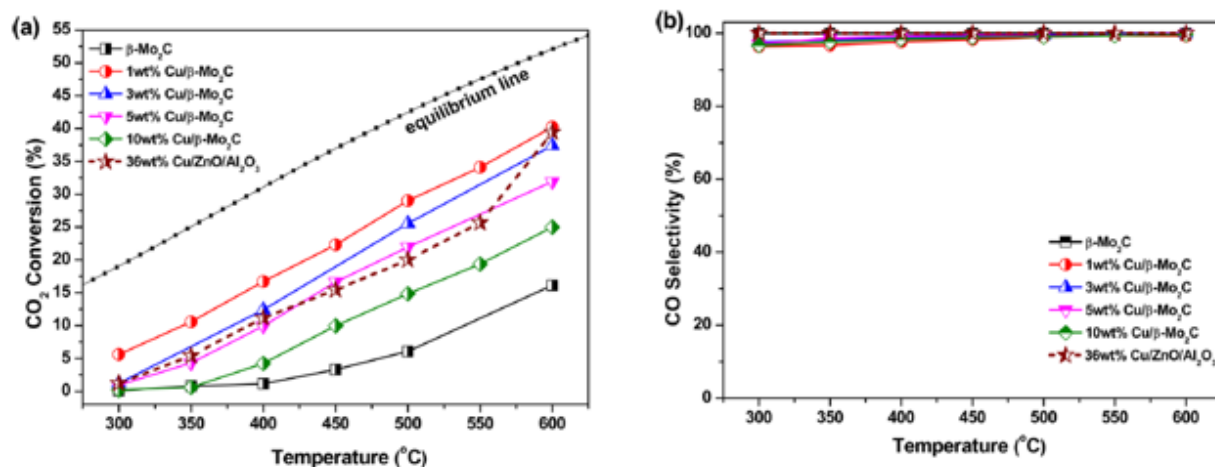
Fig. 7 a) CO_2 conversion and (b) CO selectivity of β-Mo_2C, Cu-modified β-Mo_2C and Cu/ZnO/Al_2O_3 catalysts in the RWGS reaction. Reaction conditions: atmospheric pressure, 300−600°C, CO_2:H_2=1:2, WHSV= 300,000 mL/(g h) [19].

While in some studies the use of promoters is essential to achieve high stability over highly dispersed Cu on the support [20], [21]. In the paper of Lin et al. the performance of copper-ceria catalyst promoted by Fe was evaluated [21]. When Fe was added to copper iron oxides the catalyst achieved high stability and oxygen mobility which leads to increase RWGS activity [22]. As a result, Cu promotes high selectivity to CO, while Fe oxide improves the stability and CO_2 adsorption [22]. As Cu/CeO_2 catalyst showed the loss of about 35% of its activity in 40 h despite the availability of strong support CeO_2, a reducible oxide that can anchor metal centers using strong metal-support interaction [21]. That happened due to Cu-based catalysts deactivation at 600 °C in the RWGS reaction [21]. As a result, doping the copper catalyst under the reaction conditions of CO_2:H_2:N_2 = 3:3:4 with a weight hourly space velocity of 600,000 ml g^{-1} h^{-1} 5Cu-1.6Fe/CeO_2 didn't show rapid deactivation [21]. Highly dispersed FeO_x prevents the inter-particle aggregation of metallic Cu, therefore the obtained catalyst is rather stable at high temperatures [21]. In the

16

following Bansode et al. study the Cu/Al_2O_3, the reaction was conducted at low temperatures and high pressure. Additionally, the copper based catalyst was promoted by Ba and K [20]. As for this case, RWGS is selective to CO at high temperatures due to the endothermic nature of the reaction. Therefore, K promotes selectivity to CO at low temperatures, on the other hand, Ba increases furthermore selectivity to methanol [20]. Potassium covered both support and Cu active sites creating specific sites and favoring the RWGS pathway [20]. For the potassium promoted Cu/Al_2O_3, the selectivity to CO was relatively high above 503 K from 0.4 to 36 MPa. On the contrary, Barium covered only support surface and left Cu aside making them more reducible, therefore promoting methanol synthesis [20].

In the study of Bahmanpour et al. the spinel oxide Cu-Al and Co-Al catalysts were investigated [23]. Cu-Al outperformed Co-Al despite its lower surface are and larger crystallite size [23]. The concentration of oxygen vacancies was shown as a crucial parameter to control the reaction, when spinal oxide catalysts are studied for CO_2 activation [23].

2.3.4 Support effects

In most studies, the activity of the catalyst is related to the active metal, and as for support the specific area and dispersion are investigated rather than mechanism [24]. However, the role of support is more complex and can affect the overall reaction rate. Jurković et al. looked at the most studied, highly active, and low-price copper catalysts supported on Al_2O_3, CeO_2, SiO_2, TiO_2, and ZrO_2 [24]. The Cu content was $Al_2O_3 > TiO_2 > SiO_2 > CeO_2 > ZrO_2$ from highest to the lowest, while the dispersion was $Al_2O_3 > ZrO_2 > CeO_2 > TiO_2 > SiO_2$ [24]. Interestingly, the catalyst activity was $Al_2O_3 > CeO_2 > TiO_2 > SiO_2 > ZrO_2$. The most active support to be alumina, while zirconia was the worst one with the lowest Cu dispersion [24]. However, the activity of Cu/Al_2O_3 was decreased with the increase of H_2/CO_2 ratio, possibly due to the presence of copper species on the catalyst,

17

while CeO$_2$ can be very beneficial to RWGS because of the ability to store oxygen and its reducibility as shown in Fig.8 [24]. It can be seen that support influences on the reaction mechanism for RWGS which at the same time dependent on the reactant ratio and pressure.
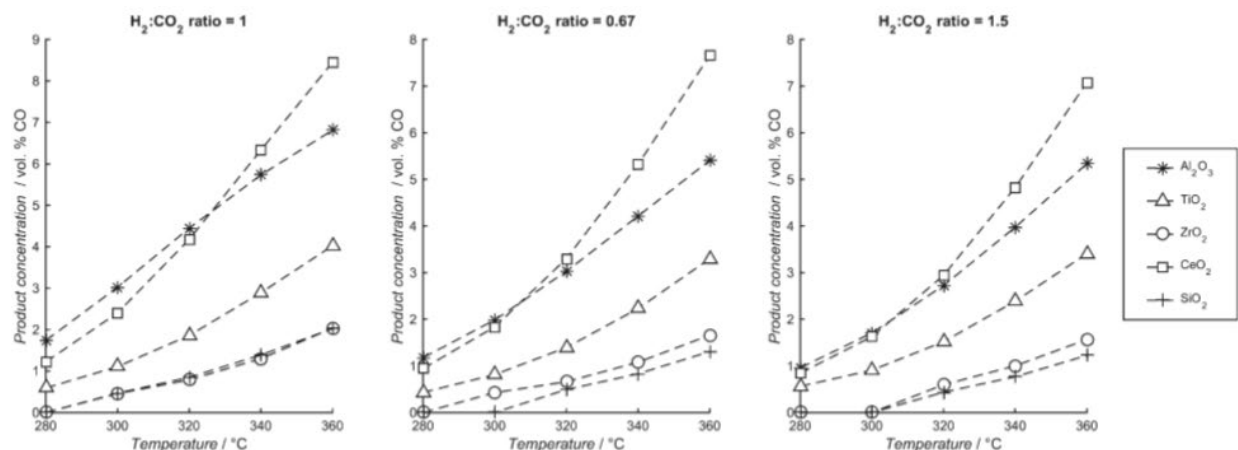
Fig. 8 CO concentration with different H$_2$/CO$_2$ ratios: H$_2$:CO$_2$=1, H$_2$:CO$_2$=0.67, H$_2$:CO$_2$=1.5. Reaction conditions: pressure 3 bars, 280−360°C [24].

Sakura et al. studied Au supported on ZnO, Fe$_2$O$_3$, Al$_2$O$_3$ and TiO$_2$ for RWGS under pressure 1 and 50 bar, respectively [25]. In this study, the most active support was TiO$_2$ for 1 and 50 bar [25]. While active at 1 bar Fe$_2$O$_3$ and Al$_2$O$_3$ lost their activity at high pressure [25]. At the same time, ZnO showed the lowest activity during the reaction conditions [25].

2.4 Reverse microemulsion method

2.4.1 Reverse microemulsion method for nanoparticles preparation

Microemulsions are considered as micro-heterogeneous systems in liquid phases either 'water in oil' or 'oil in water' which are stabilized by amphiphiles that help to lower the interfacial tension between oil and water by their interfacial adsorption [26]. As an alternative, the surfactant can separate layers of water and oil. However, the water-oil side is more complex than it seems to

18

be. Microemulsions are complicated systems because of the presence of at least four components in them as well as because of the contribution of layers to the free energy of the system and the existence of the electric double layer surrounding the droplets. As a result, final microemulsions are low viscous, isotropic, transparent, and stable solutions with an average particle size of around 5-100 nm [26]. One special trait of microemulsions is called 'phase inversion' that occurs at a given water-to-oil concentration ratio [27]. For example, if the water content is low the microemulsion is made of water droplets dispersed in oil, while if the water content is high the situation is reversed, oil droplets dispersed in water [27]. A phase diagram of a microemulsion made by Prince (1977) is presented in Fig. 9 [27].
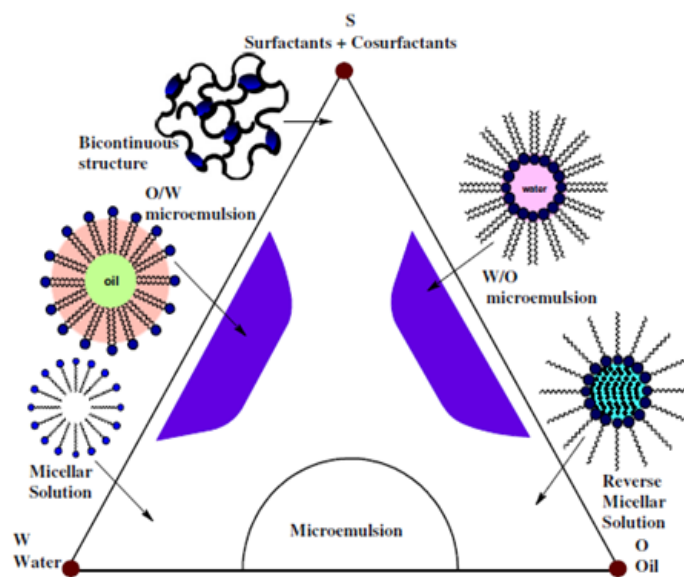
Fig. 9 Phase regions of microemulsions [27].

As for the shape, the water-oil region is unusual, it changes water-oil droplets to a cylindrical shape along with the line of where surfactant moves to a region, where microemulsion is not stable. A mixture of oil (O), water (W) and surfactant (S) has four variables such as pressure, temperature and two composition variables [27]. However, the effect of pressure is relatively small compared to temperature and two compositional variables.

Several variants of the synthesis of nanoparticles in microemulsions exist which differ from each other in the introduction of the reactants. The most common version is a mix of two microemulsions with dissolved reactants in their aqueous pseudophases, where reverse micelles in solutions include solubilized reactants, but don't contain water [28]. In the next method, this microemulsion is prepared by mixing one reactant in the solution of the other in water or oil. However, during this procedure, a stable microemulsion is not always formed, but at the same time, particles with narrow size distribution can be made [28]. Also, while preparing microemulsions the reaction can be stimulated by heat, electromagnetic radiation or bubbling through as a gas [28].

Moreover, the synthesis of nanoparticles does not always involve chemical reactions in reverse micelles [28]. The changes in the structure of reverse micelles can result in solid dispersion to form nanoparticles. The transition of reactants from one solid phase to another and the dispersion of the reaction product can be conducted by the solutions of reverse micelles. It includes special procedures of reactant blending: the constant rate of pouring one microemulsion into another one, slow pouring of a reactant or its solution into the microemulsion, slow pouring of the microemulsion into the third one and pouring of two aqueous solutions into a microemulsion [28]. If the metal ion used, there are two ways to prepare microemulsion such as using a solution of its salt in microemulsion' preparation and using an ionic surfactant where the counter ion takes place in the reaction [28].

Reverse microemulsions are mainly used to synthesize inorganic nanoparticles such as metals, salts, oxides [28]. Nanoparticles of organic compounds are rarely synthesized in the reverse microemulsion. For instance, salt nanoparticles are synthesized by ion-exchange reactions, while metal nanoparticles and oxides are synthesized by the reduction of their compounds and by the

hydrolysis, respectively. Some particles synthesized in reverse microemulsions can be required to undergo an additional treatment such as ferromagnets and high superconductors.

The example of nanoparticle formation is described below. In the paper of Li et al., the preparation of CaP/pDNA nanoparticles by reverse microemulsion method is shown in Fig. 10 [29]. The following procedures and materials were used: Triton X-100 and Butanol were used as emulsifiers; Hexane was used as an oil phase; pDNA and calcium chloride solution was poured into the oil phase and stirred for an hour to prepare microemulsion №1 [29]. The same way Na_3PO_4 was poured into the oil phase and mixed for an hour to prepare microemulsion №2. Then both microemulsions were added and stirred together for 12 h. After that, the ethyl alcohol was added to break down the formed emulsion, following the centrifugation. Then sediments were resuspended in redistilled water after washing in ethyl alcohol three times [29].
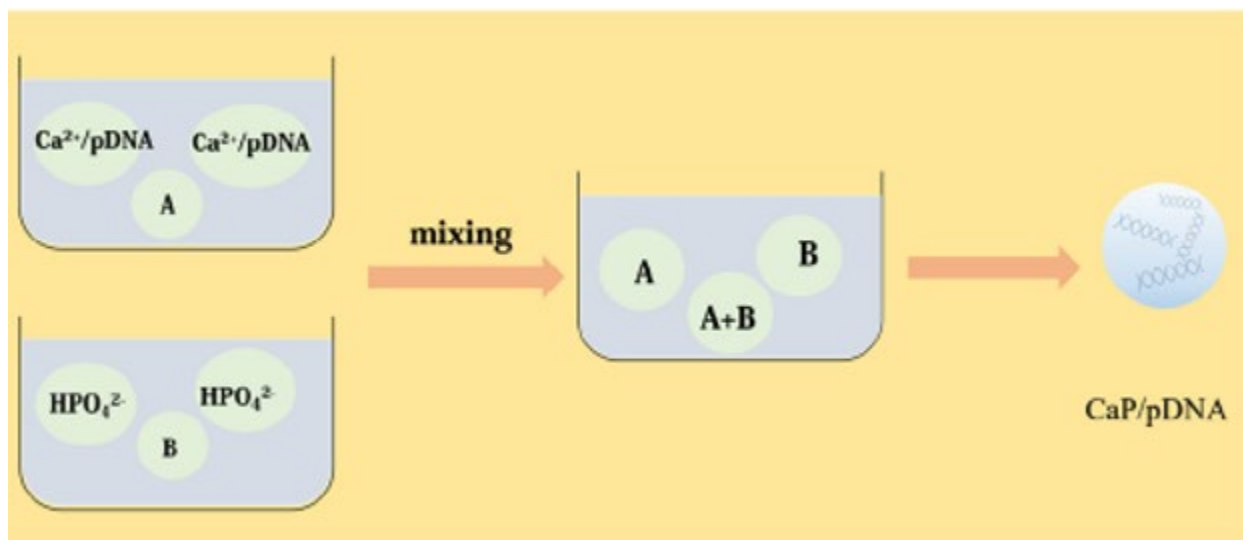
Fig. 10 The schematic diagram of nanoparticles preparation by reverse microemulsion [29].

2.4.2 Reverse microemulsion method for catalyst synthesis

The choice of synthesized substances is crucial to determine the practical use in the future[28]. Formerly, synthesis in reverse micelles to form nanoparticles was used to obtain catalysts [28]. This synthesis allows producing fine particles with large surface-to-volume ratios which are the major factor for the evaluation of catalyst efficiency [28]. The synthesis in reverse micelle allows the components to be effectively mixed on the nanoscale.

In Fig. 11, the main procedures for the catalyst synthesis by the reverse microemulsion method include [30],[31],[32]: 1) the preparation of the microemulsion- a surfactant, an oil phase, and an aqueous solution are mixed under the constant stirring until transparent to make one microemulsion [30]. In some cases, two types of surfactants can be used as ionic and non-ionic or co-surfactant with the chemicals above [31],[32]. Then the second microemulsion is made the same way. 2) reduction within the reverse microemulsion- the reduction occurs when the solution is added to the mixture of the oil phase and the surfactant [30]. The reduction is also conducted by the addition of the other chemicals such as hydrazine. The change of the color in the solution indicates the reduction in ions [31]. 3) hydrolysis- the first microemulsion was added to the second one dropwise and stirred for some hours [30]. The precipitations were obtained within the reverse micelle. Sometimes, the hydrolysis reaction occurs slowly at room temperature, by the gradual reduction in the transparency of the mixture [32]. 4) dispersion- then in some cases, the calculated amount of carbon black was added to the mixture and stirred for several hours to ensure homogeneous dispersion of nanoparticles [30], [31]. In some situations, an additional stage of aging can take place, the final mixture with a low water content (1-5 wt%) can be stirred for 1-48 hours to gain phase separation, while a high water content (>10 wt%) remain stable under the aging [32]. After aging particles can be recovered from the microemulsions using various techniques

22

[32]. For example, the phase separation can be triggered by cooling to -5 °C [32]. 5) heat treatment and particles processing-after that carbon-supported nanoparticles can be precipitated by acetone, washed repeatedly with ethanol and acetone to remove surfactant, dried and heated at chosen temperatures under N_2 gas, air or H_2/N_2 mixture [32],[31]. After heat treatment, obtained particles can be crushed to the fine powder. Sometimes liquids for washing may vary, for example, the combination of water and acetone or water and ethanol [30]. To separate phases, several techniques can be used such as filtration, centrifugation, roto-evaporation, and freeze-drying [32]. While filtration wasn't effective since ultrafine particles were lost, the centrifugation and roto-evaportaion are failed to recover particles without causing agglomeration [32]. As for freezing-drying, it is an alternative approach that was described in the paper of Zarur et al [32]. 6) calcination and crystallization- then the obtained powder is heated up to the desired temperature in the oven to get rid of surfactant, hydrocarbons, and so on [32]. The heating can be carried under the flowing air or N_2 for several hours to obtain a desirable crystalline catalyst [32]. The method of preparation can be optimized varying different parameters such as the temperature, time and etc. The optimization of the process can be done with the respect to the active metal and support. For example, the calcination procedure is strongly dependent on the active metal and support's temperature and the duration time. As you change the temperature different form of oxides can be activated, therefore, it can lead to various performance. Additionally, the loading of metal and the materials for the RME preparation can be altered according to the performance needs.

The preparation of the microemulsion → Reduction within the reverse microemulsion → Hydrolysis

Calcination and crystallization ← Heat treatment and particles processing ← Dispersion
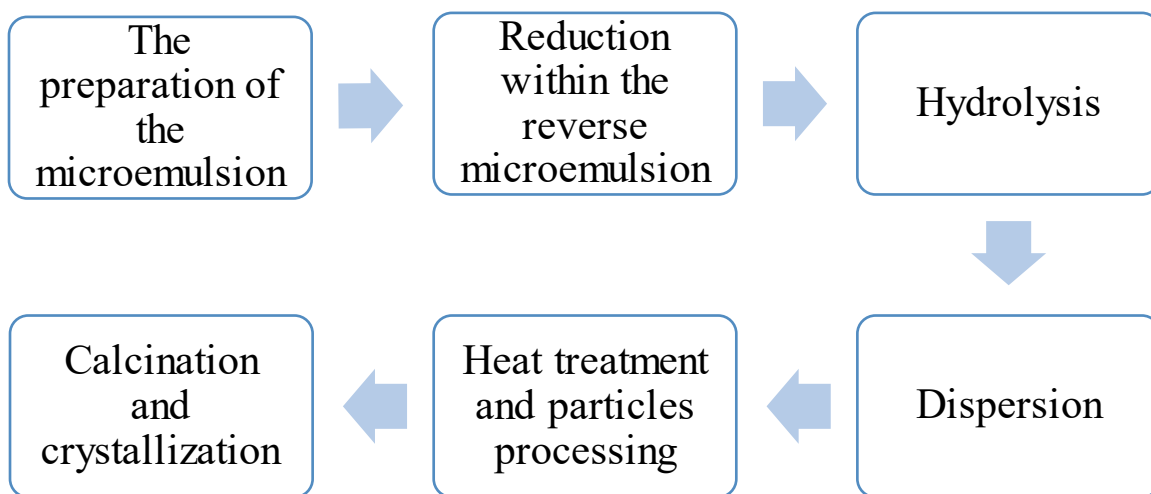
Fig. 11 Schematic diagram of the reverse microemulsion method for the synthesis of the catalyst.

Chapter 3: Methodology

3.1 X-ray powder diffraction (XRD)

X-ray diffraction is a technique that helps to analyze a wide range of materials including catalysts, plastics, metals, fluids, thin-film coatings and so on [33]. The X-ray diffraction method is used to analyze and identify the crystal structure and atomic spacing. It can be conducted on powder or crystalline samples. However, when the crystal used for the diffraction, X-rays diffracts in a pattern characteristic to its structure. For the powder, the diffraction pattern is obtained from the material. Therefore, X-ray powder diffraction is considered as an easy and convenient way to analyze the material compare to crystal diffraction [33].

A cathode-ray tube produces monochromatic radiation that collimates to concentrate the X-ray towards the sample. The interaction of rays with the sample produce the interference that appears when the conditions satisfy Bragg's law, Eq.8 [33]:

$$n\lambda = 2d \sin\theta \tag{8}$$

where n is an integer, λ is a wavelength of X-rays, d is the interplanar spacing that generates the diffraction and θ is the diffraction angle [33]. Due to this law, the wavelength of the radiation is related to the diffraction angle and the lattice spacing in the sample. Then the diffracted X-rays are being detected, analyzed, and counted. As the sample is scanned through a range of 2θ angles, the various diffraction of the powder sample can be obtained due to its random orientation. D-spacing broadens the scale because every compound has its own unique set of d-spacings. Then it can be compared by the reference patterns of d-spacing.

The X-ray diffractometer consists of the main elements such as sample holder for samples, the X-ray tube (X-ray source) and detector shown in Fig.12.
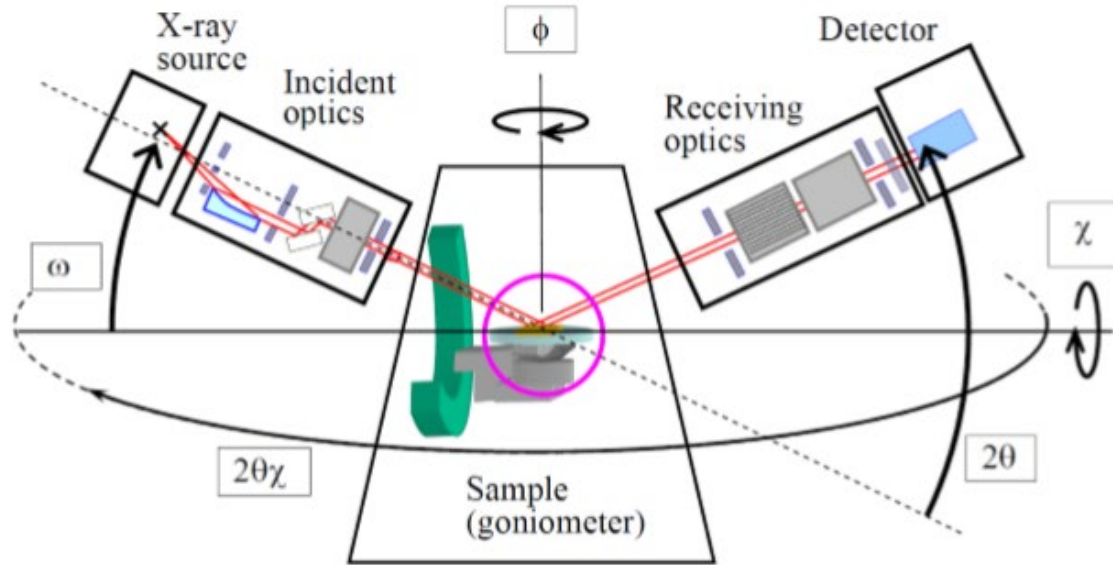
Fig. 12 Schematic diagram of X-ray diffractometer [34].

The X-rays are generated from the X-ray source in a cathode tube due to the heating of a filament that produces electrons. These electrons are accelerated to the sample by the voltage, then electrons reach the target material. When the inner shell electrons of the sample's material get displaced by electrons the X-ray spectra are made. At the same time, the sample and the detector rotate, and the intensity of the diffracted X-rays is recorded. The peak appears when the geometry of the X-rays produced by X-ray tube matches the sample ones satisfying Bragg's law. This information of the X-ray signal is recorded and processed by the detector. The obtained signal is directed to the printer or computer monitor. The goniometer is responsible for the maintenance of the angle and rotation of the sample. Typically, for the powder samples, the angle of 5° to 70° is implemented at 2θ [33]. There are certain advantages and limitations of X-ray powder diffraction. The main advantages are straightforward data interpretation, the XRD can be done in a relatively short time, the identification can be provided for the most ambiguous materials, the sample preparation is minimal [33]. The limitations are the material must be ground into the powder,

26

homogeneous and single-phase materials are favored, some compounds can be unexplored for example, some inorganic compounds, a peak may occur or worsen at a high angle [33].

3.2 Inductively coupled plasma optical emission spectrometry (ICP-OES)

ICP-OES is an analytical technique that is used for the determination of chemical elements in liquid samples. To inject liquid samples into a radiofrequency-induced argon plasma nebulizers or sample introduction methods are used. Plasma can be generated by supplying argon gas to the torch coil as well as the high-frequency electric current to the work coil at the top of the torch tube. In the torch tube, the electromagnetic field is generated by the high-frequency electric current and argon gas became ionized and therefore plasma is created. Created plasma possesses some specific traits such as high electron density and temperature (6000-10000 K) [35]. The energy of plasma is provided to the analyzed sample from the outside, through the excitement of atoms (elements). The photon wavelength is measured when the excited atoms return to the low energy position. The emitted rays match the certain photon length that can be furthermore measured. The position and the intensity of photon rays can help to determine the element type and the content of each element, consequently. The sample is introduced into plasma in an atomized state through the narrow tube in the centre of the torch tube. Then, the analyzed sample quickly dries, vaporizes and energized due to collision excitation at elevated temperatures. The atomic emission can be taken from the plasma through the mirror or lens. Then the signal is sent to the entrance slot of a wavelength selection device where the image is shown. To determine the single element the monochromator and photomultiplier tube combination can be used, while for the multiple-element determination the combination of a polychromator and an array detector is implemented.

The schematic representation of a typical ICP-OES instrumentation is shown in Fig.13.
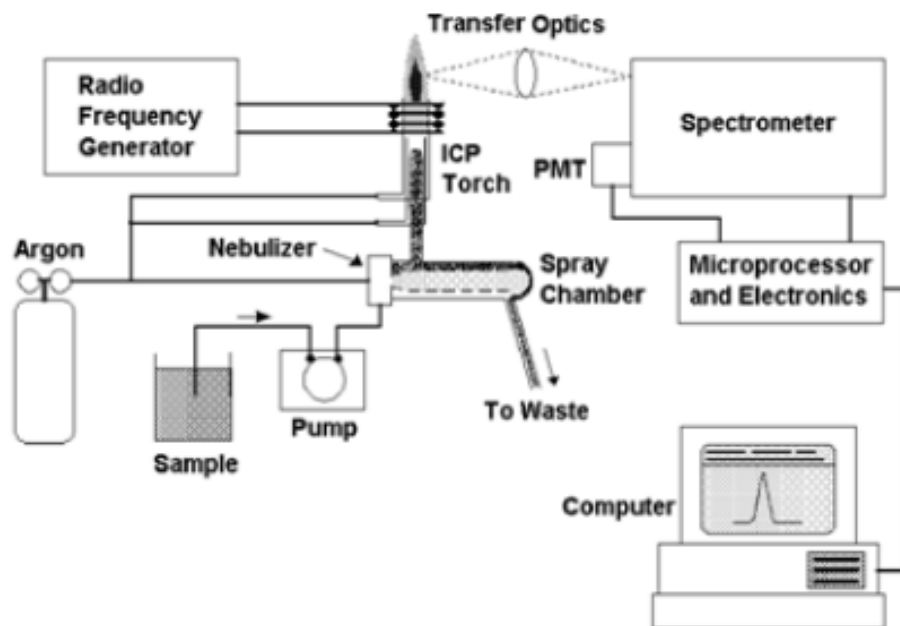
Fig. 13 Major components of a typical ICP-OES instrument [35].

In ICP-OES, the analyzed sample is transported to the instrument as steam, because inside of the instrument the liquid sample is converted into the aerosol through the nebulization in the nebulizer. At the same time, the argon gas is fed to the instrument and high-frequency current together form the plasma. The aerosol is sprayed to the instrument where the plasma is created and then the sample aerosol is desolvated, vaporized, atomized and excited by the plasma. These excited ions emit the characteristic radiation that is gathered by the device (spectrometer) that collects radiation by the wavelength. Then the radiation is turned into the electronic signal which is sent to the computer monitor.

The main benefits of ICP-OES are cost-effectiveness, high temperatures, high electron density, low background emission and chemical interference, and excellent accuracy and precision due to high stability [35].

3.3 BET Surface area analysis (SAA)

BET is a method that allows to calculate the specific surface area of the solid powder by the adsorption isotherm measurement. BET is based on the physical adsorption of an inert gas on the surface to form monolayer. This procedure is conducted at constant temperature and the amount of the adsorbate can be determined. The surface area can be calculated by the following equation, Eq.9 [36].

$$S.A. = a \frac{V_m}{V_M} N_A \tag{9}$$

where N_A is Avogadro's number, a is the surface area of one molecule of adsorbate, for a gas with molar volume V_M, for a solid with monolayer volume V_m. Furthermore, the monolayer volume V_m can be determined by the BET equation, Eq.10 [36].

$$\frac{P_i}{V_i(P - P_i)} = \frac{1}{V_m c} + \frac{c-1}{V_m c} \times \frac{P_i}{P}$$

(10)

where P is the absorbate vapor pressure at the adsorption temperature, C is a constant based on the concentration of adsorption sites, V_i and P_i are absorbed volume at given partial pressure of adsorbate.

The main procedure to get specific surface area is to measure the absorbate volumes at the adsorbate partial pressures and apply the BET equation. As the adsorbate the nitrogen gas is normally used for BET measurements at the liquid nitrogen temperature. Then the cross-sectional area of adsorbate can be found from the literature, while the partial pressure and temperature of adsorbent are measured in the BET instrument. A flow method is one of the methods for BET

surface area measurement. The procedure consists of several steps: treatment, BET adsorption/desorption and pulse calibration. The analyzed material as a solid powder or small particles is placed into a tube. Then it is set on the instrument at the position that allows a gas to pass through the tube and to get back to an analyzer. At the beginning, one-point BET is run, and the BET equation is applied to this point and its origin. After that the mixture of nitrogen and helium passes through the solid material till the flow equilibrium is reached. Then the adsorption/desorption step begins. The tube with the sample is immersed into the dewar with the liquid nitrogen inside. That carrier steam make nitrogen to condense on the walls of the tube and at the same time the signal is sent to the system to obtain an adsorption peak. When the flow equilibrium is reached again, the dewar is removed from the tube. Then the tube gets immerged into the water at the room temperature resulting in desorption of nitrogen on the walls of the tube to obtain a new signal a desorption peak. After that the last step is left, the pulse calibration where the volume term of the BET equation is obtained and the ratio of N_2/He is related to the partial pressure of the nitrogen.

The most important condition that must be satisfied to obtain the surface area is to have mesoporous solids (pores around 20 and 500 angstroms in diameter according to the IUPAC).For microporous solids the nitrogen as an adsorbate can only surface area greater than 10 m^2/gram, for lower than that the other adsorbent should be used such as krypton [37].

3.4 Scanning Electron Microscope (SEM) and SEM-EDS

The scanning electron microscope is a type of the electron microscope that can produce high-resolution images of a sample surface by scanning it with a high energy beam of electrons. While conventional light microscopes use glass lenses to bend light waves and make a magnified

image, the scanning electron microscope makes magnified images by using electrons instead of light waves. The schematic representation of SEM is shown in Fig.14.
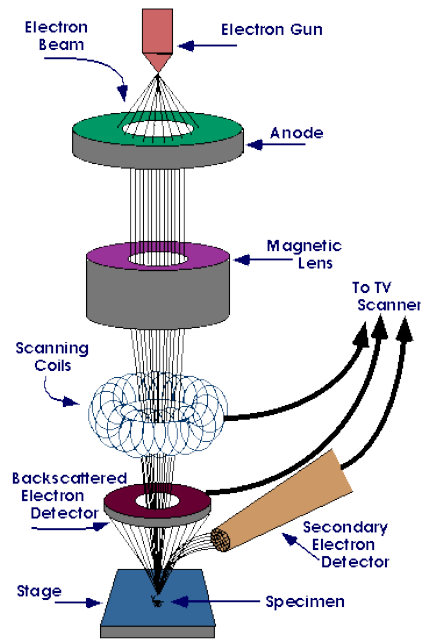
Fig. 14 Schematic diagram of SEM [38].

When the sample is placed, the electron gun emits the electron beam that passes through scanning coils or deflector plates to the final lens that reflects the beam horizontally and vertically. It allows to scan the area of sample in a raster fashion over a rectangular area. Then the electronic devices analyze and transfer the signal as an image on the cathode ray tube where the raster scanning is synchronized with the microscopic one. Then the image is displayed as a distribution map of the emitted signal from the scanned area. For the samples, the material is supposed to be conductive for the electron beam for the scanning. Normally, non-conductive materials are coated with the layer of conducting material by low vacuum sputter coating and high vacuum evaporation in order to prevent the accumulation of static electric charge on the sample during the electron irradiation. There are some SEM instruments such as Environmental SEM (ESEM) or in field emission gun (FEG) SEM that can operate on non-conductive materials without coating. SEM

31

creates highly magnified images up to ×300000, but as the images created without light waves, they are black and white [38].

Energy dispersive X-ray analysis can be used in conjunction with SEM, it can analyze near surface elements and determine the proportion at different position, therefore showing the overall mapping of the sample [38]. The electron beam strikes the surface of the sample causes X-rays emission from the material. However, the X-rays are produced in a region about 2 microns in depth. By the moving of the electron beam across the sample the whole image can be obtained. However, due to low intensity of X-ray it can take hours to get an image.

3.5 Temperature-programmed reduction (TPR)

Temperature-programmed reduction (TPR) is a characterization technique used for solid materials mostly used for heterogeneous catalysts to find the best reduction conditions, the oxidized catalyst precursor is treated with the programmed temperature rise at the same time the reducing mixture of gas passes through the catalyst. The TPR schematic diagram is shown in the picture, Fig. 16.
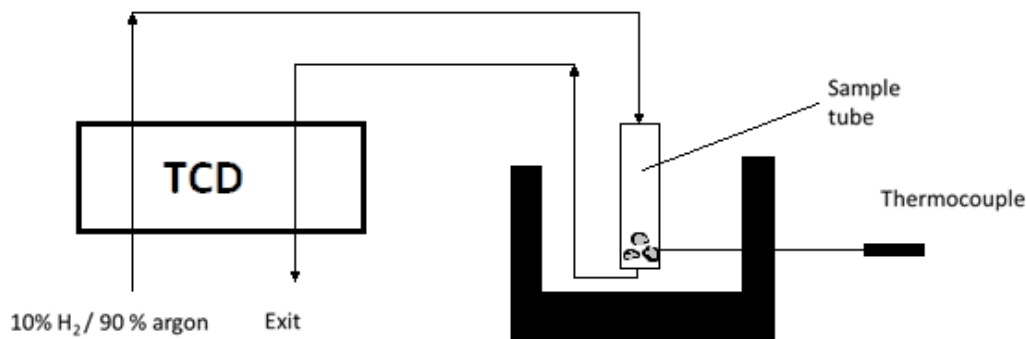
Fig. 15 TPR schematic diagram.

In the beginning, a certain amount of catalyst or solid material is placed in a sample tube in between the quartz wool (U-tube). Then the sample tube is placed in a furnace with the thermocouple to measure the temperature inside of the U-tube. The air was flushed out of the sample tube with inert gas (nitrogen, argon). The heating takes place in an inert gas until the predefined temperature is reached. Normally heating rate is around 1K/min to 20 K/min [37]. Then the reduction takes place at the forementioned temperature with the hydrogen-containing gas mixture (for example, 10% of hydrogen and 90% of argon) flowing at the constant rate through the sample [37]. Hydrogen becomes consumed, and the change in the concentration of hydrogen that passes through the U-tube is proportional to the amount of reduced catalyst. This change in the amount of hydrogen is sent to the TCD detector. Then the information is recorded on the monitor where the TPR curve is obtained. The TPR curve provides the information on the change of the metal oxidation states and the interactions between two metals and between the support and metal oxide.

3.6 CO_2 Temperature-programmed desorption (TPD)

The temperature-programmed desorption (TPD) technique is used to monitor surface interactions among substrate surface and absorbed molecules. This technique is commonly used in heterogeneous catalyst characterization. A TPD experiment can provide the information about the number of surface sites exposed and available for chemisorption especially for supported metal catalysts. The chemisorption uptake can be used to calculate the average metal crystallite size [39]. The TPD schematic diagram is shown in the picture, Fig. 17.
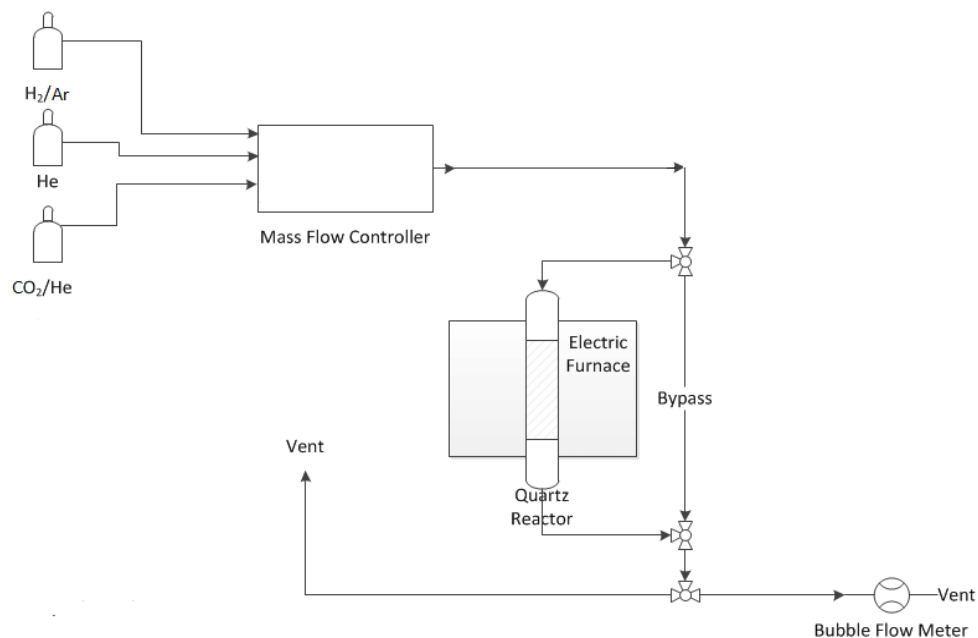
Fig. 16 TPD schematic diagram.

CO$_2$ TPD studies were conducted on (AMI-300Lite, Altamira Instruments) to determine the dispersion of the Cu/Al$_2$O$_3$ catalyst. Fresh catalyst after calcination and spent catalyst after being 18 hours on stream were analysed. About 30-40 mg of catalyst was placed in a U-shaped quartz sample tube. Prior to CO$_2$ TPD, the catalyst sample was dehydrated in He for 2 hours at 200 °C to remove the moisture. After pre-treatment, the sample was reduced in H$_2$/Ar at 350 °C for 2 hours and subsequently flushed with pure helium for 60 min to remove the excess hydrogen. After the sample was reduced, it was saturated with CO$_2$ in a flow of a 10% CO$_2$-He mixture at 20 °C. A TPD analysis was carried out from ambient temperature to 600 °C at a heating rate of 10 °C /min. The amount of CO$_2$ desorbed was calculated using Altamira Software.

3.7 Thermogravimetric Analysis (TGA)

The changes in the mass continuously measured with the temperature change over time in a thermogravimetric analyzer the instrument for TGA. Temperature, time, and mass are the main

measurements in TGA, and some additional measurements can be derived from them. The schematic diagram of TGA is shown in the picture, Fig. 17.
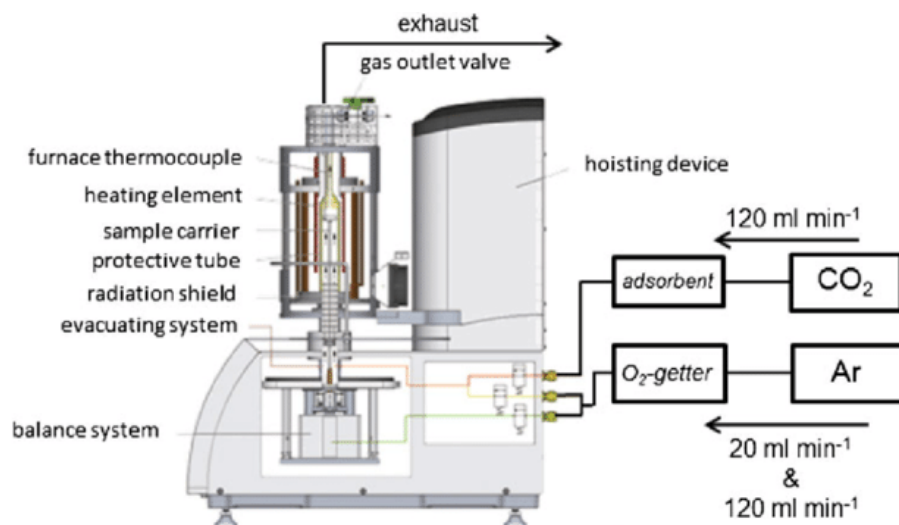
Fig. 17 The schematic diagram of TGA [40].

TGA is conducted inside of a small tube furnace. The solid sample is placed on the micro-balance and this balance is put inside of the furnace where the temperature goes up and the thermal reaction occurs. The thermal reaction can appear under a variety of atmospheres: ambient air, vacuum, inert gas, oxidizing/reducing gases, corrosive gases, carburizing gases, vapors of liquids or "self-generated atmosphere" or the variety of pressures: a high vacuum, high pressure, constant pressure, or a controlled pressure. At the same time, the sample starts to evaporate, react, or burn down inside of the chamber and the mass is determined to the nearest microgram. When the sample boils off, then the temperature of the sample becomes constant meaning that the temperature in the furnace is slightly constant. When the sample burns down, some extra heat of this reaction can be released into the oven. The heat signal is measured and reported to the analyzer. This signal can provide information about the sample kinetics and thermal stability. The sample inside of the furnace can be heated to high temperatures (600-900 °C).

TGA can give an opportunity to examine how the reactive gases interact with the sample either etch or add mass at different temperatures. Modern TGA allows to vary gas that covers sample. Therefore, it will measure the etching rate or the reaction rate of the sample material. Then obtained data is collected from the thermal reaction and as a result, the plot of mass or percentage of initial mass versus time or temperature can be gained. It is referred to the TGA curve that can be used for material characterization through the decomposition patterns.

3.8 Fourier-transform infrared spectroscopy (FTIR)

FTIR is a technique that helps to obtain an infrared spectrum of absorption or emission of liquid, solid, or gas. A spectrometer collects high-spectral-resolution information over a wide spectral range. Due to the theory of the adsorption of specific infrared wavelengths, the compound molecules vibrate. The infrared spectroscopy is based on this theory and relates to the absorption spectrum. Various parameters influence the infrared light wavelength such as chemical bond and the atomic weight of atoms connected at both ends. Generally, infrared spectroscopy is a study of the molecular structure and chemical composition. When it comes to the relationship between the position, shape, intensity, and adsorption bond of the peaks that are obtained by adsorption of infrared light, it can be concluded that there is a certain bond in the molecule. The transition type FTIR is shown in the picture, Fig. 18.
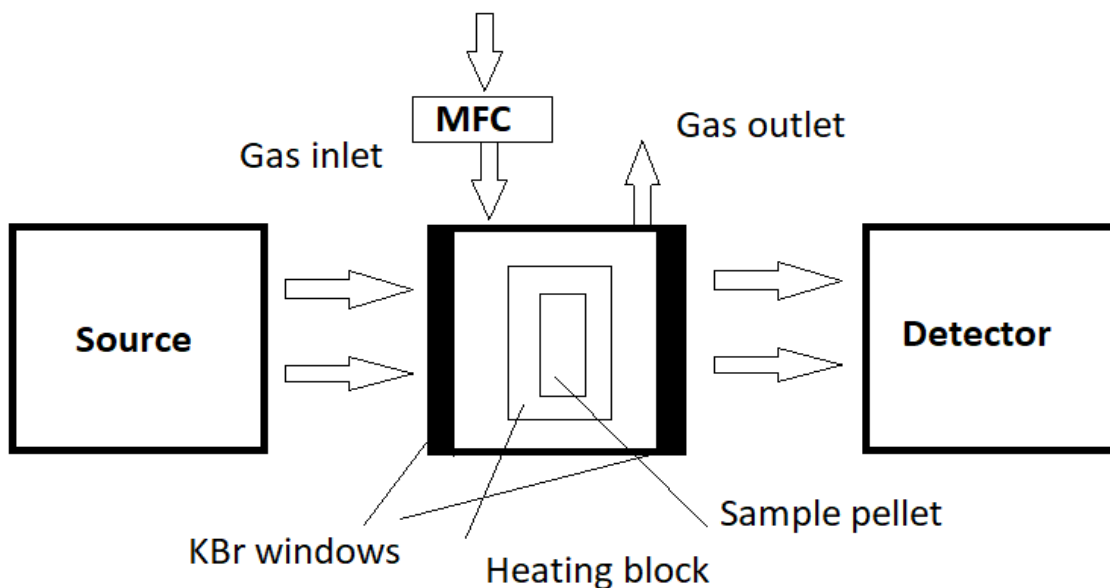
Fig. 18 The schematic diagram of in-situ FTIR.

In the transition type of FTIR, the infrared signal is created from the source that goes through a sample pellet and the KBr windows are presented at both sides of the pellet. Then the signal arrives at the detector where information is processed. Spectra can be obtained at different reaction times and temperatures to study the adsorbed species during the reaction. The gases at the outlet are continuously measured by an IR analyzer (IR-208 Infrared Industries). A multiple channel infrared detector arrays are used to analyze target gases. The infrared beam goes through a specially designed narrow band-pass optical filters and the obtained energy is limited to the specified signal. The adsorption then compared with the optical filter comparator and the concentrations can be obtained.CO_2, CH_4, and CO adsorptions are measured and processed to the digital signal to be displayed.

Chapter 4: Experiment setup

4.1 Catalyst synthesis

In this study, 25 wt% CuO/γ-Al$_2$O$_3$ was synthesized by reverse microemulsion method. The schematic diagram of the catalyst preparation is shown in the picture, Fig. 19.
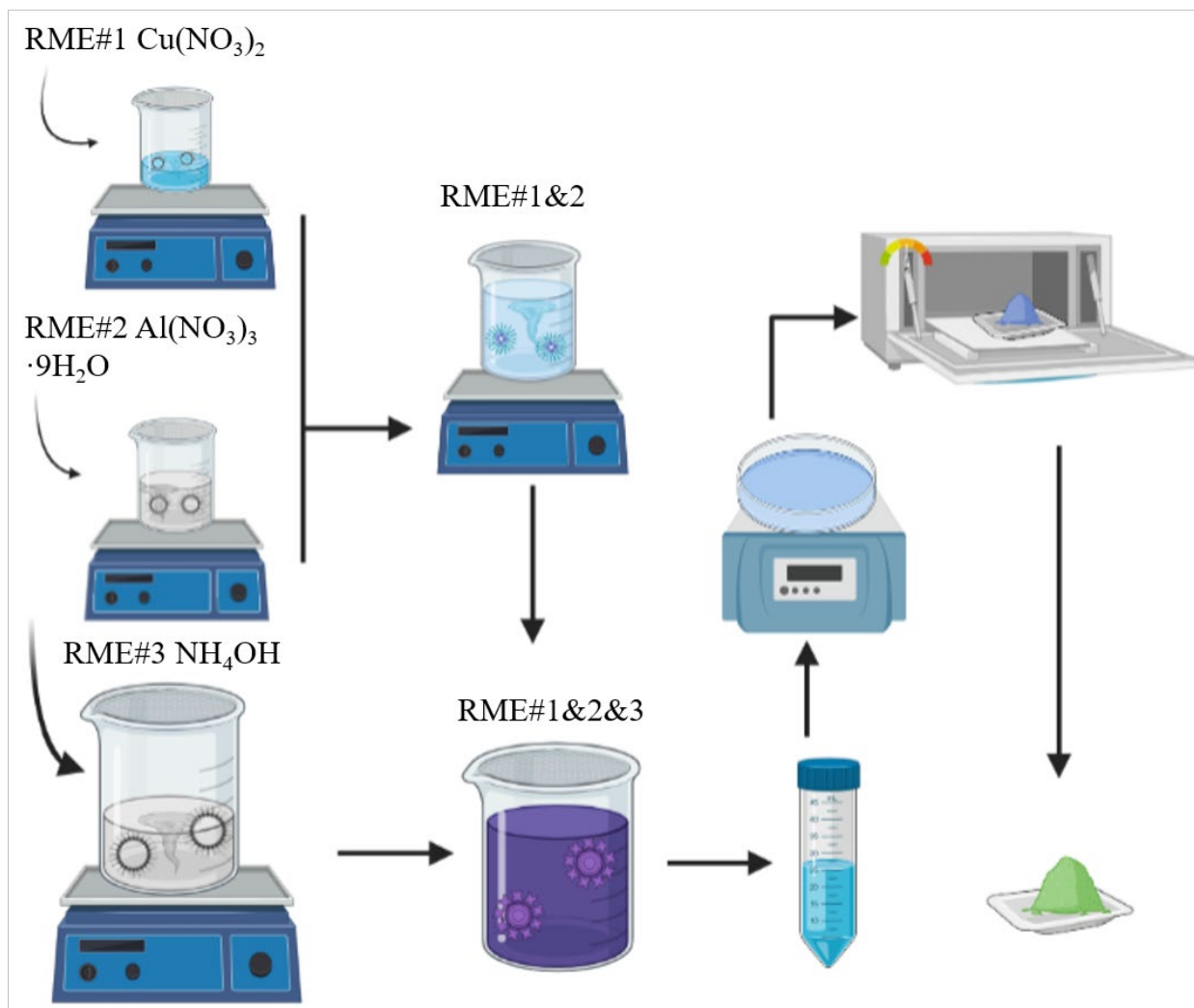
Fig. 19 Schematic process for synthesizing Cu/γ-Al$_2$O$_3$ catalyst by reverse microemulsion (RME) method.

Three blank RMEs were prepared by mixing non-ionic surfactant Triton X−100 (2− [4−(2,4,4−trimethylpentan−2−yl) phenoxy] ethanol, Acros Organics), co-surfactant propanol−2 (Sigma-Aldrich, USA), and oil phase cyclohexane, (Sigma-Aldrich, USA) under vigorous stirring. In Table 2, the ratios for RME preparation to make 1 g of catalyst are shown. The blank RMEs were used to prepare three individual RMEs containing salt (an aqueous phase), i.e. copper nitrate (Sigma-Aldrich, USA), aluminum nitrate nonahydrate (Fisher Scientific, USA), and ammonia hydrate (LabChem Inc., USA) named as RME #1, RME #2, and RME #3, respectively. RMEs were prepared while adding an aqueous phase to the blank RME solution. Aqueous phases were prepared by dissolving copper nitrate (RME#1) and aluminum nitrate nonahydrate (RME #2) in deionized water to obtain 1M solution. 1M ammonia was used directly for RME #3. After 15 min of stirring, aqueous phases were introduced to the blank RMEs dropwise. After the addition of aqueous phases, a small amount of co-surfactant was added into the RME till the RME turned transparent. The mixture of aluminum RME#1 was colorless and transparent, while the mixture of RME#2 copper was transparent and blue.

Table 2 The microemulsion system materials used for the synthesis of copper oxide supported on alumina nanoparticles

RME	Ratio	$Al(NO_3)_3$	$Cu(NO_3)_2$	Ammonium Hydroxide
Aqueous phase	3	5.5146 g $Al(NO_3)_3$ ·9H$_2$O solution 6 mL	0.7563 g Cupric Nitrate Trihydrate solution 4 mL	NH$_4$OH solution 60 mL
Surfactant	2	Triton X-100 4 mL	Triton X-100 2.7 mL	Triton X-100 40 mL
Co-surfactant	10	Propanol-2 20 mL	Propanol-2 13.3 mL	Propanol-2 200 mL
Oil phase	7	Cyclohexane 14 mL	Cyclohexane 9.3 mL	Cyclohexane 140 mL

Separately prepared copper nitrate, aluminum nitrate, and ammonia RME's were mixed in different orders as described and the changes of color and transparency are summarized in Fig.20. 1 g of the catalyst was prepared by mixing RME #1 and RME #2 first under vigorous stirring for an hour. The obtained RME #1&2 then was poured dropwise into RME #3 under stirring. The mixture of RME #1 was clear and transparent, the mixture of RME #2 was transparent and blue. Then RME #1&2 was clear and blue when the mixture was added to RME #3, the RME #1&2&3 system start to turn to dark blue because when copper(II) hydroxide reacts with a solution of ammonia, it forms a deep blue solution of tetramminecopper $[Cu(NH_3)_4]^{2+}$ complex ion [41]. It accelerates the oxidation reaction of ammonia solution in the presence of dioxygen, giving rise to copper ammine nitrites, for example, $Cu(NO_2)_2(NH_3)_n$ [41].
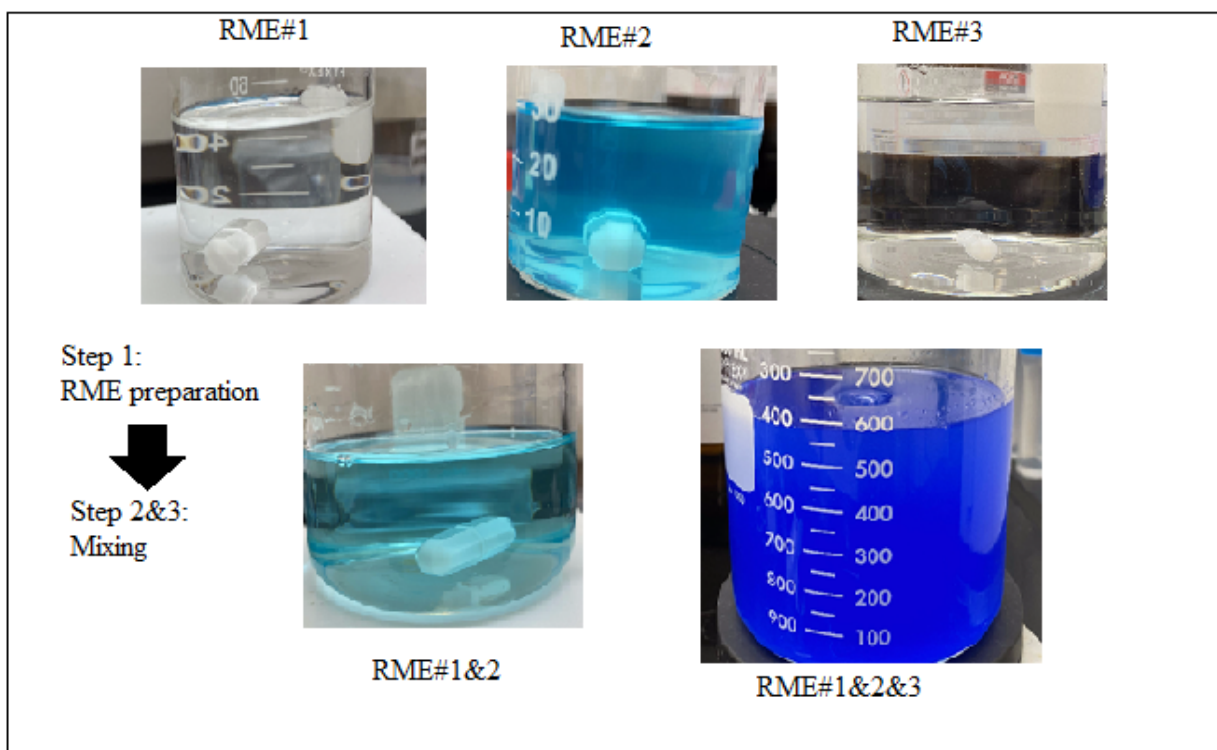
Fig. 20 RME preparation.

The precipitation was washed 4 times by ethanol and deionized water (3:1) followed by centrifugation. The precipitation was dried at 100 °C, ground to a fine powder, and calcinated at 400 °C for 6 hours with a ramping rate 10 °C/min, which leads to the formation of copper oxide. This temperature was chosen because the catalyst becomes thermally activated in the temperature range of 400–450 °C, which is high enough to obtain stable γ-Al$_2$O$_3$ (about 400 °C) and to decompose copper nitrate, which is used as a common precursor of an active phase (about 350 °C) [42].

CuO became green as shown in Fig. 21. Copper undergoes an oxidation reaction and turns green after being exposed to the air. The copper metal reacts with oxygen and forms an outer layer of copper oxide, which becomes green or bluish-green in color [43]. This layer is called the patina, which usually consists of varying mixtures of copper chlorides, sulfides, sulfates, and carbonates, depending upon conditions [43].
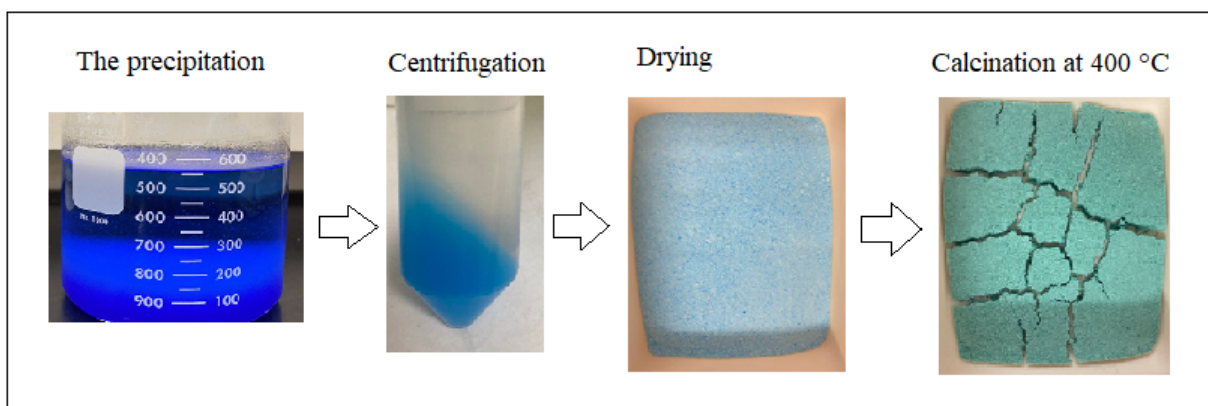
Fig. 21 CuO preparation procedure.

4.2 Flow system setup

The flow system that was used for the reactor testing is show in the picture, Fig. 22. Two mass flow controllers (TMCs) are used to control the feed CO$_2$ and H$_2$ entering the reactor. A

stainless-steel reducer (1/4" to 3/8") was used as the reactor that was coupled between a ¼"
stainless steel tube at the outlet and a 3/8" tube at the inlet. 3/8" tube was used for the easy loading
and unloading of the catalyst. Catalyst was loaded and sandwiched between quartz wool on both
sides. After catalyst was packed, the reactor system was placed in a programmable furnace
(Lindberg/Blue M™ Mini-Mite™, thermo Fisher Scientific). A K type thermocouple (1/8″,
Omega Engineering) was installed at the outlet of the reactor touching the quartz wool next to the
catalyst bed and connected to the controller (UP150, Yokogawa) of the furnace (Lindberg/Blue
M™ Mini-Mite™, thermo Fisher Scientific) for precise temperature measurement of the catalytic
bed. The reactor was placed in the middle of the furnace during the reaction. The pressure of the
system was adjusted by a back-pressure regulator (S01094789B, Swagelok) while moisture was
removed by a mist trap (AFM40-N02-Z-A, SMC Corporation) before the regulator and a silica gel
(Fisher Scientific) column after, the original adsorbent was replaced with orange silica gel, Fisher
Scientific). The concentrations of CO, CO_2 and CH_4 of the dry outlet were measured by an IR
analyzer (IR-208, Infrared Industries) continuously and monitored by an analog-to-digital
converter (USB 6008, National Instruments) and LabView (National Instruments).
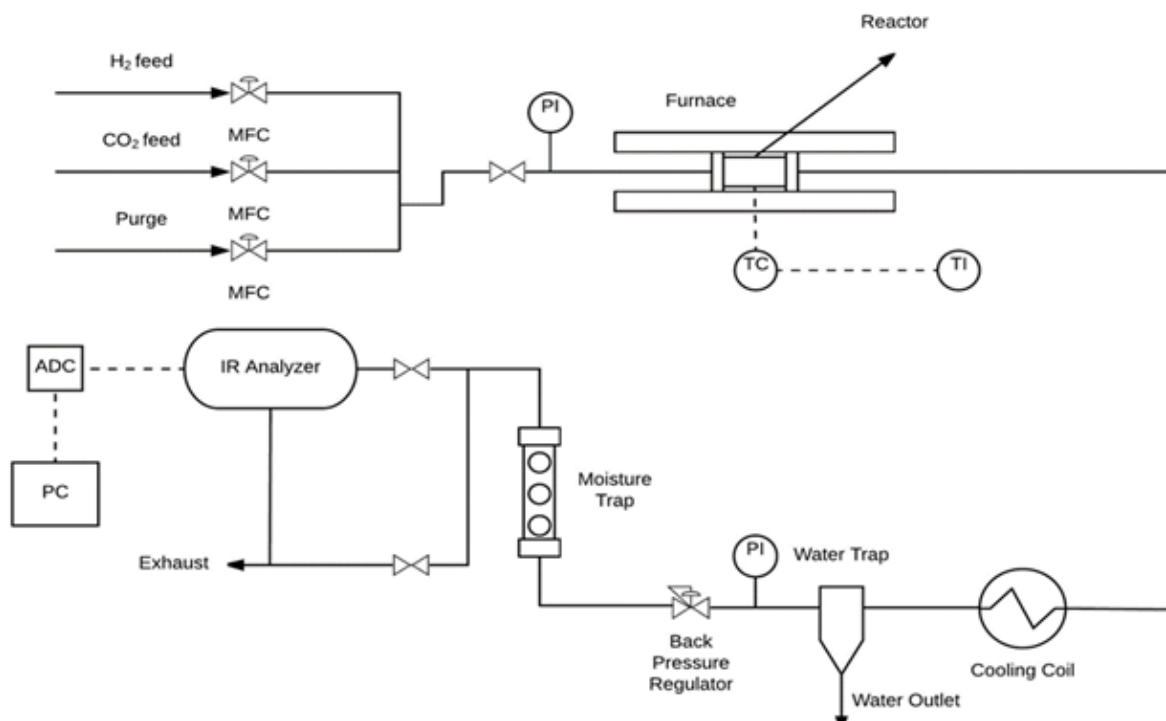
Fig. 22 Flow system setup.

4.3 Catalyst characterization

X-ray diffraction (XRD), temperature programmed reduction (H_2-TPR), surface area analysis (SAA), thermal gravimetric analysis (TGA), in-situ FTIR, scanning electron microscope (SEM), inductively coupled plasma optical emission spectrometry (ICP-OES), scanning electron microscopy coupled to energy dispersive spectroscopy (SEM-EDS) and transmission electron microscopy (TEM) were conducted to characterize and determine properties of the catalyst. TPR was conducted on the fresh and spent catalyst using a catalyst characterization instrument (AMI-300Lite) under pure hydrogen from 100 °C to 800 °C with a ramping rate of 10 °C /min. XRD patterns were taken in a powder diffractometer D8 Discover (Bruker) for fresh and spent catalysts. To determine the size of crystallites the Scherrer formula was used that was built in the application for the obtained data analysis, Eq.11

$$\langle L \rangle = \frac{K\lambda}{S\cos\theta_o} \qquad (11)$$

where λ is the radiation wavelength, B is the physical width of a reflection (in $2\theta_0$), θ_0 is the diffraction angle of a line maximum, and K is a constant close to unity (K $\approx$ 0.9, if the halfwidth of a peak is taken, and K $\approx$ 1 for the integral width).

Specific surface area was measured by the SSA (AMI-300Lite) with single-point BET method using nitrogen as an adsorption gas. Chemical composition was determined by ICP-OES (Prodigy SPEC, Leeman Labs Inc.). SEM and SEM-EDS were also carried in a Zeiss microscope at 20 kV to obtain elemental mapping and morphology of the catalyst. To investigate the degree of coking of the spent catalyst TGA was used that is connected in-Line with an FTIR analyzer (MultiGas™ 2030, MKS Instruments) referred as In-situ TGA-FTIR and a mass spectrometer (MS) (HPR-20, Hiden Analytical) to determine the concentration of CO_2, CO and O_2.

4.4 Catalyst performance evaluation

The catalytic performance was investigated at different temperatures (300-600 °C) and space velocities (10,000-200,000 mL/(g·h)) under the constant pressure 3 bars. CO_2 and H_2 inlet feed was controlled by two mass flow controllers and maintained at H_2:CO_2=4:1. Before the reaction, the reduction was carried by pure H_2 at 350 °C for 2 h. To obtain CO_2 conversion and selectivity to CO, GHSV lower than 60,000 mL/(g·h) was kept at the same temperature for 3 h until the concentration is stable, while GHSV higher than 60,000 mL/(g·h) was carried for 2 h until the concentration is stable.

The gas hourly space velocity (GHSV) was calculated by the following equation, Eq.12:

$$GHSV = Q_f \big/ W_C \tag{12}$$

where Q_f and W_C are the volumetric flow rate and the weight of the catalysts, respectively.

CO_2 conversion and CO selectivity were determined by Eq. 13 and Eq. 14, respectively:

$$X_{CO_2} = \frac{y_{CO} + y_{CH_4}}{y_{CO_2} + y_{CO} + y_{CH_4}} \tag{13}$$

$$S_{CO} = \frac{y_{CO}}{y_{CO} + y_{CH_4}} \tag{14}$$

where y_{CO_2}, y_{CH_4} and y_{CO} represents the mole fraction of CO_2, CH_4, and CO respectively on dry basis. X is the conversion and S is the selectivity.

Carbon balance is the number that is measured before the reaction gas entered the reactor and after the gas exited it in percent. This measurement is taken once the steady-state is reached for the each step. The forementioned step was held for 2-3 hours to ensure the data validation. Carbon balance is defined as the total rate of carbon fed to the reactor divided by the rate of carbon exiting the reactor, Eq.12 with the following expressions, Eqs.15-18:

$$CB = \left(y_{CO} + y_{CO_2} + y_{CH_4}\right)\left(1 + \alpha - f_1 - 4f_2\right) \tag{15}$$

$$\alpha = \frac{F_{H_{2,f}}}{F_{CO_{2,f}}} \tag{16}$$

$$f_1 = \frac{y_{CO}}{y_{CO_2} + y_{CO} + y_{CH_4}} \equiv \frac{F_{CO,out}}{F_{C,out}} = \frac{F_{CO,out}}{F_{CO_2,f}} \tag{17}$$

$$f_2 = \frac{y_{CH_4}}{y_{CO_2} + y_{CO} + y_{CH_4}} \equiv \frac{F_{CH_4,out}}{F_{C,out}} = \frac{F_{CH_4,out}}{F_{CO_2,f}} \tag{18}$$

where α is the ratio of H_2/CO_2 in the feed, f_1 and f_2 are the conversion to CO and CH_4 respectively, $F_{C,out}$ is the outlet molar flow rate.

Here the carbon balance summarized from the above equations, Eqs. 15-18 in combination with Eq. 19 determine the total outlet molar flow rate, Eq.20:

$$CB = \frac{(y_{CO} + y_{CO_2} + y_{CH_4})F_{t,out}}{F_{CO_2,f}} \tag{19}$$

$$F_{t,out} = F_{CO_2,f} + F_{H_2,f} - F_{CO_2,out} - 4F_{CH_4,out} \tag{20}$$

Carbon balance (CB) was measured and recorded continuously in all experiments by using LabVIEW. The carbon balance was maintained ranging from 100%±15%. A variety of reasons could cause deviation of carbon balance from unity, such as carbonaceous deposition over the catalyst, evaporation of volatile products, and the systematic error of IR analysis.

For the stability test, a 1/4" U-shaped quartz reactor was connected to stainless-steel flexible tubing and conducted to the flow system (Fig. 2). The pelletized catalyst of 400 mg (350-450 μm particle size) was fixed inside the reactor between quartz wool then the quartz reactor was placed inside the furnace with quartz wool insulation. The stability test was performed at 600 °C with the changing GHSV (60,000; 100,000 and 200,000 mL/(g h)) under the constant 1 bar with $H_2:CO_2=4:1$.

CO generation rate per catalyst weight (r) and per active phase weight (R) was calculated by Eqs (21, 22) (W_s is catalyst weight and is L_{Cu} is Cu loading in %):

$$r_{CO} = \frac{F_{CO_{2,f}} X_{CO_2} S_{CO}}{W_c} \tag{21}$$

$$R_{CO} = 100 \frac{r_{CO}}{L_{Cu}} \tag{22}$$

Turnover frequency (TOF) was calculated from Eq. 23, where M_{Cu} is atomic weight and D is the metal dispersion obtained by CO_2 TPD, as calculated by Eq. 24:

$$TOF = \frac{M_{Cu} \times R_{CO}}{D} \tag{23}$$

$$D = \frac{M_{Cu} \times U}{100 \times 1 \times L_{Cu}} \tag{24}$$

U in Eq.24 is the uptake from chemically absorbed CO_2 in mole per gram catalyst and 1 is the stoichiometric factor for CO_2 desorption. The following particle size (in nm) was calculated by Eq.25:

$$d_i = \frac{6 \times 10^9 \times M_{Cu} \times \rho_{site}}{\rho_{Cu} \times N_A \times D} \tag{25}$$

The Cu site density (ρ_{site}) is 14.6 Cu atoms per nm² which is equivalent to the 0.00154 nm² site area [44], [45].

4.5 In-situ FTIR study

An FTIR spectrometer (Thermo Scientific™ Nicolet™ iS™5) with an IR cell placed inside and the catalyst characterization instrument (AMI-300Lite) were used to get in-situ FTIR spectra in order to investigate the reaction mechanism of the catalyst surface. The powder samples are used without prior preparation in an infrared spectroscopy sampling technique. Then the sample is

put in the sample cup and the data analyzed on the bulk sample. The in-situ FTIR spectra were studied at 300 °C. Inlet and outlet flows were connected to the instrument and gone through the IR cell. A controller is connected to a bed thermocouple to control the temperature. The sample was reduced in H_2 (10% H_2/Ar) at 300 °C for 1 hour followed by argon flushing and dehydrating before introducing reaction gases (5% CO_2/He, 30 mL/min). Then the background spectra were taken at the same temperature under argon 30 mL/min.

4.6 Reverse water gas shift equilibrium

The maximum conversion is limited by equilibrium and it is a function of temperature, because the reverse water gas shift reaction, Eq. 1, is reversible. The equilibrium conversion can be calculated analytically. Total conversion and H_2/CO_2 feed ratios are related to the equilibrium conversion, Eqs.13-14 respectively, for each species at equilibrium the following expression are derived assuming that CH_4 formation equals zero, Eqs. 26-31:

$$X = \frac{n_{CO_2,f} - n_{CO_2,eq}}{n_{CO_2,f}}$$

(26)

$$\alpha = \frac{n_{H_2,f}}{n_{CO_2,f}}$$
(27)

$$\phi_{CO_2} = (1 - X)$$
(28)

$$\phi_{H_2} = \alpha - X$$
(29)

$$\phi_{CO} = X$$
(30)

$$\phi_{H_2O} = X$$
(31)

48

where n_i- is a feed flow rate for the following gases, H_2 and CO_2.

To calculate equilibrium pressures the equations mentioned above can be used, Eqs.32-36.

$$P_i = y_i P = (\frac{\phi_i}{\sum \phi_j}) P \tag{32}$$

$$P_{CO_2} = \frac{1-X}{1+\alpha} P \tag{33}$$

$$P_{H_2} = \frac{\alpha - X}{1+\alpha} P \tag{34}$$

$$P_{H_2O} = \frac{X}{1+\alpha} P \tag{35}$$

$$P_{CO} = \frac{X}{1+\alpha} P \tag{36}$$

where y_i is a mole fraction and P_i pressure.

Then to calculate the RWGS equilibrium constant, Eq.37:

$$K_{RWGS} = A_{RWGS} \exp(-\frac{-\Delta H_{RWGS}}{R_g T}) = \frac{P_{CO} P_{H_2O}}{P_{CO_2} P_{H_2}} = \frac{X^2}{(1-X)(\alpha - X)} \tag{37}$$

Therefore, the equilibrium conversion depends on the temperature, H_2/CO_2 feed ratio, but it will not depend on pressure, and there is no change in number of moles, Eq.1.

Chapter 5: Kinetic parameter estimation

5.1 MATLAB formulation

Parameter estimation was conducted using the minimization sum of weighted residual squares of the CO_2 and CO concentrations by the Trust-Region Reflective Algorithm [46]. The equation is based on the mass balance due to the constant temperature for each point of the reaction. While the experimental values were obtained from the IR analyzer, the simulated mole fraction was calculated by integrating the set of ordinary differential equation (fourth-order Runge-Kutta) described by Eq.38 (MATLAB ode15s) which represents time evolution of all species of the RWGS reaction, i.e. CO_2, H_2, CO, and H_2O, Eq. 38:

$$\varepsilon \frac{dc_i}{dt} = -\frac{Q_f(c_i - c_{if})}{V_r} + (1-\varepsilon)\rho_{cat}\alpha_i R_j \qquad (38)$$

This equation was obtained in the dimensionless form in Appendix A. The parameter estimation code from MATLAB is shown in Appendix B.

The MATLAB code contains three main functions such as: SSE_lsqnonlin_mod_WTR, SSE_CSTR_ALL_mod_newresults, and CSTResti. Each function has its own purpose. CSTResti function contains the kinetic, adsorption constants, reaction rate and mole fraction equations in dimensionless form. This function is used to calculate mole fraction of all species that participate in the reaction. SSE_CSTR_ALL_mod_newresults and SSE_lsqnonlin_mod_WTR are SSE functions. The SSE is a network performance function that was used for the measurement performance according to the sum squared errors. SSE_CSTR_ALL_mod_newresults determines the error between the simulation results and experimental data of mole fraction of species. While SSE_lsqnonlin_mod_WTR uses lsqnonlin function that nonlinear data-fitting problems. This

function starts at the point X (the initial values of activation energy, preexponential factor of the reaction, enthalpy change of adsorption and preexponential factor of adsorption constants of CO, CO_2 and H_2O) and finds a minimum to the sum of squares of the functions described in function, including the set of lower and upper bounds on the design variables.

This parameter estimation was conducted in MATLAB to determine eight parameters such as: activation energy, preexponential factor of the reaction, enthalpy change of adsorption and preexponential factor of adsorption constants of CO, CO_2 and H_2O were estimated. The experimental data of conversion, mole fractions and carbon balance were compared to the simulation one as well as the following plots were made to see the difference. Two T-tests (from 300 ℃ to 600 ℃ with the step of 50 ℃) at 10,000 mL/(g h) and 60,000 ml/(g h), and GHSV test (10,000 mL/(g h); 20,000 mL/(g h); 60,000 mL/(g h); 100,000 mL/(g h); 150,000 mL/(g h); 200,000 mL/(g h) at 450 ℃ were used for this estimation. The obtained model accurately predicts the experimentally measures mole fractions of RWGS species over a variety of operating conditions. The parameters were estimated with DEN coefficient that depends on adsorption constants of species and with DEN coefficient equals one to determine the importance of adsorption constants using the plots. The initial guesses were obtained from the paper while the fitting was achieved using the parameter estimation model.

5.2 Kinetic parameter estimation

An experimental data obtained from the Cu/Al_2O_3 catalyst can be used to predict catalytic performance under various operating conditions and evaluate practical use. It was assumed that the RWGS reaction over Cu/Al_2O_3 catalyst follows the mechanism that was described in the paper of Xu and Froment [47], the rate equation can be written using the Langmuir-Hinshelwood-Hougen-Watson (LHHW) approach. Assuming that there is no CH_4 formation observed and

51

furthermore, the experiment confirmed no CH_4 formation. The following RWGS mechanism is suggested (L is an active site), Eqs. 39-42:

$$CO_2 + L \rightleftarrows CO_2 - L \tag{39}$$

$$CO_2 - L + L \rightleftarrows CO - L + O - L \tag{40}$$

$$O - L + H_2 \rightleftarrows H_2O + L \tag{41}$$

$$CO - L \rightleftarrows CO + L \tag{42}$$

The Langmuir-Hinshelwood formulation can represent all reactions, including the surface reaction by elementary reversible reactions, where CO_2 dissociation is a limiting step, therefore the reaction can be written as, Eq. 43:

$$r = k_f \, [CO_2 - L][L] - k_b[CO - L][O - L] \tag{43}$$

Partial pressures and the corresponding adsorption/desorption equilibrium constants express the concentration of the adsorbed species, Eqs.44-45. Therefore, the final equation was taken from Eq.43 and reorganized, DEN and R (reaction rate) are written as, Eqs.46-47:

$$y_i = \frac{c_i}{c_t} = \frac{c_i}{\rho_g} \tag{44}$$

$$c_t = \rho_g = \frac{P_T}{R_g T} \tag{45}$$

$$R = k_{RWGS} P_t (y_{CO_2} - \frac{y_{CO} y_{H_2O}}{K_{RWGS} y_{H_2}}) \frac{1}{DEN^2} \tag{46}$$

$$DEN = 1 + P_t \cdot K_{CO} y_{CO} + P_t \cdot K_{CO_2} y_{CO_2} + \frac{K_{H_2O} y_{H_2O}}{y_{H_2}} \tag{47}$$

The reaction rate and adsorption constants can be found, Eq.48:

$$K_i = B_i \exp(-\frac{\Delta H_i}{R_g T})$$ (48)

To run the model in MATLAB the initial guesses must be made. Equilibrium constants and initial guesses for preexponential factor of adsorption constants and enthalpy change of adsorption, CO, CO_2 and H_2O were adopted from Xu and Froment [47] and Elnashaie et al. [48], and Michael et al. [49] shown in Table 2.

Table 3 Equilibrium constants and initial guesses for preexponential factor of adsorption constants and enthalpy change of adsorption.

Symbol	Value	Unit
ΔH_{CO}	-70.65	kJ/mol
ΔH_{H_2O}	88.68	kJ/mol
B_{CO}	8.25×10^{-5}	bar^{-1}
B_{H_2O}	1.77×10^{5}	bar^{-1}
ΔH_{eq}	36.5816	kJ/mol
B_{eq}	56.5995	bar^{-1}
ΔH_{CO_2}	35.0	kJ/mol
B_{CO_2}	97.9	bar^{-1}

Initial guesses for the activation energy (Ea) and the preexponential factor of rate coefficient (A_{RWGS}), obtained using the following equations, reaction rate equation, Eq.49, where CO_2 consumed, Eq.50 and CO_2 flow rate, Eq. 51:

$$R = \frac{CO_{2consumed}}{Wc \cdot 60} \cdot 1000$$ (49)

$$CO_{2consumed} = F_{CO_{2,fed}} \cdot X$$ (50)

$$F_{CO_{2,fed}} = F_t \cdot \alpha_{CO_2} \cdot \frac{P}{R_g T} \tag{51}$$

The rate coefficient of RWGS reaction was used to obtain A_{RWGS} and Ea from the Arrhenius plot, Eqs.52-53, where it was assumed that DEN =1, RWGS equilibrium constant was calculated using Eq.46:

$$k_{RWGS} = \frac{R \cdot DEN^2}{P_{CO_2} - \frac{P_{H_2O} \cdot P_{CO}}{K_{RWGS} \cdot P_{H_2}}} \tag{52}$$

$$\ln(k_{RWGS}) = \ln\left(A_{RWGS}\right) - \frac{Ea}{R_g} \frac{1}{T} \tag{53}$$

Chapter 6: Results and discussion

6.1 Characterization results

$Cu/\gamma-Al_2O_3$ batches were synthesized by the RME method described in Section 4.1. SSA for the as-prepared fresh and spent catalyst was measured using the BET experiment, Cu dispersion was obtained by CO_2-TPD, crystallite size was obtained by XRD, and chemical composition was measured by ICP-OES for as-prepared catalyst (Table 3). The highest SSA was obtained at 369.69 $m^2 \ g_{cat}^{-1}$, while the average number with standard deviation was reported at 328.3$\pm$32.1 $m^2 \ g_{cat}^{-1}$. The variations in SSA can be related to the preparation steps. The obtained surface area is much higher as compared to the similar study of Bansode et al. [50], where 18 wt% $Cu/\gamma-Al_2O_3$ prepared by wet impregnation had SSA of 184 $m^2 \ g_{cat}^{-1}$. Therefore, in the study presented in this thesis, more active sites were exposed to the reaction. However, the surface area of spent catalyst was highly reduced after the reaction (169.5 m^2/g). Compared to as-prepared catalyst, significant reduction in the average pore volume of $Cu/\gamma-Al_2O_3$ indicates possible sintering at high temperatures [51]. When the catalyst is exposed to the higher temperature the crystallite size increases and the surface area decreases [52].

Although the targeted Cu content was 25 wt%, the obtained values were measured at 18 wt% (Table 3). Cu loss can occur during the RME preparation steps, particularly due to washout during the centrifugation. For as prepared catalyst, the catalyst is well-dispersed and the particle size is relatively small (6.5 nm), consistently with the RME preparation technique that typically provides particle size of 5-10 nm [53]. To evaluate the Cu dispersion of the catalyst the CO_2 TPD was performed, where it can be seen that as-prepared catalyst has quite high 15.7 % dispersion that is quite consistent with the diameter of particles. After the temperature test, it can be seen that the

dispersion decreased, indicating the agglomeration of Cu particles which is also a reason for the decrease in SSA of spent catalyst.

The CO_2-TPD results of the as-prepared, spent catalyst are shown in Table 3 with corresponding values of dispersion, particle diameter and TOF as calculated in Section 4.4. TOF provides insights on the intrinsic kinetic activity is the same after eliminating internal and external diffusion. TOF for this reaction with Cu/Al_2O_3 was 31 s^{-1} based on a fresh catalytic value and 9 s^{-1} for the spent one, these numbers are favourable for the industrial use [54].

Table 4 Cu/γ-Al_2O_3 composition, crystallite size, diameter, TOF, Cu dispersion and specific surface area.

Cu, wt%	SSA, m²/g		Cu dispersion,%		d, nm		TOF, s^{-1}		Crystallite size, nm		
	As-prepared	Spent	As-prepared	Spent	As-prepared	Spent	As-prepared	Spent	Spent		
									Cu	Cu₂O	γ-Al₂O₃
18.0±0.3	328.3±32.1	169.5±19.9	15.7	4.6	6.5	21.9	31	9	9.35	6.58	8.34

XRD patterns for the as-prepared catalyst Cu/γ-Al_2O_3 (calcined at 400 °C) and spent Cu/γ-Al_2O_3 alongside with spent Al_2O_3 synthesized by RME (after the temperature test) are shown in Figure 23.
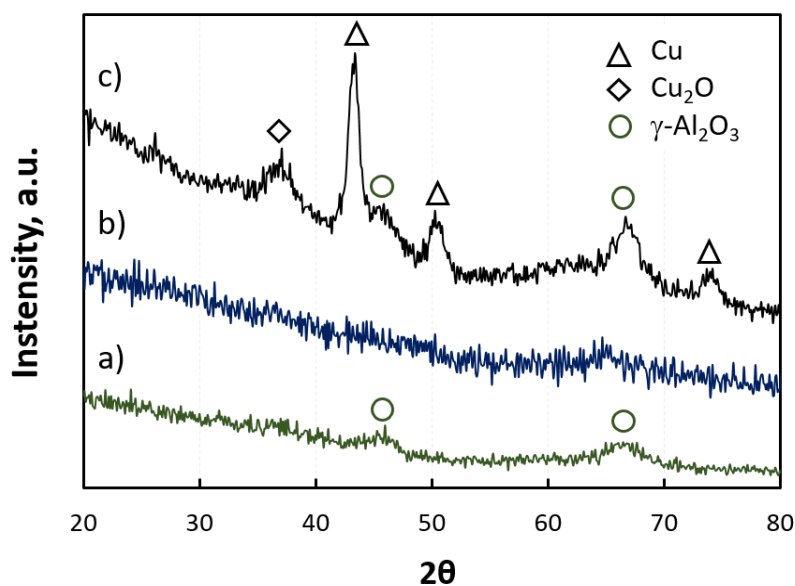
Fig. 23 XRD patterns of a) spent γ-Al$_2$O$_3$, b) as prepared Cu/γ-Al$_2$O$_3$, and c) spent Cu/γ-Al$_2$O$_3$. Peaks associated with γ-Al$_2$O$_3$, Cu$_2$O, and Cu are shown by circles, diamonds, and triangles, respectively.

Clear peaks for as-prepared fresh Cu/γ-Al$_2$O$_3$ catalyst were not observed due to the amorphous nature of the γ-alumina support. For the spent Cu/γ-Al$_2$O$_3$ peaks were identified at 36.5° for Cu$_2$O; at 43.7°, 50.5° and 74.0° for Cu and at 46.3° and 67° for γ-Al$_2$O$_3$. Similar XRD patterns, except for Cu$_2$O, were observed by Bansode et al. [50], where metallic copper and Al$_2$O$_3$ were indicated after the reaction. The XRD pattern showed broad diffraction peaks due to poorly microcrystalline γ-alumina which was also reported by López-Suárez, Bueno-López [55]. The absence of CuO diffraction peaks in catalysts indicated that the formation of highly dispersed copper species on the alumina surface.

The XRD pattern demonstrated full reduction of CuO to Cu after the reaction [50]. It could be the sign of sintering during the reaction and activation of the catalyst. This is a phenomenon which was also reported by Bansode, Tidona [50]. Similarly, peaks 46.3° and 67° were identified

for the spent γ-Al$_2$O$_3$ [50]. The peaks were detected in a built-in tool using Bruker XRD Eva software. Furthermore, the crystallite sizes were calculated by built-in Scherrer equation tool in Bruker XRD Eva software. The average values of the multiple peaks were used to calculate crystallite size for both Cu and γ-Al$_2$O$_3$ (Table 3). The agglomeration of particles could be related to the increase in the crystallite size which also explains the decrement of SSA values.

Figure 24 presents scanning electron microscopy (SEM) micrographs for as-prepared Cu/γ-Al$_2$O$_3$ catalyst. This highly porous structure with detectable nanometric features was coherent with the high SSA of the samples (369.69 m^2 g$_{cat}$$^{-1}$). Moreover, the cloudy growth was accounted for copper formations on the γ-Al$_2$O$_3$ support that occupies most of the sample volume. Similar patterns were obtained in the study of Bayat et al. [56] the incorporation of metal oxide into γ-Al$_2$O$_3$ support decreases the porosity of the catalyst.

Elemental mapping was conducted by energy dispersive spectroscopy (SEM-EDS) to further investigate the dispersion and elemental composition. Figure 25 confirms highly dispersed copper in the sample. High dispersion was previously confirmed by dispersion for as-prepared catalyst. Particularly, the dispersion of Al, Cu and O can be observed in colors.
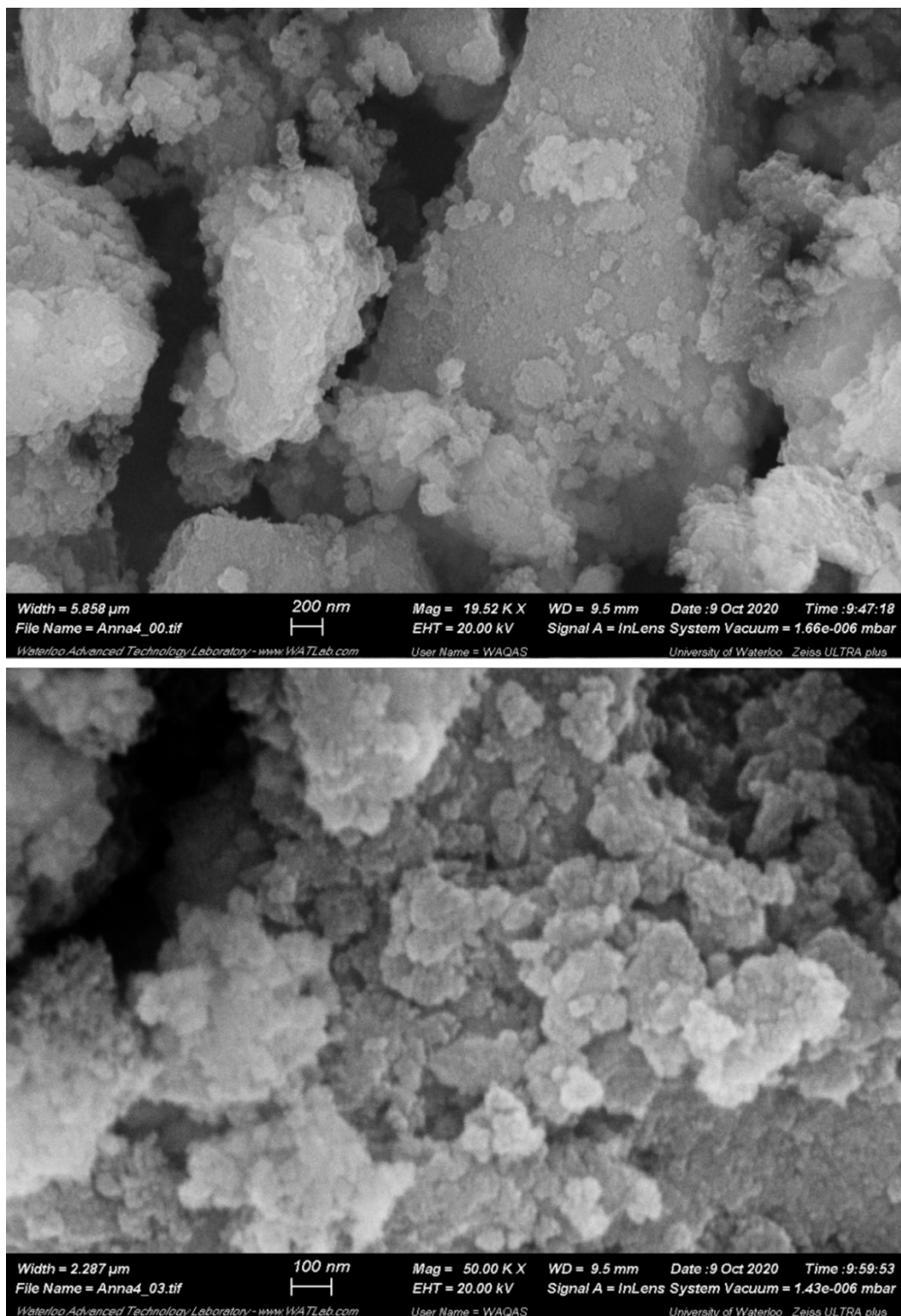
Fig. 24 SEM micrographs of as-prepared Cu/γ-Al$_2$O$_3$ catalyst. Scale bars are 100 nm, and 200 nm
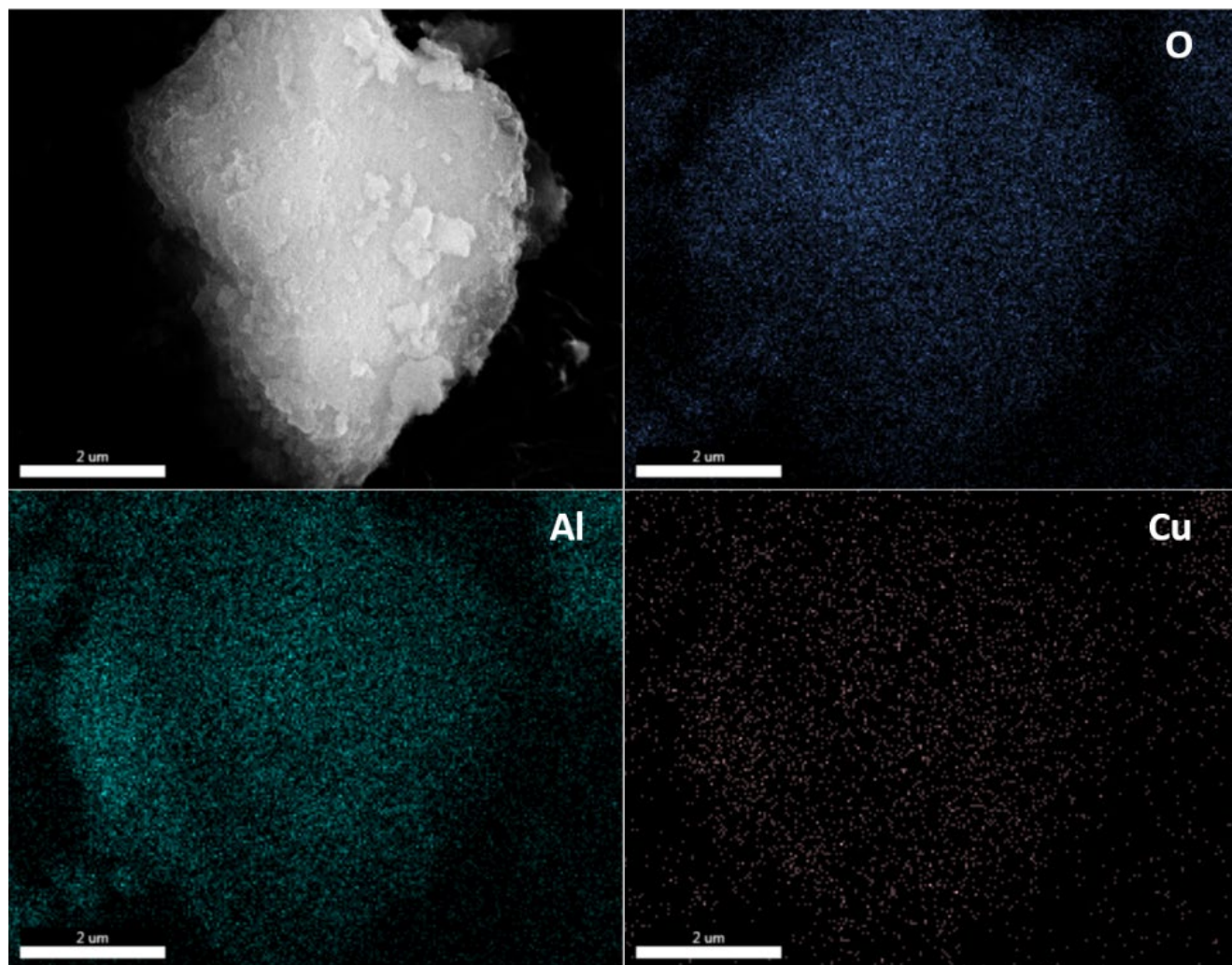
Fig. 25 SEM-EDS mapping of as-prepared Cu/γ-Al$_2$O$_3$ catalyst (Scale bars are 2 μm).

Figure 26(a) shows the H$_2$ consumption for as-prepared different batches of Cu/γ-Al$_2$O$_3$ catalyst after the temperature tests. The TPR allows to study the reducibility of the as-prepared catalysts in order to choose the best reduction temperature for the reaction. The experimental peaks were reported at 252.5, 274.9 and 280 °C that attributes to the temperature range of above 260 °C that also shows the reduction of the bulk CuO on alumina. Nevertheless, for the temperature range 200-250 °C, the reduction is attributed to highly-dispersed CuO [57]. Luo, Fang [58] reported the similar results within the range of 230–255 °C where peaks were contributed to the reduction of

highly-dispersed CuO species, while for temperature in the region of 275-300 °C, the peaks were attributed to the reduction of bulk CuO species.
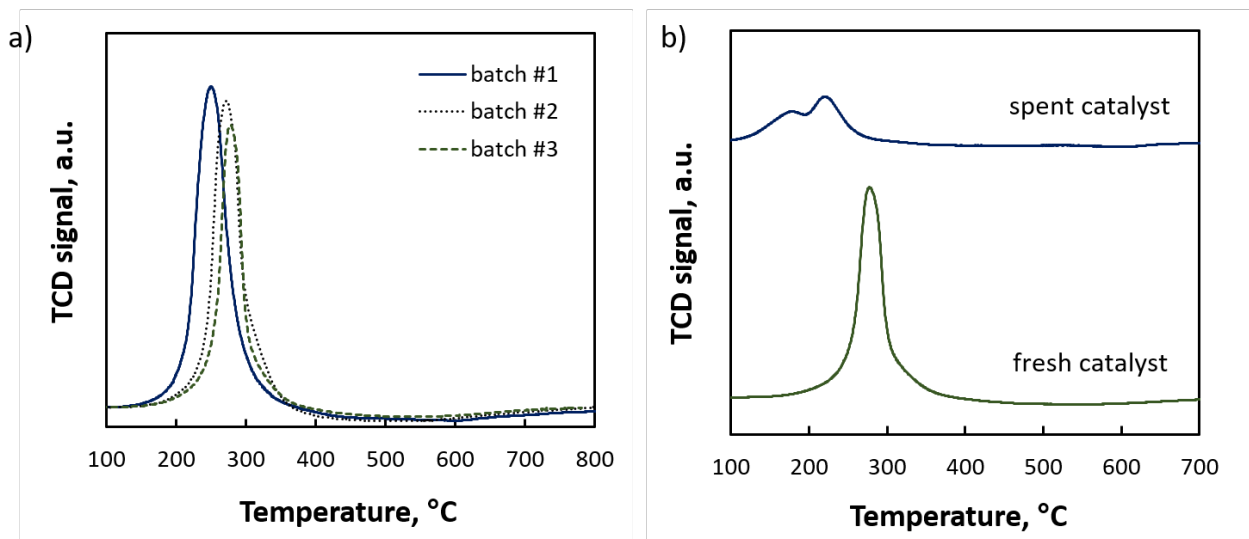
Fig. 26 Temperature programmed reduction profiles obtained for a) different batches of the as-prepared Cu/γ-Al$_2$O$_3$ catalyst after calcination and b) the comparison Cu/γ-Al$_2$O$_3$ catalyst as-prepared after calcination and spent.

The negligible variation of TCD signal (standard deviation 12 °C) was acceptable for the batches as the performance did not vary significantly. This CO$_2$ conversion deviation can be seen in the temperature test by error bars (Figure 29). This small shift of the peaks can be attributed to the interaction between the copper and alumina support during the synthesis. The reduction behavior of the fresh and spent catalyst (batch #1) was investigated using the H$_2$-TPR technique (Figure 26(b)). The TPR allows to study the reducibility of the catalysts. The as-prepared copper oxide supported on alumina nanoparticles (Cu/γ-Al$_2$O$_3$) exhibited only one reduction peak with high intensity at ca. 280 °C which was assigned to the reduction of bulk CuO. After the temperature test, the peaks were shifted to the left for the spent catalyst as well as the magnitude of the spent profile is much lower as for as-prepared one.

The redox properties of CuO can be affected by the interaction with alumina and small CuO clusters and/or isolated Cu^{2+} ions are reduced at lower temperatures than larger CuO crystallites [55]. Kim, Rodriguez [59] demonstrated that under a normal supply of hydrogen, CuO reduces directly to metallic Cu without formation of an intermediate or suboxide (i.e., no Cu_4O_3 or Cu_2O). The spent catalyst peaks were obtained at 185 °C and 223.5 °C. These peaks belong to reduction of CuO species [60]. The presence of the two peaks and their small shift can be hypothetically attributed to the interaction of copper and alumina support after activity test. The catalyst still remains active after the first temperature test.
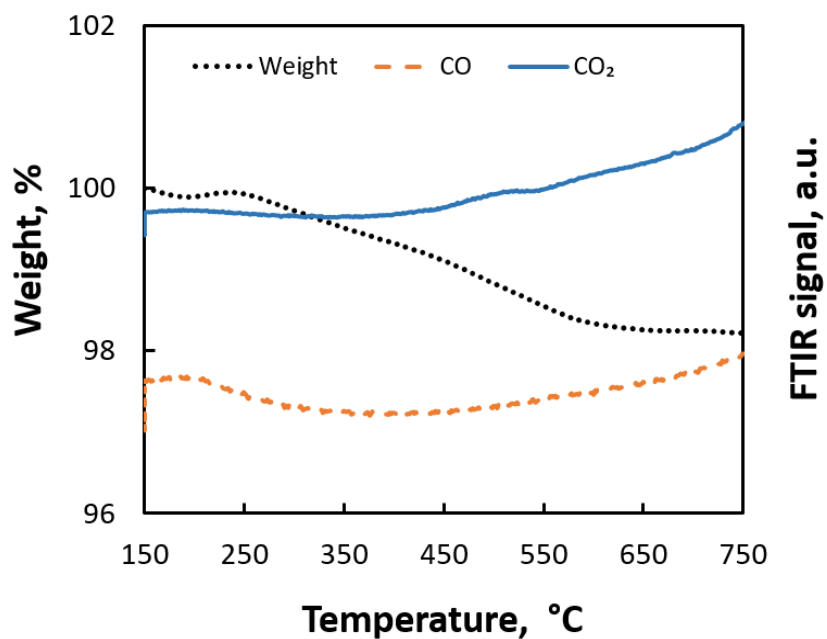
Fig. 27 TGA-FTIR analysis of spent Cu/γ-Al$_2$O$_3$ catalyst after the stability test. Evolution of CO, NO, CO$_2$ and SO$_2$ concentrations are shown in the FTIR signals. Temperature ramping rate was 10 °/min for T ≤ 150 °C and 2 °/min for T = 150–750 °C. Air flow rate was 40 ml/min. The stability test conditions: 1 bar, T=600 °C, H$_2$:CO$_2$=4:1 by ascending space velocity from 10,000 to 200,000 mL/(g h).

TGA-FTIR study was conducted to investigate the thermo-gravimetric properties and the extent of coking of the spent catalyst after the stability test in a quartz tube (Figure 27). For T = 150–750 °C the initial weight loss of Cu/Al_2O_3 can be attributed to the loss of water molecules trapped on the surface that around 2%. The sample gained almost 1% of weight due to the loss of Cu in the form of CuO at about 150–200 °C, this confirms the high stability of the Cu catalyst as well as retention of active Cu for higher hydrogenation activity [61]. Then above 550 °C the slight increase of CO_2 and CO are detected due to the oxidation of carbon on the surface of the sample that as well reduces the weight by around 2%. As a result, the overall decrease in the catalytic weight was about 2%, and there was no significant CO_2 signal observed that confirms the absence of a carbonaceous compounds over the spent catalyst. This result indicates that the RME-synthesized catalyst is resistant to coking.

6.2 Catalytic performance evaluation

Several tests were conducted under various operating conditions, specifically different space velocities and temperatures, to evaluate the catalytic performance of the catalyst. The main parameters for the fresh Cu/Al_2O_3 catalyst evaluation were CO_2 conversion and selectivity to CO generation (CO selectivity).
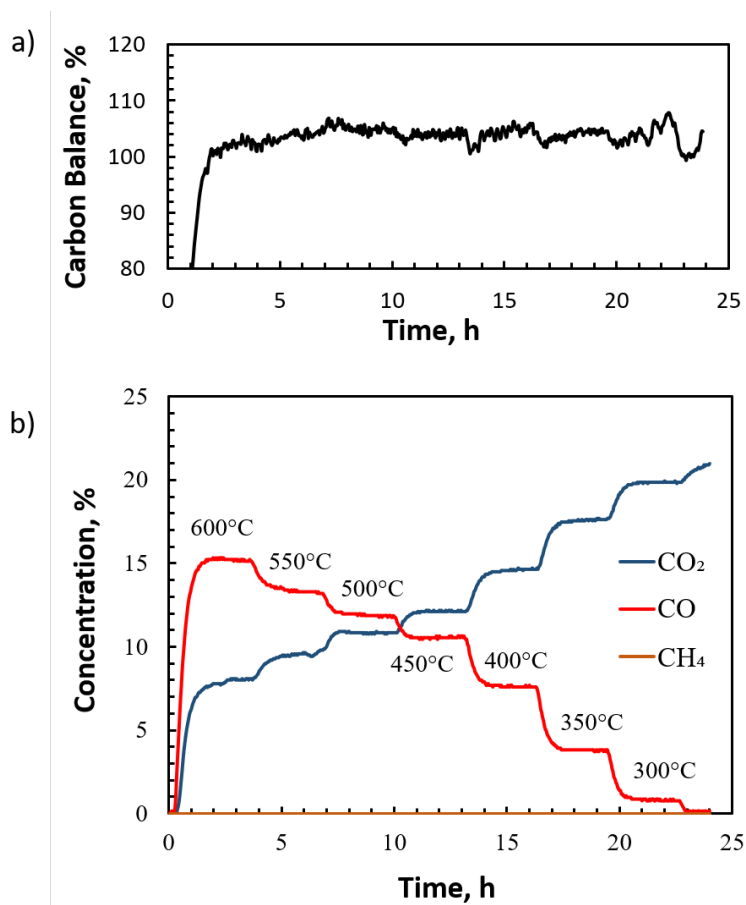
Fig. 28 a) Carbon balance as a function of time, and b) Concentration fields of CO, CO_2 and CH_4 evaluation of Cu/γ-Al$_2$O$_3$ catalyst as a function of time and temperature. Parameters: P = 3 bars, H_2:CO_2 = 4:1, and GHSV =10,000 mL/(g h).

Figure 28 represents the carbon balance and concentration fields during the reaction. The reaction was performed at various temperatures from 300 to 600 °C under constant GHSV 10,000 mL/(g h) and pressure 3 bar. At the beginning the reduction was conducting under the flow of H_2 so no carbon was observed. From the concentration fields (figure 28(b)), it can be seen that there was no CH_4 formation observed. The carbon balance was in a normal range for the reaction at 100±15%.
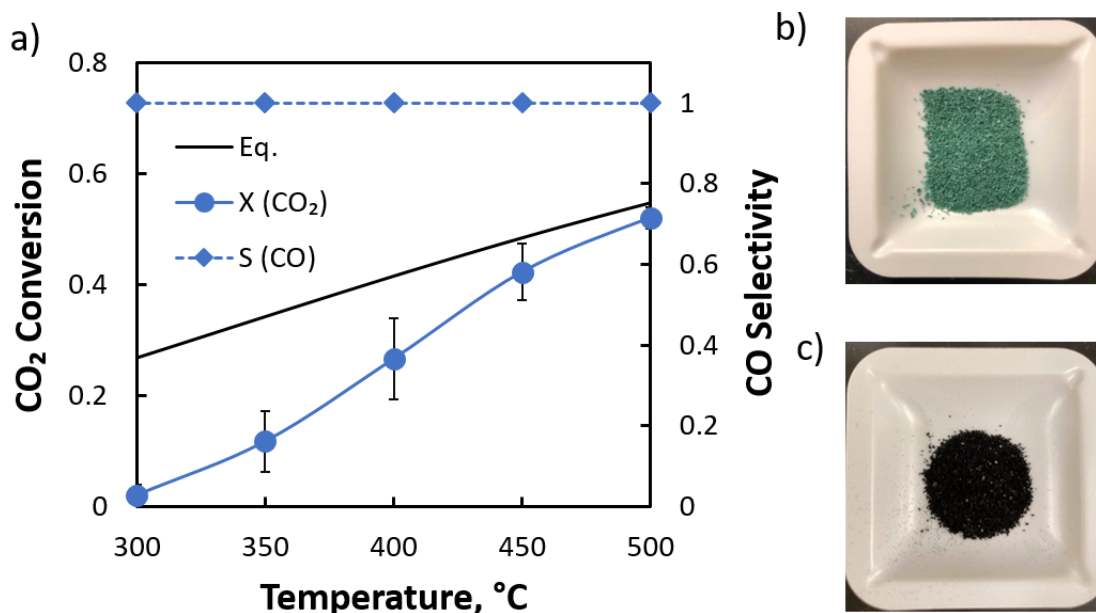
Fig. 29 a) Catalytic performance evaluation as a function of temperature for Cu/γ-Al$_2$O$_3$ catalyst prepared by RME method. Error bars show standard deviation for different batches. Equilibrium conversion and selectivity is shown by black line. Parameters: P =3 bar, H$_2$:CO$_2$ =4:1, GHSV =10,000 mL/(g h). b) as-prepared pelletized Cu/γ-Al$_2$O$_3$ after calcination, c) spent Cu/γ-Al$_2$O$_3$ after temperature test.

The catalytic performance of Cu/γ-Al$_2$O$_3$ catalyst prepared by RME method was tested for CO$_2$ conversion and CO selectivity as a function of reaction temperature. In general, as the temperature increased, the CO$_2$ conversion was of similar trend. Also, by rising the temperature, the values of CO$_2$ conversion approached closer to the equilibrium values. As shown in Figure 29(a), when temperature increased to 500 °C, the maximum CO$_2$ conversion of 52% was obtained which is relatively close to the equilibrium value of 55% in the same temperature. This could be ascribed to the endothermic nature of the RWGS reaction whereby the CO$_2$ conversion has direct relationship with the temperature. Furthermore, a complete selectivity to CO generation was

obtained at all temperatures as in the study of Chen et al. [62] for γ-Al$_2$O$_3$ supported catalyst at 500°C and 10,000 mL/(g h) the CO$_2$ conversion was around 50% while the selectivity to CO was about 60-55%. Therefore, the results of activity test in this study exhibit that Cu/γ-Al$_2$O$_3$ catalyst prepared by RME method is highly active and selective in RWGS at 500 °C and space velocity of 10,000 mL/(g h). Figure 29(b-c) shows calcined pelletized fresh and spent catalysts. Evidently, the natural color of Cu/γ-Al$_2$O$_3$ catalyst has changed significantly after undergoing reduction test. This phenomenon was attributed to reduction by H$_2$ with the feed rate 250 ccm at 350 °C for 2 hours prior to the reaction.
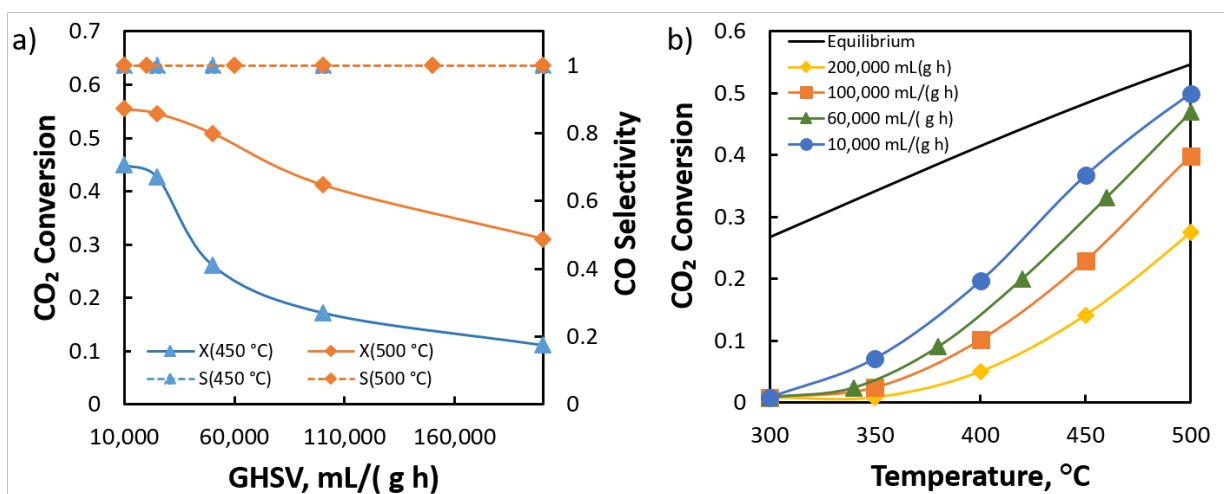
Fig. 30 a) CO$_2$ conversion of Cu/γ-Al$_2$O$_3$ catalyst as a function of temperature at different GHSV values (i.e., 10,000 to 200,000 mL/(g h)). Test conditions: P =3 bar, H$_2$:CO$_2$ =4:1. Equilibrium conversion is shown by black line, b) Catalytic performance evaluation of Cu/γ-Al$_2$O$_3$ catalyst as a function of space velocity. Parameters: P = 3 bars, H$_2$:CO$_2$ = 4:1, and T = 450 °C and 500 °C.

Figure 30(a) shows the CO$_2$ conversion versus reaction temperature for four different space velocities. An overall trend of increasing CO$_2$ conversion can be seen when space velocity is reduced. The results of GHSV test shows that the CO$_2$ conversion rates at 500 °C vary between

27% to 53% for space velocities of 10,000 mL/(g h) to 200,000 mL/(g h), respectively. Furthermore, the complete selectivity to CO was observed. That means, an increase in space velocity from 10,000 to 200,000 mL/(g h) caused a more notorious decreased in the catalytic activity at 500 °C. One of the biggest limitations of the RWGS is the low space velocity needed to achieve high performance [63]. Figure 30(b) considering the highest CO_2 conversion was observed at 500 °C and 450 °C, respectively, we herein investigated the variation of CO_2 conversion as a function of space velocities at fixed temperature and pressure (i.e. T=500 °C and 450 °C, P=3 bars). The results indicated that at both temperatures, CO_2 conversion drops as GHSV increases in figure 30(b). The similar GHSV test patterns were obtained from Zhuang et al. studies of RWGS reaction where with the increase in GHSV the conversion went down [51].

To investigate the stability, the catalyst was subjected to two heating-cooling cycles under the condition of 300-500 °C, 3 bars and a space velocity of 10,000 mL/(g h) using a stainless-steel reactor. Figure 31 displays CO_2 conversion over 18% Cu/Al for 41h. Four different tests of the catalyst were evaluated to ensure the consistent stability behavior and maximum CO selectivity of the catalyst over the time. As shown, all the tests showed similar trend with small changes in the same conditions of the reaction. The endothermic nature of the RWGS reaction has direct relationship with the rising CO_2 conversion with the temperature. The conversion at 500 °C for all the tests was stable at a constant rate of 51–53%, nearly equal to the equilibrium value (~55%). The high conversion rate along with thermal resistance as well as little to no deactivation at high temperatures for long periods indicate the capability of the Cu/γ-Al_2O_3 catalyst to be used in industrial applications.
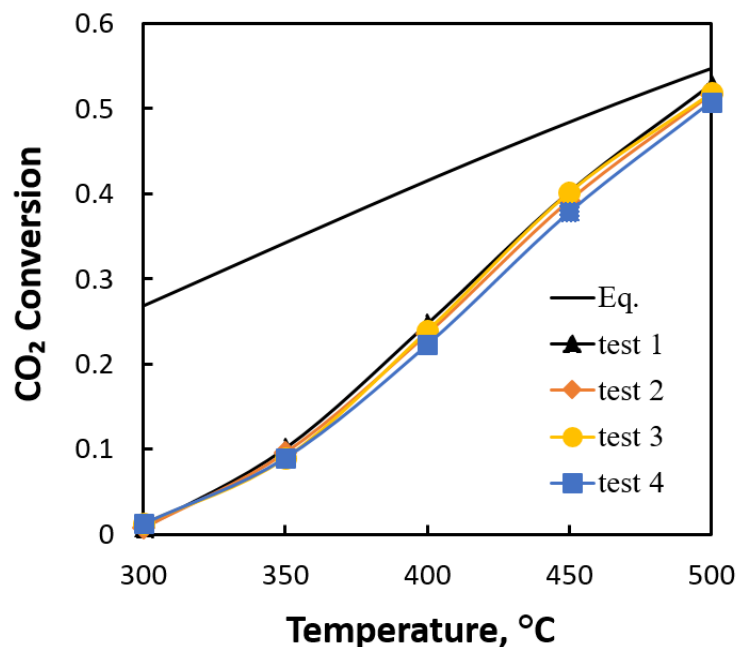
Fig. 31 CO_2 conversion as a function of temperature for Cu/γ-Al_2O_3 catalyst prepared by RME method. Cycling conditions: P=3 bar, H_2:CO_2=4:1, GHSV=10,000 mL/(g h), and descending temperatures from 500 °C to 300 °C followed by ascending temperatures from 300 °C to 500 °C with the step of 50 °C. The total time for the entire cycle is 41 hr. Equilibrium conversion is shown by the black line.

6.3 Stability evaluation

The stability test was conducted to evaluate the catalytic performance and resistance towards sintering, coking and deactivation within the long hours of reaction of the Cu/γ-Al_2O_3 (figure 32).

68
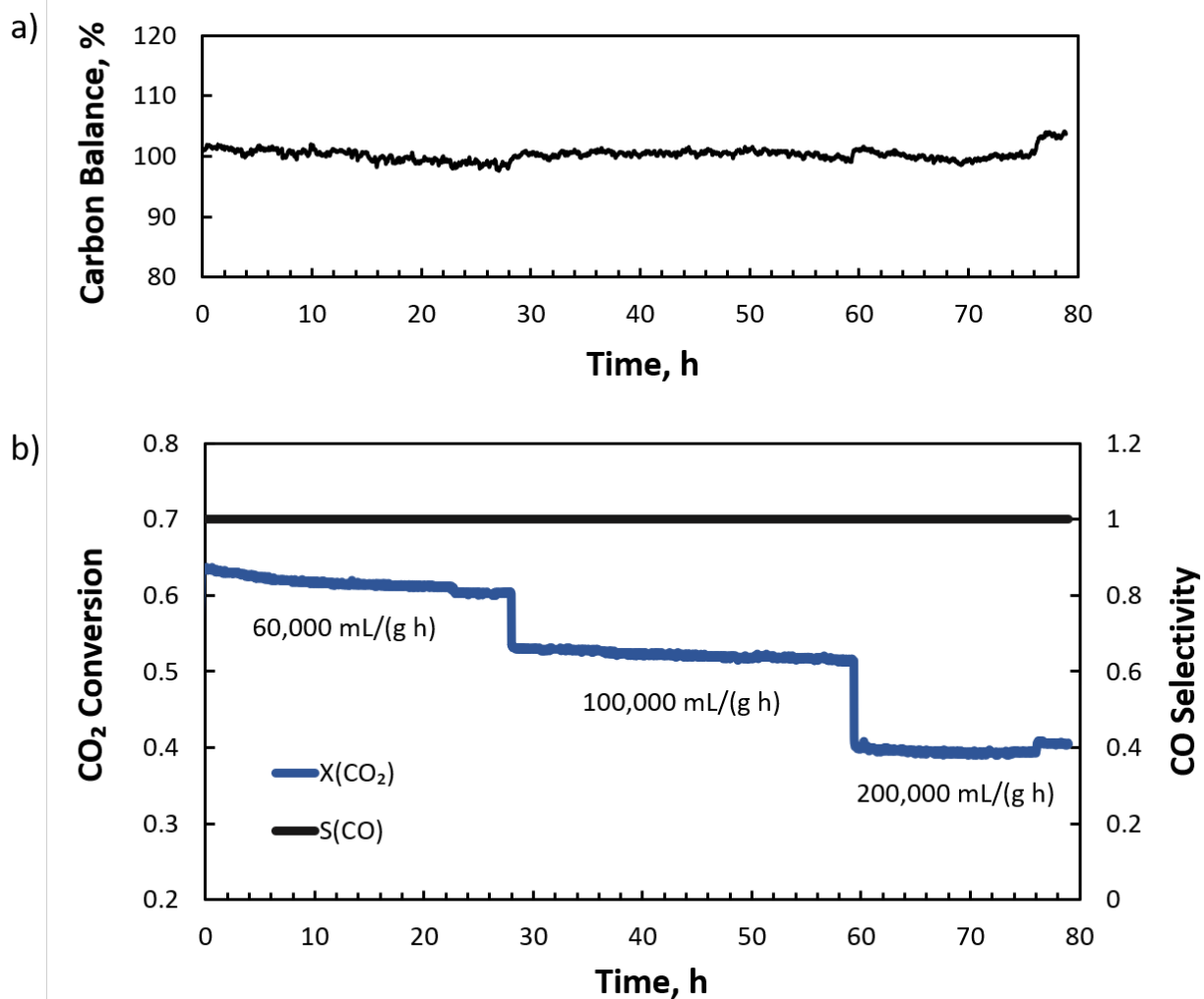
Fig. 32 a) Carbon balance as a function of time, and b) Stability test performance evaluation of Cu/γ-Al$_2$O$_3$ catalyst as a function of conversion, selectivity and time. Parameters: P = 1 bars, H$_2$:CO$_2$ = 4:1, and T = 600 °C.

The test was conducted in the quartz reactor. First, the H$_2$ reduction was conducted at 350 °C following by the temperature test from 300 to 600 °C with the 50 °C step. While during the process of reduction, the carbon balance is unstable since no carbon is fed to the system. Once the CO$_2$ was fed into the reactor, we can see that it was gradually stabilized. Carbon balance was

recorded throughout the experiment at 100±15% (figure 32(a)). It demonstrates that no carbon loss occurred during the test.

A variety of reasons could cause deviation of carbon balance from unity, such as carbonaceous deposition over the catalyst, evaporation of volatile products, and the systematic error of IR analysis [63]. The catalyst was subjected to a stability test under the following conditions of 600 °C, 1 bar and a space velocity a various space velocity from 60,000 to 200,000 mL/(g h) using a quartz reactor. Here the variation of GHSV can be observed. The lowest GHSV resulted in the highest conversion rate of 60% compared to the other GHSV values. The conversion decreased in 20 h only by 3% at 60,000 mL/(g h). Particular emphasis was given to the formation of CH_4 formation during the stability test. The results indicated that no CH_4 was formed as a result of which the complete selectivity to CO was observed at all stages. The overall catalytic performance showed a highly stable behaviour despite high temperature and GHSV variations. This supports that fact that reverse microemulsion synthesis method increases the catalytic activity and stability towards the RWGS reaction. Additionally, there were no clogging nor coking observed during this test which TGA-FTIR confirmed (figure 27).

6.4 Parameter estimation results

Parameter estimation was conducted for the purpose of the efficient utilization of experimental data for the estimation of constants appearing in modeling of the RWGS reaction. Therefore, the experimental data can provide insights on the catalytic performance and further simulation modeling. To estimate the parameters the set of lab experiments was conducted. The change in concentration of species was recorded by infrared analyzer as a function of space velocity and temperature (from 600 to 300 °C and 10,000 to 200,000 mL/(g_{cat}·h)). The obtained lab data was put into the MATLAB parameter estimation code to gain corrected constants

(equilibrium constants and initial guesses for pre-exponential factor of adsorption constants and enthalpy change of adsorption). Once the estimated parameters were obtained, the simulated mole fractions were calculated and plotted to compare experimental data. The MATLAB formulation and references for the kinetic parameter estimation can be found in Chapter 5 and Appendix A, B.

Firstly, the temperature test from 600 to 300 °C with the step of 50 °C was performed under the constant GHSV and pressure, 60,000 mL/(g$_{cat}$·h) and 3 bar, respectively. The experimental H$_2$/CO$_2$ ratio is 4:1. However, the best fitting was obtained with the H$_2$/CO$_2$ ratio of 3:1 and the results presented use this ratio (3:1). This deviation can be explained by the experimental error in the IR analyzer measurements of concentrations. Note that for the 4:1 H$_2$/CO$_2$ ratio, the CO$_2$ concentration is 20%, while for the 3:1 ratio, the CO$_2$ concentration is 25%. This difference corresponds to the experimental error in CO$_2$ concentration measurement of only 5% (out of the full scale of 100%). The initial guesses for activation energy and pre-exponential factor of the experimental data were taken from the Arrhenius plot (Fig. 33), using Eq. 53 to obtain these values (Section 5.2). The activation energy is 87.2 kJ/mol and the pre-exponential factor is 3.1E+05 mol/(bar s kg).

Fig. 33 Arrhenius plot for T-test at 60,000 mL/(g$_{cat}$·h)

The parameter estimation results for 60,000 mL/(g$_{cat}$·h) are presented in Table 4 where the initial guesses for the constants were obtained from the reference in the Section 5.1. The estimated constants were obtained from the parameter estimation in MATLAB. The first set of data shows the results obtained with DEN number (Eq. 47) that was calculated from adsorption constants of species and the second set shows the Ea and A$_{RWGS}$ with DEN=1.

Table 5 Parameter estimation results for 60,000 mL/(g$_{cat}$·h)

Set/Parameter	Ea, kJ/mol	A$_{RWGS}$, mol/(bar s kg)	B$_{CO}$, bar^{-1}	ΔH_{CO}, kJ/mol	B$_{H2O}$, bar^{-1}	ΔH_{H2O}, kJ/mol	B$_{CO2}$, bar^{-1}	ΔH_{CO2}, kJ/mol
Initial guess	87.2	3.1E+05	8.2E-05	-70.6	1.7E+05	88.6	97.9	35
1	86.8	3.7E+05	1.9E-05	-70.7	1.6E+05	91.8	97.4	33.1
2	119.1	2.5E+07	-	-	-	-	-	-

It can be seen that parameters are close to the obtained initial guesses for pre-exponential factor of adsorption constants and enthalpy change of adsorption. The first and second set of Ea and A$_{RWGS}$ should be close to each other. It can be seen that activation energy and pre-exponential factor change. In the first case, the adsorption limitations were accounted for and in the second case, the adsorption limitations were negligible (DEN=1). Therefore, further investigation and tests are needed to assess the results of adsorption limitations. For the first set, the mole fraction, conversion and carbon balance plots are shown in Fig. 34.

Fig. 34 A-Conversion of CO_2; B-Carbon Balance; C- Mole fraction profile. Experimental conditions: $H_2/CO_2=4$ in feed, P=3 bar, GHSV=60,000 mL/(gcat·h)

The experimental CO_2 conversion and experimental mole fractions of CO and CO_2 matches the simulation data well from 300-600 °C; after that the simulation line is lower. As for the carbon balance the simulation data is set to 100%, but during the experiment there are some variations which are acceptable. The second set was conducted using the same parameter estimation at 60,000 and disregarding adsorption limitations (DEN=1) (in Fig. 35). The conversion field at DEN=1 is steeper but the simulated mole fractions match closer the experimental data.

Fig. 35 A-Conversion of CO_2; B- Mole fraction profile. Experimental conditions: $H_2/CO_2 = 4$ in the feed, P = 3 bar, GHSV=60,000 mL/(gcat·h).

Furthermore, the temperature test from 600 to 300 °C with the step 50 °C was performed for the different batch of $Cu/\gamma\text{-}Al_2O_3$ under the constant GHSV and pressure that equal 10,000 mL/(g_{cat}·h) and 3 bar, respectively. The experimental H_2/CO_2 ratio is 4:1. However, the best fitting was obtained with the H_2/CO_2 ratio of 3:1 and the results presented use this ratio (3:1). This deviation can be explained by the experimental error in the IR analyzer measurements of concentrations. Note that for the 4:1 H_2/CO_2 ratio, the CO_2 concentration is 20%, while for the 3:1 ratio, the CO_2 concentration is 25%. This difference corresponds to the experimental error in CO_2 concentration measurement of only 5% (out of the full scale of 100%). The initial guesses for activation energy and pre-exponential factor of the experimental data were taken from the Arrhenius plot (Fig. 36), using Eq. 53 to obtain these values. And the adsorption constants were estimated in the parameter estimation in MATLAB. The activation energy is 117.5 kJ/mol, and pre-exponential factor is 4.9E+07 mol/(bar s kg).
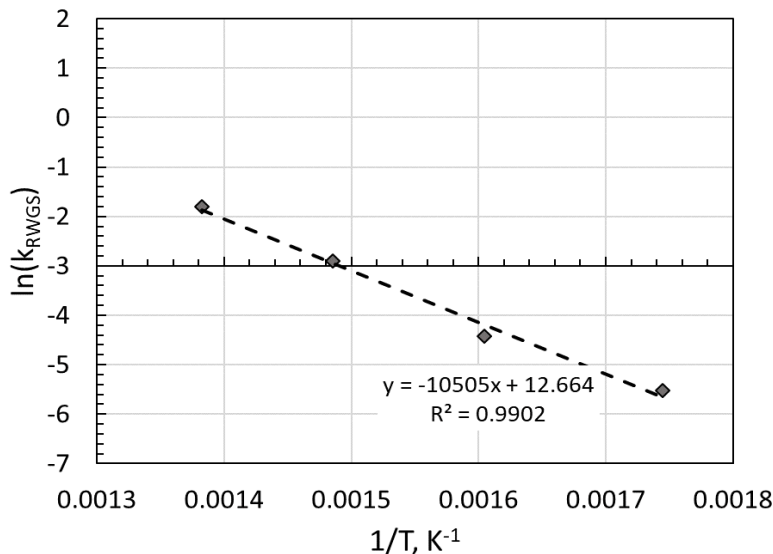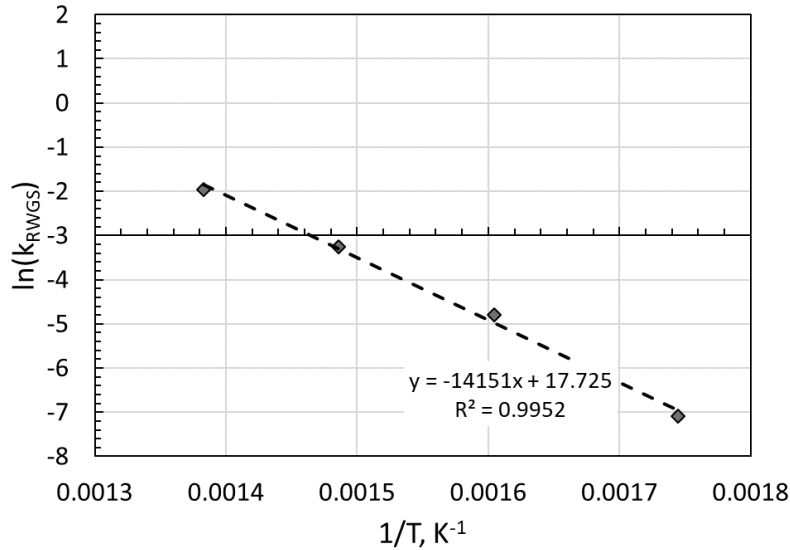
Fig. 36 Arrhenius plot for T-test at 10,000 mL/(g_{cat}·h)

The parameter estimation results for 10,000 mL/(g_{cat}·h) are presented in Table 5. The first set of data shows the results obtained with DEN number (Eq. 47) that was calculated from adsorption constant of species and the second set shows the Ea and A_{RWGS} with DEN=1. It can be seen that parameters are relatively close to the obtained initial guesses and that the first and second set of Ea and A_{RWGS} are close to each other.

Table 6 Parameter estimation results for 10,000 mL/(g_{cat}·h)

Set/Parameter	Ea, kJ/mol	A_{RWGS}, mol/(bar s kg)	B_{CO}, bar^{-1}	ΔH_{CO}, kJ/mol	B_{H2O}, bar^{-1}	ΔH_{H2O}, kJ/mol	B_{CO2}, bar^{-1}	ΔH_{CO2}, kJ/mol
Initial guess	117.5	4.9E+07	8.2E-05	-70.6	1.7E+05	88.6	97.9	35
1	115.6	5.0E+07	2.7E-05	-68.7	1.4E+05	95.7	80.8	35.7
2	117.9	2.2E+07	-	-	-	-	-	-

For the first set, the mole fraction, conversion and carbon balance plots are shown in Fig. 37. For the second set, the mole fraction and conversion of CO_2 are plotted in Fig. 38.
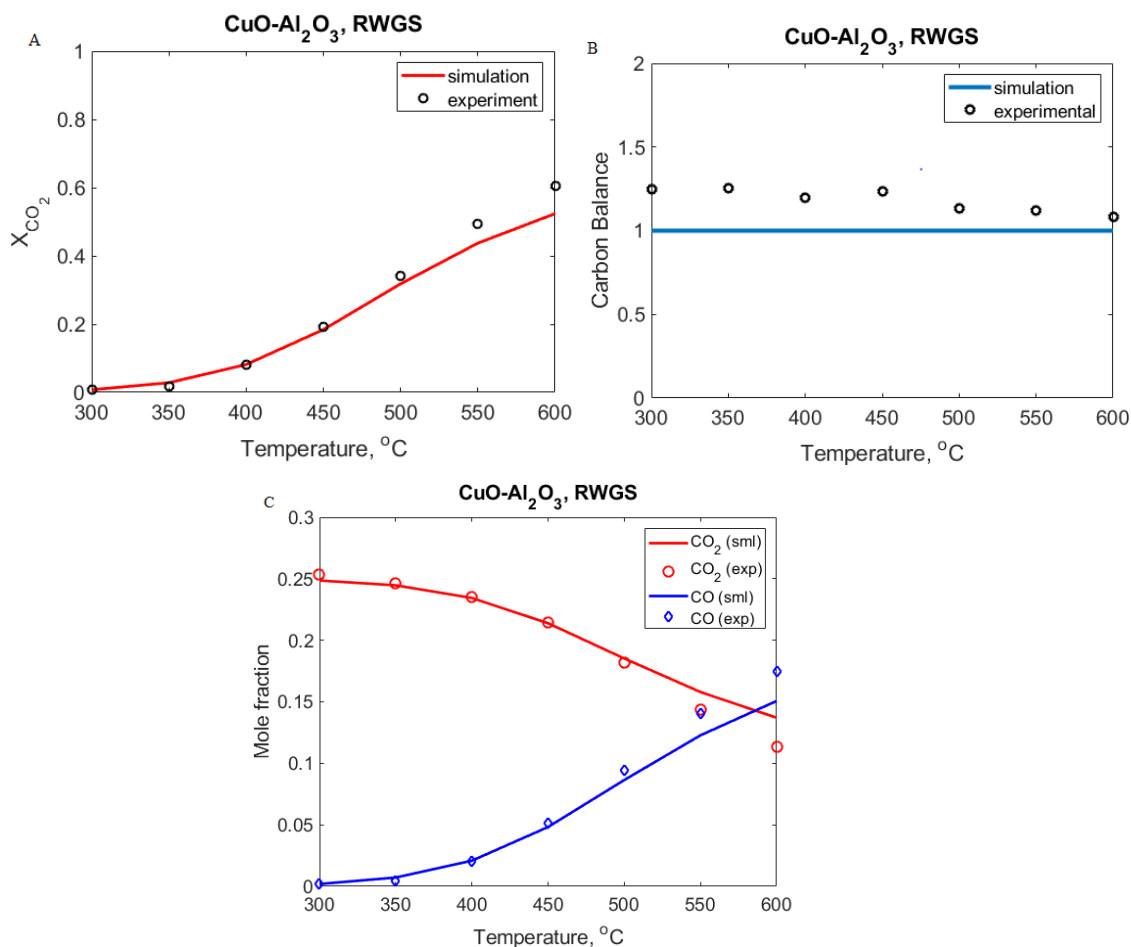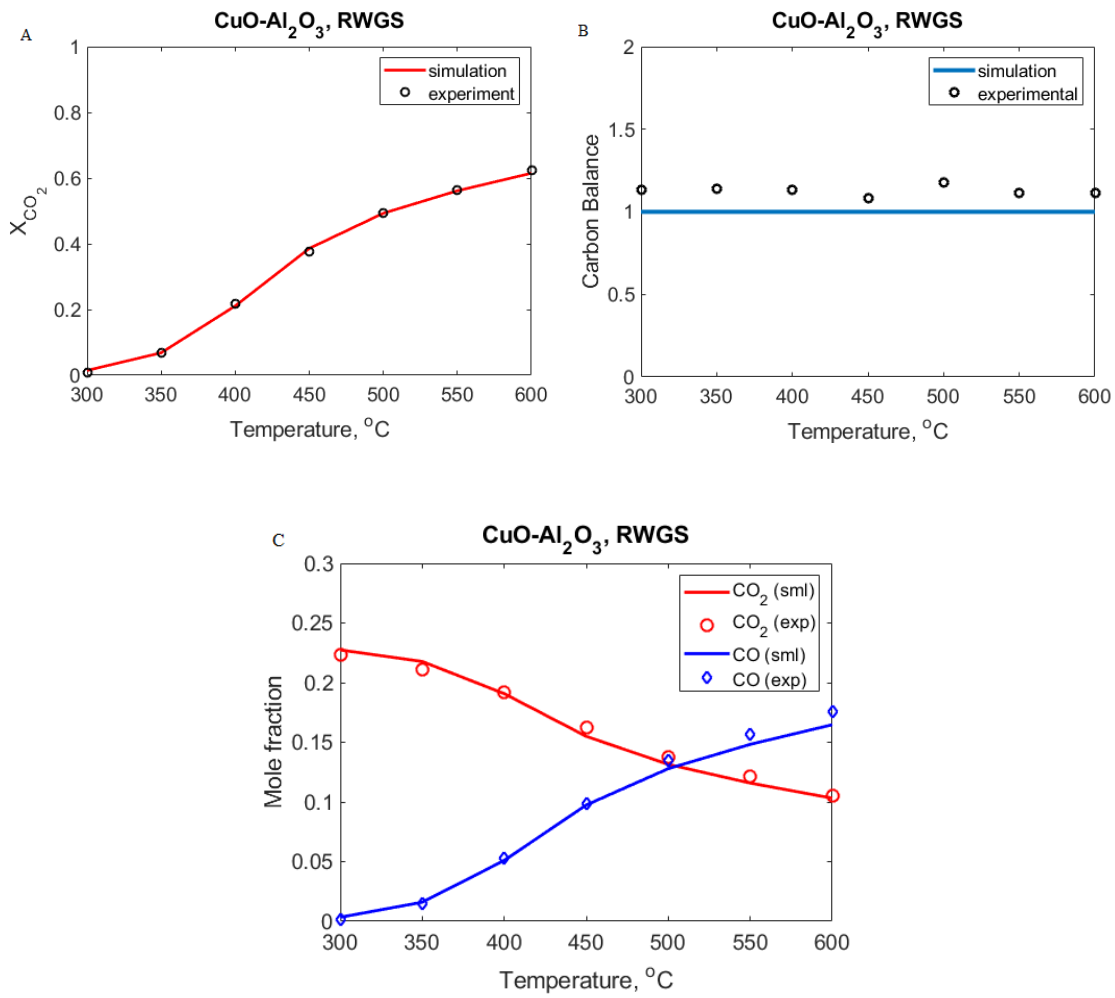
Fig. 37 A-Conversion of CO_2; B-Carbon Balance; C- Mole fraction. Experimental conditions: $H_2/CO_2 = 4$ in the feed, P = 3 bar, GHSV=10,000 mL/(gcat·h)
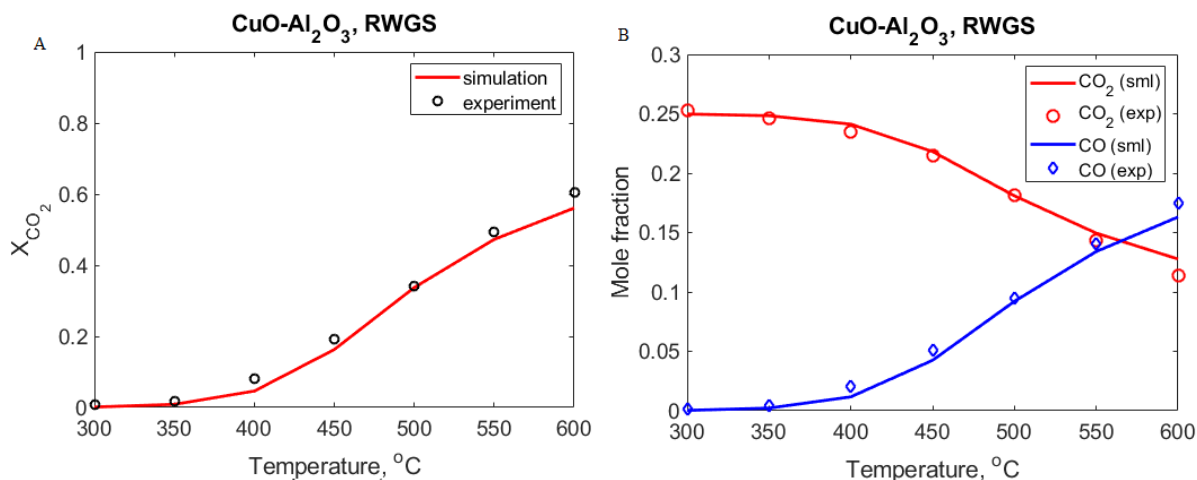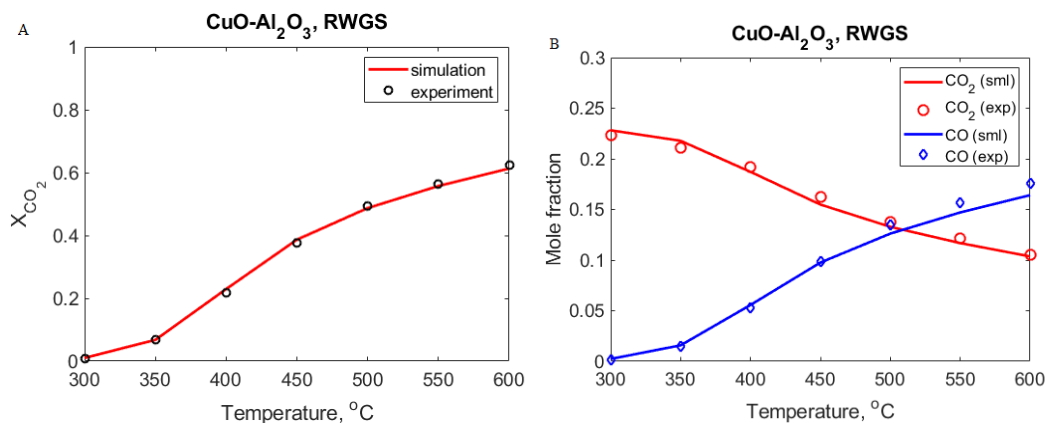
Fig. 38 A-Conversion of CO_2; B- Mole fraction profile. Experimental conditions: $H_2/CO_2 = 4$ in the feed, P = 3 bar, GHSV=10,000 mL/(gcat·h).

In both Fig. 37 and Fig.38 it can be seen that the adsorption constants do not influence significantly the conversion of CO_2 and the mole fractions. The third test can be found in Appendix C.

As a result, the parameter estimation MATLAB code works for the constant estimation. The chosen reaction rate equation closely represents the experimental data. As it can be seen in simulated vs experimental conversion to CO_2 and mole fractions plots. Moreover, the adsorption constants can be omitted in this case since the closer fitting for CO_2 conversion can be achieved without it. This reaction rate equation can be furthermore used in the reaction simulation modeling.

6.5 In-situ FTIR study

In-situ FTIR studies were conducted to investigate the adsorbed species on the copper oxide catalysts during CO_2 adsorption. Fig. 39 shows the spectra of copper oxide at different time under CO_2. The adsorbed species were identified for spent and fresh Cu/γ-Al_2O_3. At 300 °C, pronounced adsorbed peaks of CO_2, CO and carbonates were absorbed after 5 minutes of CO_2 feed

for spent and fresh Cu/γ-Al$_2$O$_3$ catalyst. The patterns obtained for the spent copper catalyst is quite different in the intensity and peaks location compare to the fresh one.
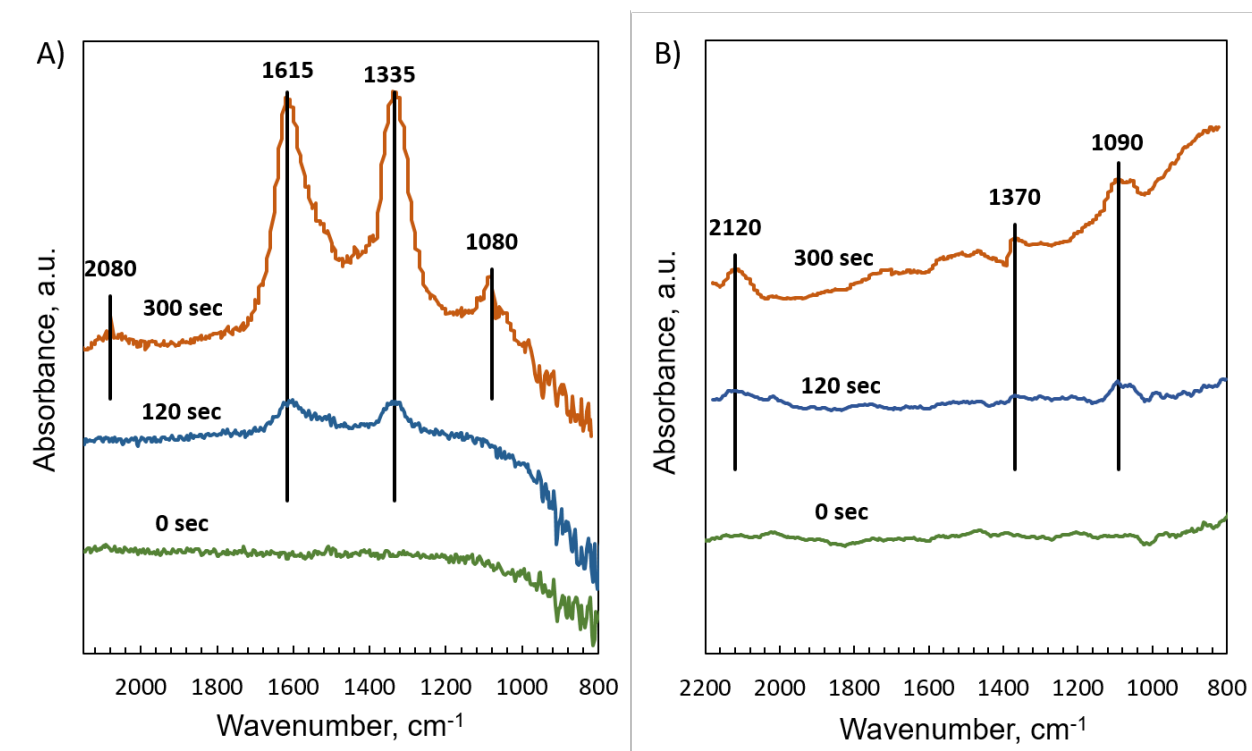
Fig. 39 Transient in-situ FTIR spectra of Cu/γ-Al$_2$O$_3$ samples: A) fresh and B) spent under 5% CO$_2$/He at 300 °C.

It can be seen that after 5 minutes of CO$_2$ feed the CO is produced on the fresh catalyst, similarly on spent catalyst we can notice the CO formation. This formation could be related to CO$_2$ dissociation [64]. In figure 42 peaks at 1370 cm^{-1}, 1335 cm^{-1} were assigned to adsorbed CO$_2$ [65]. The peaks of 2080 cm^{-1} and 2120 cm^{-1} indicated the formation of CO gas [66]. Moreover, carbonate species were identified in both spent and fresh catalyst. These peaks at 1615, 1090 cm^{-1} and 1080 cm^{-1} were absorbed on the surface [65, 67].

These findings indicate that the reaction mechanism for RWGS can possible lead to production of intermediates either carbonate or formate pathways [68][69][70]. Moreover,

interestingly that during the CO_2 feed we can obtained CO even without the H_2 in a feed at a relatively low temperature at 300 °C which indicates that the formation of CO (particularly, RWGS reaction) is favourable for the copper catalysts. More detailed study is required under the reaction test conditions to recognize the right pathway for the $Cu/\gamma\text{-}Al_2O_3$.

Chapter 7: Conclusions and future work

7.1 Conclusions

This study analyzed the effect of the reverse microemulsion (RME) synthesis on the catalytic performance of copper oxide supported on alumina nanoparticles for reverse water gas shift (RWGS). A highly active and selective catalyst was successfully synthesized by the RME method and its composition, crystallinity and morphology were investigated by a number of analytical techniques, including ICP-OES, TPR, TPD, XRD, SEM and SEM-EDS (see Chapter 3 for methodology). SEM-EDS proved that the copper was highly-dispersed on the alumina support. The size of nanoparticles was about 6.5 nm for fresh catalyst and about 22 nm for the spent one, as determined by TPD. TPR curve indicated the reducibility where the peaks were assigned either to highly-dispersed CuO or bulk CuO. Due to the peak location starting from 250 to 300 °C, the temperature for the reduction was chosen at 350 °C to ensure complete reducibility before the reaction.

The catalytic performance in the RWGS reaction was investigated in the range of temperatures and space velocities in terms of CO_2 conversion and selectivity to CO generation (CO selectivity). It was shown that the alumina-supported copper synthesized by the RME method can produce high surface area catalyst. The RME method was demonstrated as a promising approach to synthesize a high surface area catalyst with enhanced catalytic activity. The synthesized $Cu/\gamma\text{-}Al_2O_3$ catalyst was found to be highly active for the RWGS reaction (up to 60% conversion at 600 °C), achieving complete selectivity to CO for all conditions investigated. Stability test for 100 h on stream with a varying space velocity showed that the synthesized catalyst retained the superior selectivity to CO formation.

The CO_2 adsorption experiment was conducted using in-situ FTIR to investigate the mechanism of CO_2 adsorption on the catalyst surface. During the experiment with feeding a diluted CO_2, CO_2 was adsorbed on the catalyst surface and CO was produced as well, which was related to CO_2 dissociation after stabilization. The carbonate species, which are reaction intermediates, were found adsorbed on the catalyst surface as well.

The collected experimental data was analyzed via parameter estimation by fitting the experimental data to a derived kinetic model (using MATLAB). The model was developed and investigated in order to predict the performance of the catalyst under various operating conditions. The rate expression was constructed based on the Langmuir-Hinshelwood formulation as derived from the elementary steps. The resulted model was able to predict well the obtained experimental data. The reaction rate expression with the estimated parameters can be implemented to access the catalytic performance over a wide range of industrially relevant operating conditions.

7.2 Future work

Future work will require further investigation of the reaction mechanism (using in-situ FTIR) and additional experimental tests with the goal of improving the catalytic performance of the RME-synthesized $Cu/\gamma-Al_2O_3$ catalyst to achieve higher conversion at lower temperatures. The derived rate expression with estimated parameters should be further investigated experimentally to verify its validity in a wide range of operating conditions. This additional investigation will determine the catalyst performance more precisely to evaluate the potential practical application.

In order to maximize the performance of the RME-synthesized catalyst, various parameters of the synthesis procedure could be varied and optimized. For example, the effect of different copper loading and promotion with an additional metal can be investigated to optimize the

conversion, while retaining complete selectivity to CO. For practical applications, lower temperatures, higher space velocities and elevated pressures are preferred. These, industrially relevant conditions, should be tested experimentally in the lab (to the extent possible) and via simulations using the developed kinetic model (rate expression) with previously estimated parameters.

References

1. Solomon, S., et al., *Irreversible climate change due to carbon dioxide emissions*. 2009. **106**(6): p. 1704-1709.
2. Mi, Z., et al., *Carbon emissions of cities from a consumption-based perspective*. 2019. **235**: p. 509-518.
3. Hansen, J., et al., *Global temperature change*. 2006. **103**(39): p. 14288-14293.
4. Mikkelsen, M., et al., *The teraton challenge. A review of fixation and transformation of carbon dioxide*. 2010. **3**(1): p. 43-81.
5. Simakov, D.S.A., *Renewable Synthetic Fuels and Chemicals from Carbon Dioxide: Fundamentals, Catalysis, Design Considerations and Technological Challenges* ed. S.I. Publishing. 2017.
6. Sun, J., et al., *Beyond Cars: Fischer-Tropsch Synthesis for Non-Automotive Applications*. 2019. **11**(5): p. 1412-1424.
7. dos Santos, R.G. and A.C.J.I.J.o.H.E. Alencar, *Biomass-derived syngas production via gasification process and its catalytic conversion into fuels by Fischer Tropsch synthesis: A review*. 2020. **45**(36): p. 18114-18132.
8. Yang, L., et al., *CO_2 valorisation via reverse water-gas shift reaction using promoted Fe/CeO_2-Al_2O_3 catalysts: Showcasing the potential of advanced catalysts to explore new processes design*. 2020. **593**: p. 117442.
9. Sun, D., F.M. Khan, and D.S. Simakov, *Heat removal and catalyst deactivation in a Sabatier reactor for chemical fixation of CO_2: Simulation-based analysis*. Chem. Eng. J., 2017. **329**: p. 165-177.
10. *Canadian Environmental Sustainability Indicators Greenhouse gas emissions* 2021; Environment and Climate Change Canada https://www.canada.ca/content/dam/eccc/documents/pdf/cesindicators/ghg-emissions/2021/greenhouse-gas-emissions-en.pdf].
11. *Electricity facts, Natural Resources Canada*. 2021; https://www.nrcan.gc.ca/sites/nrcan/files/energy/energy_fact/energy-factbook-2020-2021-English.pdf].
12. Liang, B., et al., *Promoting role of potassium in the reverse water gas shift reaction on Pt/mullite catalyst*. Catalysis Today, 2017. **281**: p. 319-326.
13. Choi, S., et al., *Catalytic behavior of metal catalysts in high-temperature RWGS reaction: In-situ FT-IR experiments and first-principles calculations*. Scientific reports, 2017. **7**: p. 41207.
14. Kusama, H., et al., *CO_2 hydrogenation reactivity and structure of Rh/SiO_2 catalysts prepared from acetate, chloride and nitrate precursors*. Applied Catalysis A: General, 2001. **205**(1-2): p. 285-294.
15. Sengupta, S., et al., *Catalytic performance of Co and Ni doped Fe-based catalysts for the hydrogenation of CO_2 to CO via reverse water-gas shift reaction*. Journal of Environmental Chemical Engineering, 2019. **7**(1): p. 102911.
16. Pastor-Pérez, L., et al., *CO_2 valorisation via reverse water-gas shift reaction using advanced Cs doped Fe-Cu/Al_2O_3 catalysts*. Journal of CO2 Utilization, 2017. **21**: p. 423-428.

17.   Wang, X., et al., *Highly selective conversion of CO_2 to light olefins via Fischer-Tropsch synthesis over stable layered K–Fe–Ti catalysts.* Applied Catalysis A: General, 2019. **573**: p. 32-40.

18.   Sun, F.-m., et al., *Ni/Ce–Zr–O catalyst for high CO_2 conversion during reverse water gas shift reaction (RWGS).* International journal of hydrogen energy, 2015. **40**(46): p. 15985-15993.

19.   Zhang, X., et al., *Highly dispersed copper over β-Mo_2C as an efficient and stable catalyst for the reverse water gas shift (RWGS) reaction.* ACS Catalysis, 2017. **7**(1): p. 912-918.

20.   Bansode, A., et al., *Impact of K and Ba promoters on CO_2 hydrogenation over Cu/Al_2O_3 catalysts at high pressure.* Catalysis Science & Technology, 2013. **3**(3): p. 767-778.

21.   Lin, L., et al., *Conversion of CO_2 on a highly active and stable $Cu/FeO_x/CeO_2$ catalyst: tuning catalytic performance by oxide-oxide interactions.* Catalysis Science & Technology, 2019. **9**(14): p. 3735-3742.

22.   Daza, Y.A. and J.N. Kuhn, *CO_2 conversion by reverse water gas shift catalysis: comparison of catalysts, mechanisms and their consequences for CO_2 conversion to liquid fuels.* RSC advances, 2016. **6**(55): p. 49675-49691.

23.   Bahmanpour, A.M., et al., *Essential role of oxygen vacancies of Cu-Al and Co-Al spinel oxides in their catalytic activity for the reverse water gas shift reaction.* 2020. **266**: p. 118669.

24.   Jurković, D.L., et al., *Effect of Copper-based Catalyst Support on Reverse Water-Gas Shift Reaction (RWGS) Activity for CO_2 Reduction.* Chemical Engineering & Technology, 2017. **40**(5): p. 973-980.

25.   Sakurai, H., et al., *Low-temperature water–gas shift reaction over gold deposited on TiO_2.* Chemical Communications, 1997(3): p. 271-272.

26.   Moulik, S.P. and B.K. Paul, *Structure, dynamics and transport properties of microemulsions.* Advances in Colloid and Interface science, 1998. **78**(2): p. 99-195.

27.   Malik, M.A., M.Y. Wani, and M.A. Hashim, *Microemulsion method: A novel route to synthesize organic and inorganic nanomaterials: 1st Nano Update.* Arabian journal of Chemistry, 2012. **5**(4): p. 397-417.

28.   Tovstun, S.A. and V.F. Razumov, *Preparation of nanoparticles in reverse microemulsions.* Russian Chemical Reviews, 2011. **80**(10): p. 953.

29.   Li, W., et al., *Preparation of CaP/pDNA nanoparticles by reverse micro-emulsion method: Optimization of formulation variables using experimental design.* asian journal of pharmaceutical sciences, 2017. **12**(2): p. 179-186.

30.   Lee, E. and A. Manthiram, *One-step reverse microemulsion synthesis of $Pt−CeO_2/C$ catalysts with improved nanomorphology and their effect on methanol electrooxidation reaction.* The Journal of Physical Chemistry C, 2010. **114**(49): p. 21833-21839.

31.   Xiong, L., K.L. More, and T. He, *Syntheses, characterization, and catalytic oxygen electroreduction activities of carbon-supported PtW nanoparticle catalysts.* Journal of Power Sources, 2010. **195**(9): p. 2570-2578.

32.   Zarur, A.J., H.H. Hwu, and J.Y. Ying, *Reverse microemulsion-mediated synthesis and structural evolution of barium hexaaluminate nanoparticles.* Langmuir, 2000. **16**(7): p. 3042-3049.

33.   Bunaciu, A.A., E.G. UdriŞTioiu, and H.Y. Aboul-Enein, *X-ray diffraction: instrumentation and applications.* Critical reviews in analytical chemistry, 2015. **45**(4): p. 289-299.

34.   Inaba, K., et al., *High resolution X-ray diffraction analyses of (La, Sr) MnO₃/ZnO/Sapphire (0001) double heteroepitaxial films.* Advances in Materials Physics and Chemistry, 2013.

35.   Ghosh, S., et al., *Inductively coupled plasma–optical emission spectroscopy: a review.* 2013. **3**(1): p. 24-33.

36.   Dollimore, D., P. Spooner, and A.J.S.T. Turner, *The BET method of analysis of gas adsorption data and its relevance to the calculation of surface areas.* 1976. **4**(2): p. 121-160.

37.   *ALTAMIRA INSTRUMENTS, OPERATIONAL MANUAL FOR AMI-300lite with IR 120V.*

38.   Joshi, M., A. Bhattacharyya, and S.W. Ali, *Characterization techniques for nanotechnology applications in textiles.* 2008.

39.   Cvetanovic, R. and Y.J.A.P.N.Y. Amenomiya, *Advances in Catalysis and related Subjects.* 1967. **17**: p. 103.

40.   Allen, K.M., et al., *Cobalt ferrite in YSZ for use as reactive material in solar thermochemical water and carbon dioxide splitting, part I: material characterization.* 2013. **65**(12): p. 1670-1681.

41.   Richardson, H.W., *Handbook of Copper Compounds and Applications 1st Edition 1997* Boca Raton.

42.   Białas, A., et al., *Copper-aluminum oxide catalysts for total oxidation of toluene synthesized by thermal decomposition of co-precipitated precursors.* 2014. **590**: p. 191-197.

43.   Franey, J. and M.J.C.S. Davis, *Metallographic studies of the copper patina formed in the atmosphere.* 1987. **27**(7): p. 659-668.

44.   Ahouari, H., et al., *Methanol synthesis from CO₂ hydrogenation over copper based catalysts.* J. Reac. Kinet. Mech. Cat., 2013. **110**(1): p. 131-145.

45.   Natesakhawat, S., et al., *Active sites and structure–activity relationships of copper-based catalysts for carbon dioxide hydrogenation to methanol.* ACS Catal., 2012. **2**(8): p. 1667-1676.

46.   Wu, S., T. Harris, and K.J.T.C.J.o.C.E. McAuley, *The use of simplified or misspecified models: Linear case.* 2007. **85**(4): p. 386-398.

47.   Xu, J. and G.F.J.A.j. Froment, *Methane steam reforming, methanation and water-gas shift: I. Intrinsic kinetics.* 1989. **35**(1): p. 88-96.

48.   Elnashaie, S., et al., *On the non-monotonic behaviour of methane—steam reforming kinetics.* 1990. **45**(2): p. 491-501.

49.   Mark, M.F., et al., *Reaction kinetics of the CO2 reforming of methane.* 1997. **20**(6): p. 361-370.

50.   Bansode, A., et al., *Impact of K and Ba promoters on CO₂ hydrogenation over Cu/Al₂O₃ catalysts at high pressure.* Catal. Sci. Technol., 2013. **3**(3): p. 767-778.

51.   Zhuang, Y., et al., *Highly-selective CO2 conversion via reverse water gas shift reaction over the 0.5 wt% Ru-promoted Cu/ZnO/Al2O3 catalyst.* Appl. Catal. A-Gen., 2019. **575**: p. 74-86.

52.   Amirsalari, A. and S.F. Shayesteh, *Effects of pH and calcination temperature on structural and optical properties of alumina nanoparticles.* Superlattices Microst., 2015. **82**: p. 507-524.

53.   Malik, M.A., M.Y. Wani, and M.A. Hashim, *Microemulsion method: a novel route to synthesize organic and inorganic nanomaterials: 1st Nano Update.* Arab. J. Chem., 2012. **5**(4): p. 397-417.

54.   Bartholomew, C.H. and R.J. Farrauto, *Fundamentals of industrial catalytic processes.* 2011: John Wiley & Sons

55.   López-Suárez, F.E., A. Bueno-López, and M.J. Illán-Gómez, *Cu/Al_2O_3 catalysts for soot oxidation: Copper loading effect.* Appl. Catal. B: Environ., 2008. **84**(3-4): p. 651-658.

56.   Bayat, N., M. Rezaei, and F. Meshkani, *Methane dissociation to COx-free hydrogen and carbon nanofiber over $Ni-Cu/Al_2O_3$ catalysts.* J. Fuel, 2017. **195**: p. 88-96.

57.   Boukha, Z., et al., *Preparation and characterisation of CuO/Al_2O_3 films deposited onto stainless steel microgrids for CO oxidation.* Appl. Catal. B: Environ., 2014. **160**: p. 629-640.

58.   Luo, M.-F., et al., *In situ XRD, Raman, and TPR studies of CuO/Al_2O_3 catalysts for CO oxidation.* J. Mol. Catal. A-Chem., 2005. **239**(1-2): p. 243-248.

59.   Kim, J.Y., et al., *Reduction of CuO and Cu_2O with H_2: H embedding and kinetic effects in the formation of suboxides.* J. Am. Chem. Soc., 2003. **125**(35): p. 10684-10692.

60.   Chen, C.-S., W.-H. Cheng, and S.-S. Lin, *Mechanism of CO formation in reverse water–gas shift reaction over Cu/Al_2O_3 catalyst.* Catal. Lett., 2000. **68**(1): p. 45-48.

61.   Hengne, A.M. and C.V. Rode, *$Cu–ZrO_2$ nanocomposite catalyst for selective hydrogenation of levulinic acid and its ester to γ-valerolactone.* J. Green Chem., 2012. **14**(4): p. 1064-1072.

62.   Chen, Y., et al., *High catalytic performance of the Al-promoted Ni/Palygorskite catalysts for dry reforming of methane.* Appl. Clay Sci., 2020. **188**: p. 105498.

63.   Pastor-Pérez, L., et al., *CO_2 valorisation via reverse water-gas shift reaction using advanced Cs doped $Fe-Cu/Al_2O_3$ catalysts.* J. CO_2 Util., 2017. **21**: p. 423-428.

64.   Chen, C.-S., W.-H. Cheng, and S.-S.J.C.l. Lin, *Mechanism of CO formation in reverse water–gas shift reaction over Cu/Al 2 O 3 catalyst.* 2000. **68**(1): p. 45-48.

65.   Vayssilov, G.N., et al., *Reassignment of the vibrational spectra of carbonates, formates, and related surface species on ceria: a combined density functional and infrared spectroscopy investigation.* 2011. **115**(47): p. 23435-23454.

66.   Fujita, S.-I., M. Usui, and N.J.J.o.C. Takezawa, *Mechanism of the reverse water gas shift reaction over Cu/ZnO catalyst.* 1992. **134**(1): p. 220-225.

67.   CHEN, K.H., et al., *Calcification of senile cataractous lens determined by Fourier transform infrared (FTIR) and Raman microspectroscopies.* 2005. **219**(1): p. 36-41.

68.   Choi, S., et al., *Catalytic behavior of metal catalysts in high-temperature RWGS reaction: In-situ FT-IR experiments and first-principles calculations.* 2017. **7**(1): p. 1-10.

69.   Arunajatesan, V., et al., *In situ FTIR investigations of reverse water gas shift reaction activity at supercritical conditions.* 2007. **62**(18-20): p. 5062-5069.

70.   Ortelli, E.E., J.M. Weigel, and A.J.C.l. Wokaun, *Methanol synthesis pathway over Cu/ZrO 2 catalysts: a time-resolved DRIFT 13 C-labelling experiment.* 1998. **54**(1): p. 41-48.

Appendix

A. Dimensionless model

The dimensionless form of mass balance time evolution of all species of the RWGS reaction,

Eqs. A1-4:

$$\frac{dN_i}{dt} = F_{if} - F_i + \alpha_i R_j W \tag{A1}$$

$$\frac{1}{W}\frac{dN_i}{dt} = \frac{F_{if} - F_i}{W} + \alpha_i R_j \tag{A2}$$

$$\frac{\varepsilon V_r}{(1-\varepsilon)\rho_{cat}V_r}\frac{dc_i}{dt} = \frac{Q_f(c_{if} - c_i)}{(1-\varepsilon)\rho_{cat}V_r} + \alpha_i R_j \tag{A3}$$

$$\varepsilon\frac{dc_i}{dt} = -\frac{Q_f(c_i - c_{if})}{V_r} + (1-\varepsilon)\rho_{cat}\alpha_i R_j \tag{A4}$$

Dimensionless variables of temperature, mole fraction and reaction time, Eqs. A5-7:

$$y_i = \frac{C_i}{C_t} = \frac{C_i}{\rho_g} \tag{A5}$$

$$\tau = \frac{t}{\varepsilon\left(V_r / Q_f\right)} \tag{A6}$$

$$\theta^{RWGS} = \frac{T^{RWGS}}{T} \tag{A7}$$

Dimensionless functions- an overall balance written on the catalytically active sites gives the

final rate equation accounting for the reaction rate and adsorption constants, Eqs. A8-11.

$$f_{RWGS} = exp\left(-\frac{\gamma_{RWGS}}{\theta^{RWGS}}\right)\left(y_{CO_2} - \frac{y_{CO}y_{H_2O}}{K_{RWGS}y_{H_2}}\right)\frac{1}{DEN^2}$$ (A8)

$$DEN = 1 + \hat{K}_{CO}y_{CO} + \frac{\hat{K}_{H_2O}y_{H_2O}}{y_{H_2}} \quad \hat{K}_{CO} = P_t \cdot K_{CO} \quad \hat{K}_{H_2O} = K_{H_2O}$$ (A9)

$$K_i = B_i \exp\left(-\frac{\Delta H_i}{R_g T^{RWGS}}\right) = B_i \exp\left(-\frac{\Delta H_{iad}}{\theta^{RWGS}}\right)$$ (A10)

$$K_{RWGS} = B_{eq} exp\left(-\frac{\Delta H_{eq}}{R_g T^{RWGS}}\right) = B_{eq} \exp\left(-\frac{\Delta H_{eqad}}{\theta^{RWGS}}\right)$$ (A11)

Dimensionless parameters of reverse water gas shift reaction variables such as enthalpy change of reaction and adsorption, Damkohler number (Da), the total flow rate, Eqs. A12-16:

$$\gamma_{RWGS} = \frac{E_{a,RWGS}}{R_g T}$$ (A12)

$$\Delta H_{iad} = \frac{\Delta H_i}{R_g T}$$ (A13)

$$\Delta H_{eqad} = \frac{\Delta H_{eq}}{R_g T}$$ (A14)

$$Da_{RWGS} = \frac{W_c \cdot A_{RWGS} \cdot P_t}{F_{tf}}$$ (A15)

$$F_{tf} = Q \cdot c_{tf}$$

(A16)

The final equation was obtained in dimensionless form, Eq.17:

$$\frac{dy_i}{d\tau} = -(y_i - y_{if}) + Da_{RWGS} \cdot \alpha_i f_{RWGS}$$

(A17)

B. Parameter estimation code

```
function
dydt = CSTResti(t,y,ufCO2,ufH2,ufCO,ufH2O,ufCH4,B,deltaHeq,T,P,R,Ctf,Q,W)
global Ea ARWGS BCO deltaHCO BH2O deltaHH2O BCO2 deltaHCO2

Ct = P/(R*T);
gamma = Ctf/Ct; %%% !!! need to be noticed

uCO2 = (y(1));
uH2 = (y(2));
uCO = (y(3));
uH2O = (y(4));
uCH4 = (y(5));

%-------Kinetics and Thermodynamic Parameters------%
%-------Reaction Constant-------%
% k = ARWGS*exp((-Ea/R)*(1/T));
%-------Equilibrium Constant-------%
Keq = B*exp(-deltaHeq/(R*T));
Keqhat = Keq; % dimensionless
%-------Adsorption Constant------%
KCO = BCO*exp((-deltaHCO/R)*(1/T));
KH2O = BH2O*exp(-(deltaHH2O/R)*(1/T));
KCO2=BCO2*exp(-(deltaHCO2/R)*(1/T));

KCOhat = KCO*P/100; %dimensionless Pressure Unit [kpa to bar]
KH2Ohat = KH2O;
KCO2hat=KCO2;
%dimensionless

DEN = 1+KCOhat*gamma*uCO+KCO2hat*gamma*uCO2+KH2Ohat*uH2O/uH2;

%reaction rate
f2 = real(gamma*exp((-Ea/R)*(1/T))*(uCO2-uCO*uH2O/(uH2*Keqhat))/(DEN^2));%%%
Keqhat?Denominator

% Ftf = Q*44.643*3600;
% Ftf = Ftf/3600;
Ftf = Q*Ctf;

Da = ARWGS*W*(P/100)/(Ftf); % only used when there is no methanation

dydt = zeros(5,1);

dydt(1) = ufCO2 -y(1)+ real(Da*(-f2));
dydt(2) = ufH2 -y(2) + real(Da*(-f2));
```

```matlab
dydt(3) = ufCO -y(3)+ real(Da*(+f2));
dydt(4) = ufH2O -y(4) + real(Da*(+f2));
dydt(5) = ufCH4 -y(5) + real(Da*(0));

end

function resids = SSE_CSTR_ALL_mod_newresults(parms)

global Ea ARWGS BCO deltaHCO BH2O deltaHH2O BCO2 deltaHCO2

deltaHeq = 36.5816; % known ref[3] pg[2]
B = 56.5995; %known ref[3] pg[2]

Ea=parms(1);
ARWGS=parms(2);
BCO=parms(3);
deltaHCO=parms(4);
BH2O = parms(5);
deltaHH2O = parms(6);
BCO2=parms(7);
deltaHCO2=parms(8);

disp(Ea)
disp(ARWGS)
disp(BCO)
disp(deltaHCO)
disp(BH2O)
disp(deltaHH2O)
disp(BCO2)
disp(deltaHCO2)

%Experimental Results
%Order: GHSV Tests (6 points each), Temperature Tests (13 points each)
flow = [(50/(60*1000*1000)) (100/(60*1000*1000)) (300/(60*1000*1000))
(500/(60*1000*1000)) (750/(60*1000*1000)) (1000/(60*1000*1000))];
CO2exp = [14.34096684
14.58698146
17.41404591
18.28940487
19.12040098
19.47617358
]';%18+8*3
COexp = [11.68805063
10.80462674
6.127729116
3.769296199
2.361130416
1.61860244
]';

%save('CO2exp.mat','CO2exp');
%save('COexp.mat','COexp');

%Temperature & Pressure
```

90

```matlab
P = 45/0.145038; %kPa
R = 8.314e-3;

%dimensionless concentrations
ufCO2 = 0.2; %CO2
ufH2 = 0.8; %H2
ufCO = 0;
ufH2O = 0;
ufCH4 = 0;

%initial conditions
tspan = [0 10];

row = length(CO2exp);
flowcount = 1;
yCO2PRED = zeros(row,1);
yCOPRED = zeros(row,1);


for k=1:1:row

    if k <= 6
     ufCO2 = 0.2; %CO2
     ufH2 = 1-0.2; %H2
     y0 = [ufCO2 ufH2 ufCO ufH2O ufCH4];
     T = 450 + 273.15; % K
     W=0.000311;
     Q = flow(flowcount);
     flowcount = flowcount+1;
     if flowcount > 6
         flowcount = 1;
     end
end

Ctf = P/(R*T);
[t,y] = ode15s(@(t,y)
CSTResti(t,y,ufCO2,ufH2,ufCO,ufH2O,ufCH4,B,deltaHeq,T,P,R,Ctf,Q,W),tspan,y0);

CO2pre = y(:,1);%(:,1) the first column of the matrix
H2pre = y(:,2);
COpre = y(:,3);
H2Opre = y(:,4);
CH4pre = y(:,5);

utpre = CO2pre+H2pre+COpre+H2Opre+CH4pre;
utdpre = utpre-H2Opre;

yCO2pre = CO2pre/utpre;
yH2pre = H2pre/utpre;
yCOpre = COpre/utpre;
yH2Opre = H2Opre/utpre;
yCH4pre = CH4pre/utpre;
```

```matlab
ydCO2pre = CO2pre/utdpre; % dry
ydH2pre = H2pre/utdpre; % dry
ydCOpre = COpre/utdpre; % dry
ydCH4pre = CH4pre/utdpre; % dry


m = length(ydCO2pre);

yCO2PRED(k,1) = ydCO2pre(m)*100;
yCOPRED(k,1) = ydCOpre(m)*100;




end




varCO2 = 1; % pooled variance
varCO = 1; % pooled variance




%resids = [(CO2exp-yCO2PRED)'*(CO2exp-yCO2PRED)/varCO2 (COexp-
yCOPRED)'*(COexp-yCOPRED)/varCO]
resids = [(CO2exp-yCO2PRED)/sqrt(varCO2); (COexp-yCOPRED)/sqrt(varCO)]; %
%reguar residuals

% save('CO2Pred.mat','yCO2PRED');
% save('COPred.mat','yCOPRED');
% save('CO2Exp.mat','CO2exp');
% save('COExp.mat','COexp');

SSE_scaled = sum(resids.^2);
% save('SSE.mat','SSE_scaled','resids');

end


function SSE_lsqnonlin_mod_WTR

close all
clear
%Initial guesses for parameters and bounds may need to be changed
initial guesses for activation energy and pre-exponential factor & adsorb
constants
parms0 = [117.5 4.9E+07 8.2E-05 -70.6 1.7E+05 88.6 97.9 35];
lb = [parms0(1)-parms0(1)*0.5 parms0(2)*0.01 parms0(3)*0.01
parms0(4)+parms0(4)*0.5 parms0(5)*0.01 parms0(6)-parms0(6)*0.5 parms0(7)*0.01
parms0(8)-parms0(8)*0.5]; %lower bounds for the solver
ub = [parms0(1)+parms0(1)*0.5 parms0(2)*100 parms0(3)*100 parms0(4)-
parms0(4)*0.5 parms0(5)*100 parms0(6)+parms0(6)*0.5 parms0(7)*100
parms0(8)+parms0(8)*0.5]; %upper bounds for the solver
```

```
options = optimset('Display','iter','MaxIter',1000,'TolX',1e-9,'TolFun',1e-
9); %Tolerances for the solvers
[parmshat,resnorm,residual,exitflag,output]=
lsqnonlin('SSE_CSTR_ALL_mod_newresults',parms0,lb,ub,options); %calling the
minimization function

parmshat=parmshat'
output;
SSE = resnorm
residual

%CSTRplot(parmshat)
end

function SSE_lsqnonlin

close all
clear

parmshat = [   1.164682814669014e+02
      4.995655646829545e+07
      4.382698983126468e-05
     -7.154706275834795e+01
      1.844298711819113e+05
      8.462040993703756e+01
      9.756407612628242e+01
      3.499241694178877e+01]

CSTRplot(parmshat)
end

function CSTRplot(parms)
close all
%Constants
R=8.314e-3; %gas constant
%ro_s=1.274e+3; %catalyst density
ro_s = 3.956e+3;

%----reactor geometry-------
%L=1;dr=0.2; epsi=0.5; V=L*pi*(dr/2);
epsi = 0.5; V = 0.0003 /((1-epsi)*ro_s); %volume calculated so that Wc = 218
mg
%Q = 200/(60*1000*1000); %200ml/min

%----Ea & equilibrium enthopy---
deltaHeq2=36.5816;
B2=56.5995;

Ea = parms(1);
ARWGS = parms(2);
BCO=parms(3);
deltaHCO=parms(4);
BH2O = parms(5);
deltaHH2O = parms(6);
BCO2=parms(7);
```

93

```matlab
deltaHCO2 = parms(8);


%Temperature & Pressure

P = 45/0.145038; %psi to kpa

%dimensionless concentrations
ufCO2 = 0.2; %CO2
ufH2 = 0.8; %H2
ufCO = 0;
ufH2O = 0;

%initial conditions
y0 = [ufCO2 ufH2 ufCO ufH2O];

%dimensionless time
tspan = [0 10]; %number of T test points
p=6; %number of GHSV test points
vo = zeros(p,1);


T = 450 + 273.15; %K
flow = [(50/(60*1000*1000)) (100/(60*1000*1000)) (300/(60*1000*1000))
(500/(60*1000*1000)) (750/(60*1000*1000)) (1000/(60*1000*1000)) ];
flowcount=1;
%dimensionless concentrations
ufCO2 = 0.2; %CO2
ufH2 = 0.8; %H2
ufCO = 0;
ufH2O = 0;

%initial conditions
y0 = [ufCO2 ufH2 ufCO ufH2O];

for j=1:p
Q = flow(flowcount);
flowcount = flowcount+1;
if flowcount > 6
    flowcount = 1;
end
vo(j,1) = Q*(60*1000*1000*60)/(0.000450*1000);

%Inlet molar density
Ctf = P/(R*T);
Ct = P/(R*T); % placeholder for later

[t,y] = ode45(@(t,y)
CSTRRWGS(t,y,ufCO2,ufH2,ufCO,ufH2O,Ea,ARWGS,B2,deltaHeq2,T,P,R,ro_s,Ctf,epsi,
V,Q,BCO,deltaHCO,BH2O,deltaHH2O,BCO2,deltaHCO2),tspan,y0);

%plotting dimensionless concentrations
%figure(1);
%plot(t,y,'LineWidth',3);
```

94

```matlab
%title('CSTR Dimensionless Concentration Plot');
%legend('CO2','H2','CO','H2O','CH4');
%xlabel('Dimensionless Time');
%ylabel('Dimensionless Concentration');

%creating empty vectors
uCO2 = zeros(size(y,1),1);
uH2 = zeros(size(y,1),1);
uCO = zeros(size(y,1),1);
uH2O = zeros(size(y,1),1);
ut= zeros(size(y,1),1);
utd = zeros(size(y,1),1);

yCO2 = zeros(size(y,1),1);
yH2 = zeros(size(y,1),1);
yCO = zeros(size(y,1),1);
yH2O = zeros(size(y,1),1);

ydCO2 = zeros(size(y,1),1);
ydH2 = zeros(size(y,1),1);
ydCO = zeros(size(y,1),1);

f1= zeros(size(y,1),1);
alpha = zeros(size(y,1),1);
CB = zeros(size(y,1),1);


XCO2 = zeros(size(y,1),1);

%populating individual dimensionless concentrations vectors
for i=1:size(y,1)
    uCO2(i) = y(i,1);
    uH2(i) = y(i,2);
    uCO(i) =y(i,3);
    uH2O(i) = y(i,4);
    ut(i) = uCO2(i)+uH2(i)+uCO(i)+uH2O(i);
    utd(i) = ut(i)-uH2O(i);


    yCO2(i) = uCO2(i)/ut(i);
    yH2(i) = uH2(i)/ut(i);
    yCO(i) =uCO(i)/ut(i);
    yH2O(i) = uH2O(i)/ut(i);

    ydCO2(i) = uCO2(i)/utd(i);
    ydH2(i) = uH2(i)/utd(i);
    ydCO(i) = uCO(i)/utd(i);

    f1(i) = ydCO(i)/(ydCO(i)+ydCO2(i));

    alpha(i) = ydH2(1)/ydCO2(1);

    CB(i) = (ydCO2(i)+ydCO(i))*(1+alpha(i)-f1(i));
```

95

```matlab
        XCO2(i) = (yCO(i))/(yCO2(i)+yCO(i)); % no methanation

end


QxCO2end(j,1) = XCO2(end);
QydCO2end(j,1) = ydCO2(end);
QydCOend(j,1) = ydCO(end);
QCBend(j,1) = CB(end);
Qutot(j,1) = alpha(end);

end

%Experimental Temperature CO2 measurements !!!mole fraction!!!



QCO2Batch = [14.34096684
14.58698146
17.41404591
18.28940487
19.12040098
19.47617358
]/100;



QCOBatch = [11.68805063
10.80462674
6.127729116
3.769296199
2.361130416
1.61860244
]/100;




% %Experimental Temperature Results

%Experimental Flowrate Results
Qexp = [50 100 300 500 750 1000]*60./0.45; %flowrates mL/min, output in mL/ g
h
QBatch = [0.4485 0.4250 0.2599 0.1706 0.1099 0.0767]; %results from IR

QBatchCB = [1.07 1.03 0.96 0.98 0.95 1];



%plotting exp temperature vs simulation g


%plotting exp flowrate vs simulation g
figure(2)
```

```matlab
plot(vo,QCBend,'LineWidth',3);
hold on; plot(Qexp,QBatchCB,'o','LineWidth',2)
title('CuO-Al_2O_3, RWGS');
ylim([0 2]);
legend('simulation','experimental');
xlabel('GHSV, mL/g h');
ylabel('Carbon Balance');
set(gcf,'color','w')
set(gca,'FontSize',14);




figure (5)
plot(vo,QxCO2end,'r-','LineWidth',2);
hold on; plot(Qexp,QBatch,'ko','LineWidth',1.5);
ylim([0 1]);
title('CuO-Al_2O_3, RWGS');
legend('simulation','experiment')
xlabel('GHSV, mL/(g h)');
ylabel
set(gcf,'color','w')
set(gca,'FontSize',14);
%

figure (7)
plot(vo,QydCO2end,'r-','LineWidth',2);
hold on; plot(Qexp,QCO2Batch,'ro','LineWidth',1.5,'MarkerSize',8);
plot(vo,QydCOend,'b-','LineWidth',2);
hold on; plot(Qexp,QCOBatch,'bd','LineWidth',1.5,'MarkerSize',8);
ylim([0 0.3]);
% xlim([0 2]);
title('CuO-Al_2O_3, RWGS');
legend({'CO_2 (sml)','CO_2 (exp)','CO (sml)','CO (exp)'},'FontSize',12)
xlabel('GHSV, mL/(g h)', 'FontSize',16);
ylabel('Mole fraction', 'FontSize',16);
set(gcf,'color','w')
set(gca,'FontSize',14);

end


function dydt =
CSTRRWGS(t,y,ufCO2,ufH2,ufCO,ufH2O,Ea,ARWGS,B2,deltaHeq2,T,P,R,ro_s,Ctf,epsi,
V,Q,BCO,deltaHCO,BH2O,deltaHH2O,BCO2,deltaHCO2)
%-----------inlet & outlet molar density-----------
Ct = P/(R*T); %mol /m3
gamma = Ctf/Ct; % dimensionless
%dimensionless concentrations
uCO2 = (y(1));
uH2 = (y(2));
uCO = (y(3));
uH2O = (y(4));
%---------Kinetics-------------
%-------Reaction Constant------%
```

```matlab
%k2 = ARWGS*exp((-Ea2/R)*(1/T)); %mol /kg s bar
Keq2 = B2*exp(-deltaHeq2/(R*T)); %dimensionless
Keq2hat = Keq2; %dimensionless


KCO2=BCO2*exp(-(deltaHCO2/R)*(1/T));
KCO = BCO*exp((-deltaHCO/R)*(1/T));
KH2O = BH2O*exp(-(deltaHH2O/R)*(1/T));
KCOhat = KCO*P/100; %dimensionless
KH2Ohat = KH2O; %dimensionless
KCO2hat=KCO2;
DEN =1+KCOhat*gamma*uCO+KCO2hat*gamma*uCO2+KH2Ohat*uH2O/uH2;


%reaction rates
f2 = real(gamma*exp((-Ea/R)*(1/T))*(uCO2-uCO*uH2O/(uH2*Keq2hat))/(DEN^2));
%dimensionless


%dimensionless terms

W = 0.00031; %kg,
Ftf = Q*44.643*3600; %mol/hr
Ftf = Ftf/3600; %mol/s
Da = ARWGS*W*(P/100)/(Ftf); % dimensionless

dydt = zeros(4,1);

dydt(1) = ufCO2 -y(1)+ real(Da*(-f2));
dydt(2) = ufH2 -y(2) + real(Da*(-f2));
dydt(3) = ufCO -y(3)+ real(Da*(f2));
dydt(4) = ufH2O -y(4) + real(Da*(f2));
end
```

C. Parameter estimation results

Thirdly, the GHSV test at 10,000 mL/(g h) and 60,000 ml/(g h), and GHSV test (10,000 mL/(g h); 20,000 mL/(g h); 60,000 mL/(g h); 100,000 mL/(g h); 150,000 mL/(g h); 200,000 mL/(g h) was performed under the constant temperature 450°C and 3 bar, respectively. The experimental H_2/CO_2 ratio is 4:1 as well as the parameter estimation one. The initial guesses for activation energy and pre-exponential factor of the experimental data for 10,000 were used for this GHSV test. The parameter estimation results are shown in Table C1.

Table C1 Parameter estimation results for GHSV test.

Set/Parameter	Ea, kJ/mol	A_{RWGS}, mol/(bar s kg)	B_{CO}, bar^{-1}	ΔH_{CO}, kJ/mol	B_{H2O}, bar^{-1}	ΔH_{H2O}, kJ/mol	B_{CO2}, bar^{-1}	ΔH_{CO2}, kJ/mol
Initial guess	117.5	4.9E+07	8.2E-05	-70.6	1.7E+05	88.6	97.9	35
1	116.4	4.9E+07	4.3E-05	-71.5	1.8E+05	84.6	97.5	34.9
2	120.4	4.7E+07	-	-	-	-	-	-

The results also show the same tendency, the dependence on the adsorption coefficients. Obtained results are plotted for the further examination. For the first set, the mole fraction, conversion and carbon balance plots are shown in Fig.C1.
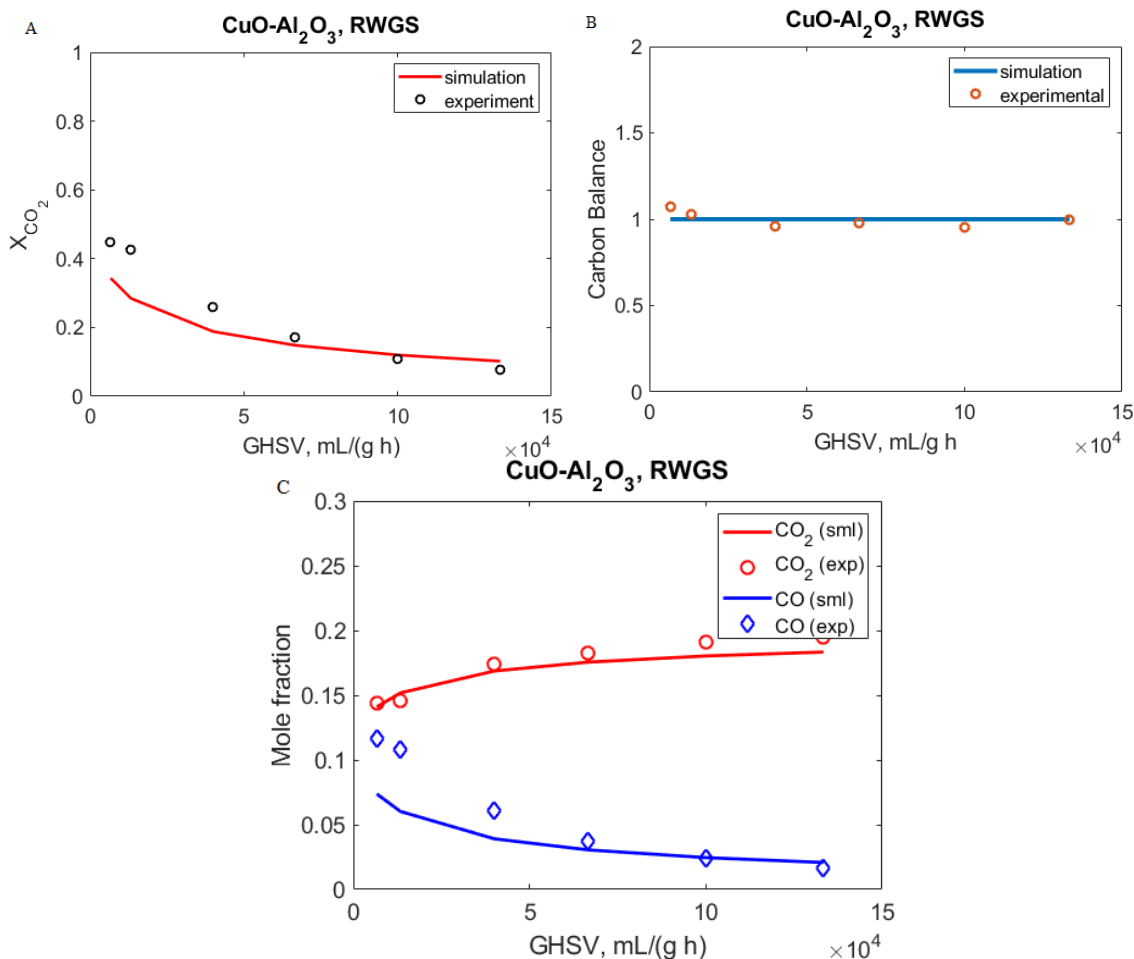
Fig. C1 A-Conversion of CO_2; B-Carbon Balance; C- Mole fraction profile. A-Conversion of CO_2; B-Carbon Balance; C- Mole fraction profile. Experimental conditions: $H_2/CO_2 = 4$ in the feed, P = 3 bar, T=450 °C.

The carbon balance is relatively stable and close to 100%. The conversion to CO_2 is quite lower compare to parameter estimation results at lower GHSV. The same can be seen for the mole fraction of CO the simulation data seems to be lower compare to experimental data.

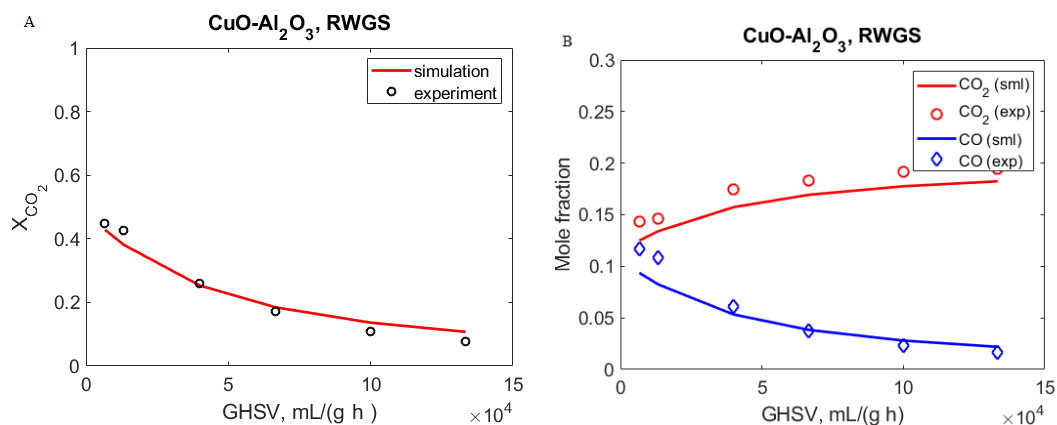The second set, the mole fraction and conversion of CO_2 are plotted in Fig.C2.

Fig. C2 A-Conversion of CO_2; B- Mole fraction profile. Experimental conditions: $H_2/CO_2 = 4$ in the feed, P = 3 bar, T=450°C.

The conversion field at DEN=1 fits better compare to the previously obtained plot with calculated DEN (Eq.47). As for the mole fraction simulation profile, the CO_2 mole fraction the line is a little bit down compare to the previous plot, while CO mole fraction matches closely experimental data. Therefore, the plots at DEN=1 look better than for the first set of data.